ՀՀ ԿՐԹՈՒԹՅԱՆ ԵՎ ԳԻՏՈՒԹՅԱՆ ՆԱԽԱՐԱՐՈՒԹՅՈՒՆ

Վ.Հ. ՀԱՄԲԱՐՁՈՒՄՅԱՆԻ ԱՆՎԱՆ ԲՅՈՒՐԱԿԱՆԻ ԱՍՏՂԱԴԻՏԱՐԱՆ

Սարգիս Արմենի Գասպարյան

Բլազարների ուսումնասիրությունը բարձր էներգիաների գամմա-փիրույթում

ԱՏԵՆԱԽՈՍՈՒԹՅՈՒՆ

Ա.03.02 - «Աստղագիտություն» մասնագիտությամբ

ֆիզիկամաթեմատիկական գիտությունների

թեկնածուի գիտական աստիճանի համար

Գիտական ղեկավար՝

ֆ.մ.գ.թ., Հայկ Հարությունյան

Երևան-2019

NATIONAL ACADEMY OF SCIENCES OF THE REPUBLIC OF ARMENIA

BYURAKAN ASTROPHYSICAL OBSERVATORY

Sargis Armen Gasparyan

Study of blazars in the high energy gamma-ray band

DOCTORAL THESIS

A thesis submitted in fulfillment of the requirements

for the degree of Doctor of Philosophy

in

specialization 03.02 – "Astronomy"

Supervisor:

Dr. Hayk Harutyunian

Yerevan–2019

Content

INTRODUCTION

Understanding the formation, structure and evolution of our Universe is one of the greatest mysteries that humans are trying to understand. Different branches of astronomy (astrophysics) are devoted to study cosmic objects by applying known physical principles and rules. Initially being limited by the possibility to explore only nearby cosmic objects, now the technical developments provide a chance to observe and investigate also very distant extragalactic objects. These studies are crucial not only for expanding our knowledge but also can significantly help to answer some fundamental questions such as how and when our planet and solar system formed, etc. For example, measurements by different experiments allowed relatively precise estimation of the age of the Universe (13.799 ± 0.021 billion years) and to understand its different epochs (formation of galaxies, stars, etc.) as well as investigate the processes taking place in different objects, etc. The latter one is especially important since by studying different astrophysical objects currently known physical processes can be tested under the extreme conditions (high magnetic field, dense medium, etc.) which are hardly possible to form in the experiments. These makes astrophysics one of the most interesting and progressively developing fields of physics.

Now the observations provide huge amount of high quality data allowing deep and high resolution view of astrophysical objects and their components. For example, in the observations at low frequencies with an exceptional angular resolution various components and their spatial structures can be investigated. Combining it with the enormous progress in the theoretical physics, the processes taking place in cosmic objects can be investigated through modeling and/or numerical simulations. Taking into account, the amount of available data which can be modeled, the number of sources which can be studied, the precise modeling technique and our current understanding of the processes, perhaps now we are in the golden ages for observational and theoretical astrophysics.

Currently, the astrophysical sources can be studied by detecting photons with energies from radio to Very High Energy (VHE;$> 100\, GeV$) γ-ray bands (multiwavelength astrophysics) as well as detecting neutrinos (multimessenger astrophysics). While

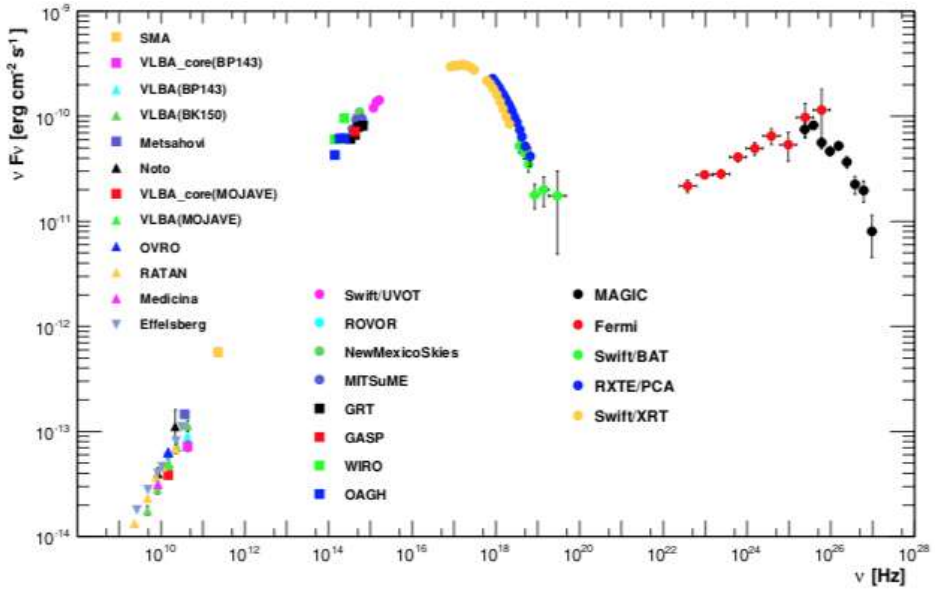

Figure 1.1. The broadband spectral energy distribution of Markarian 421 (1).

multimessenger observations of the sources started recently when the first-time gravitational waves and neutrinos were observed from known sources (2) (3), multi wavelength astrophysics is one of the fastest developing and most progressive fields of astrophysics considering the large number of currently or recently operating telescopes (Very Large Telescope, Hubble Space Telescope, Spitzer Space Telescope, Herschel Space Observatory, Planck Observatory, Swift Gamma Ray Burst Explorer, Nuclear Spectroscopic Telescope Array (NuSTAR), XMM-Newton, Chandra, INTEGRAL, Fermi Large Area Telescope (*Fermi* LAT), HESS, MAGIC, VERITAS, etc.). An example of the multiwavelength spectral energy distribution (SED) of Markarian 421 obtained from simultaneous observations with more than 13 different instruments is shown in fig. 1.1. This clearly demonstrates the power of multiwavelength observations: the nonthermal processes can be investigated with a high precision in a large frequency range.

Up to now various source classes are already confirmed to have strong nonthermal emission. For example, in the HE γ-ray band, there are around 5098 identified sources which are included in the *Fermi* LAT 8-years point source catalogue while in VHE γ-ray band around 223 sources have been identified so far. However, the most impressive is not the number of detected sources but the source classes identified as strong emitters up to TeV energies. These include Galactic sources such as pulsars, supernova remnants, pulsar wind nebulae and binary systems, and extragalactic sources such as Gamma-Ray Bursts

(GRBs) and Active Galactic nuclei (AGNs)/quasars. The emission processes taking place in Galactic sources are relatively well examined and are always among the most discussed topics in astrophysics. However, the recent major progress in the telescope technique makes it possible to investigate the physical processes in extragalactic objects as well. GRBs are short-lived bursts of γ-ray photons which last from a few milliseconds to several minutes and are considered to be the most energetic transient events in the Universe (4). The huge energetics of GRBs (e.g., $10^{51}\ erg$ in the γ-ray band (5)) allowed to detect them up to the redshift of $z = 8.0 - 9.0$ (e.g., GRB 090423 at $z = 8.2$ (6)). As distinct from GRBs which last only a few seconds, AGNs can constantly emit for a very long period ($> 10^7\ yr$), making them one of the most powerful long-lived objects in the Universe (7). AGNs are the galaxies with a very luminous nucleus: the central region is more luminous than the remaining galaxy. There are various theories currently applied to explain the huge energy output from AGNs. It is well established that the huge amount of energy is realized from very compact region so it cannot be explained by the most powerful energy release (nuclear fusion) involved in the evolutionary stage of normal stars. Indeed, the efficiency of nuclear fusion is around 0.8 % which implies that the object should have $\sim 10^9$ solar mass ($M_\odot$) to produce the energy typically released in the AGNs. However, in the sources with such a mass the gravitational effects play a crucial role and the energy will be released through converting the potential energy of the matter falling onto a super massive black hole (8). The efficiency of such an energy release mechanism can be as large as 29 % for the rotating black hole (9) (Blandford and Znajek process (10), (11)), much more efficient than the 'classical' nuclear fusion.

Under the name of AGN wide range of objects having different properties are summarized. According to the current unification theories AGNs have almost the same structure and their various observational properties are related with different viewing angles. One of the main components in the AGN structure is the accretion disk formed when the gas orbits around the central supermassive black hole. The accretion disk is a strong source of thermal emission sometimes observed even at X-ray band. Within 10^3 Schwarzschild radii around the black hole broad lines from the photoionized gas can be

observed while from much more extended regions narrow lines are produced. The strong infrared emission in all AGNs indicates the presence of obscuring matter (torus) along the plane in which the accretion occurs. In some type of AGNs (about 10 % radio-loud objects), from the central source an extremely energetic and highly collimated outflowing plasma structure (jet) can be observed. The plasma in the jet movies with mildly to highly relativistic velocities and often they remain highly collimated up to several hundreds of kilo parsecs (kpc). Depending on the orientation of the jet, the AGNs can be sub grouped in different source classes. For example, when the jet makes systematically larger angles to the observers, the AGNs appear as a radio galaxy. These are interesting sources where the nonthermal emission from both jet and extended components can be investigated (e.g., large scale lobes of Centaurus A (12) and Fornax A (13)). The most extreme type of AGNs is blazar, when the AGNs are seen exactly along the jet axis (a few degrees of inclination angle), due to which the emitted radiation will be Doppler boosted and will appear brighter to the observer. Commonly, the blazars are divided into BL Lacertae (BL Lac) objects and Flat-Spectrum Radio Quasars (FSRQs), where BL Lacs show no sign of emission lines, whereas the FSRQs are more distant, more luminous, and have stronger emission lines.

Blazars are the most interesting subclass of AGNs and their study is fundamental for understanding not only the physics of the jet but also the formation and evolution of the Universe. For example, detecting γ-rays ($> 100\,GeV$) from the distant blazars allows to constrain the density of extragalactic background light photons which represents all the light and radiation accumulated since the beginning of the Universe so it is the indicator of the energetics of the Universe. On the other hand, the short time scale variability of the blazars (sometimes down to a few minutes) provides unique chance to investigate the jet in sub-parsec scales which are crucial for understanding the physics of particle acceleration and emission. As the blazars are the main candidates for extragalactic neutrino emission which was recently strengthened by detecting neutrinos from TXS0506+056 (3), their study with both neutrinos and γ-rays is essential for investigating the hadronic processes in astrophysical environments.

Although AGNs and their different types were always investigated since their discovery, there are various open issues to understand their physics. For example, even if the jets are

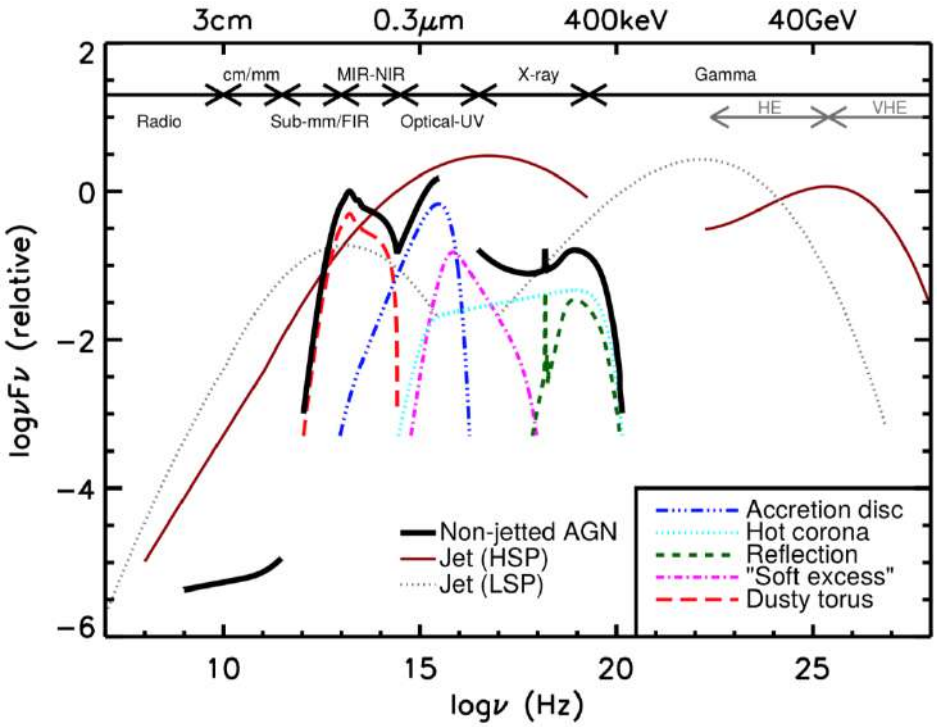

Figure 1.2. Schematic representation of SED of AGNs with and without jets. The contribution of different components is highlighted in colors (14).

observed their connection to the central sources and propagation are still under the discussion. Once the jet is formed, it is still unclear their impact on the environments where they propagate or the mechanisms which accelerates the electrons and protons. Even if the photons from radio to VHE γ-rays are observed, they are not enough to reveal the particle content of the jet (the ratio of proton/electron densities) which is necessary to understand the collimation of the jets, etc. Each of these should be clearly investigated in order to truly understand the phenomena of the AGNs.

There are various methods which are applied to study the mentioned problems. The progress of theoretical astrophysics in understanding various processes allowed developing numerical simulation techniques to follow the jet from the beginning up to its termination point. For example, the impact of the jets on the environment where they propagate and their collimation and propagation can be investigated by realistic high-resolution simulations of the jets. By three-dimensional general relativistic magneto-hydrodynamic simulation of

jet formation from an accretion disk allows to investigate their launching and acceleration. Of course, the simulations are a powerful tool for investigating different properties of the jet but they require initial parameters which can be obtained only from observations and theoretical modeling of the results. For example, the observations in radio band are unique to probe their morphology and the internal structures of the jet or the monitoring in HE γ-ray bands allows following the evolution of the system in time. On the other hand, the theoretical modeling of the broadband emission spectra will allow to estimate or at least constrain several important parameters, such as emitting particle energy density and distribution, magnetic field, etc., which are necessary to investigate the physics of the jets. Therefore, the high quality of the observed multiwavelength data and their theoretical modeling has become one of the most actively discussed topics in modern astrophysics. As mentioned above, the modeling of multiwavelength spectra of blazars is a powerful method to investigate the physics of blazar jets. In fig. 1.2, schematically is shown the broadband SED of AGNs with and without jet. As one can see, non-jetted AGNs are characterized by a faint nonthermal emission spectrum which is sometimes dominated by different components and it extends only up to X-ray band. Alternatively, blazars (as a representative class of AGNs with jet) are characterized with a strong nonthermal emission from radio to VHE γ-ray bands. Since the blazar jets are closely aligned to the observers their emission is amplified due to Doppler boosting and it appears brighter for the observer and almost always the nonthermal emission of the jet dominates over the other components. This nonthermal emission is characterized by two broadband humps, one in the infrared-optical spectral range (low energy) and the other in the MeV-GeV band (HE component). While the nature of the first component is relatively well known; it is well explained by synchrotron emission of relativistic electrons in the magnetic field (supported by the observed strong polarization) there are various theories proposed/applied to explain the second component. These theories are divided into leptonic and hadronic depending on the particles which produce the emission. In the leptonic interpretation, the accelerated electrons interact with various photon fields and the second component is formed. Instead in the hadronic models, the HE component entirely or partially is dominated by the interaction of protons with the

magnetic field, low energy photons or protons. Currently, one of the actual problems in the blazar research is to identify the nature of the HE component.

Blazars are dominant extragalactic sources in the HE and VHE γ-ray bands. In the most recent eight-year *Fermi* LAT point source catalogue there are more than 2940 identified or associated blazars. This implies that these blazars are continuously monitored in γ-ray band since 04 August 2008 which is crucial for the investigation of the origin of their variable emission. Moreover, combining this with the available data at low energy band will allow selecting simultaneous SEDs in the flaring and quiescent states necessary for the theoretical modeling. This implies that from single source study numerous time resolved SEDs can be constrained and used in the theoretical modeling. This allows not only to test various emission processes but also to propose new mechanism responsible for blazar multiwavelength emission.

Now, with the available data, the evolution of the broadband emission from blazars can be followed in physically reasonable timescales. In the theoretical modeling of blazar emission two most actual problems are 1) identifying processes responsible for the time averaged emission from radio to HE/VHE γ-ray bands and 2) finding a model which can explain time evolution of SEDs that is physical connection between the emission in different states (flaring and quiescent). These are ambitious and very complicated problems but are the ultimate goals of any currently developing and proposed theories. In principle, these two problems are linked: in order to find a unique dynamical evolving radiative model to explain the overall emission from blazars it is necessary to be able to explain the emission in different states which then can be generalized within one single emission scenario. In other words, in order to understand the global emission processes in the jet, initially the empirical models explaining the SEDs at any given period should be very well investigated. This will also provide most detailed information on the jet parameters and their evolution time which are necessary for developing a self-consistent radiation model.

Up to now various theories and models were proposed to explain the observed multiwavelength emission from blazars. Most of them were successful in explaining the multiwavelength spectra in a given period but usually they fail to model the SED observed

in another period. This is normal since these models do not include physical connection between different states of the jet and are meant only to understand the emission observed at a given period. Moreover, sometimes the problems are even more complicated: two different models or the same model with another set of free parameters can equally well explain the observed date which introduces significant difficulties for theoretical modeling. Since the main aim of the applied theoretical models is to gain as much as possible information from the observed spectra various statistical methods should be applied to compare different models or to find the set of free parameters which statistically better explain the observed data. The latter one is especially important as finding the parameters best explaining the data allows direct insight into the processes ongoing in the jet and constraining the parameters describing the jet. This implies that successful application of any theoretical model should also contain effective optimization of model free parameters. Since the models have nonlinear dependence from the model free parameters the effective optimization of the parameters is not a trivial task. There are various methods which can be used to find best description of the data one of the simplest one being calculation of chi-squares (χ^2) when the data and the models are compared. However, it is well known that the models with many free parameters are best optimized by Markov Chain Monte Carlo (MCMC) method. Running MCMC samplers allows finding the best-fit and uncertainties of the model free parameters. Due to the recent developments in high performance computing now the MCMC samplers with high number of steps can be used so most precise results can be obtained.

The aims of the thesis are:

- Study particle acceleration and emission processes in the jets of blazars.
- Investigate jet accelerated particle emission spectra as well as their variation when emission region moves different distances from the central source.
- Develop a numerical package for fitting multiwavelength SEDs of blazars which uses various statistical methods for model free parameter estimation.
- By modeling the observed SEDs in the quiescent and flaring periods, investigate the origin of emission from the jets of FSRQs which are detected in VHE γ-ray band.

- Investigate HE and VHE processes in the jet of distant blazar PKS 1441+25 ($z = 0.939$) which resulted in the detection of VHE γ-rays by MAGIC and VERITAS telescopes.
- Investigate the origin of bright flares of CTA 102 observed in the optical, UV, X-ray and γ-ray bands, during 2016-2018.

Scientific novelty

- A numerical code for fitting the multiwavelength SEDs of blazars has been developed. The code uses an MCMC method for model-free parameter estimations and allows finding the parameters which statistically better explain the observed data.
- It is shown that the flares of PKS 1510-89, PKS 1222+216 և 3C 273 can be explained assuming the emission region is outside the BLR and HE/VHE γ-ray emission is mostly due to inverse Compton (IC) scattering of IR photons from the torus.
- It is shown that PKS 1441+25 blazar was flaring on January 24, when the flux increased up to $(2.22 \pm 0.38) \times 10^{-6}\ photon\ cm^{-2}s^{-1}$. From 2015 April 13 to April 28, the MeV-to-GeV photon index has hardened and changes in the range of $\Gamma = (1.73 - 1.79)$ for most of the time with the hardest photon index of $\Gamma = 1.54 \pm 0.16$ observed on MJD 57 131.46 which is not common for FSRQs.
- The modeling shows that there is a hint of hardening of the low-energy index (1.98 ± 0.03) of the underlying non-thermal distribution of electrons responsible for the emission in 2015 April when the source was observed in the VHE γ-ray band.
- It is shown that CTA 102 blazar was in the flaring state from November 2016 up to February 2017 almost in all energy bands. For example, on December 16 within 4.31 minutes the corresponding isotropic γ-ray luminosity was $L_\gamma = 3.25 \times 10^{50}\ erg\ s^{-1}$, comparable to the highest values observed from blazars so far. It is shown that in the X-ray and γ-ray bands follows harder-when-brighter behavior and the shortest time for flux variation was $4.08 \pm 1.44\ hr$.
- By modeling, it is shown that the high-energy data are better described when the infrared thermal radiation of the dusty torus is considered. In the flaring periods when the correlation between the γ-ray and UV/optical/X-ray bands is lacking, the γ-ray

emission can be produced from the interaction of fresh electrons in a different blob, which does not make a dominant contribution at lower energies.

The thesis is structured as follows: in **Chapter 1** different types of AGNs, their main properties and components are presented and discussed. Relativistic transformation (Doppler boosted) of varies quantities from the jet to observer frame are presented.

In **Chapter 2** the main emission mechanisms of accelerated electrons (synchrotron and IC scattering) in the relativistic jets are briefly summarized. For the IC scattering various internal and external photon fields are considered and discussed.

In **Chapter 3** the main theoretical background of MCMC optimization of model free parameters and the fitting technique is described. Step by step the sampling of likelihood distribution of model free parameters and their optimization with MCMC is presented. The application of MCMC method in the modeling of blazar SED is described, the structure of the code, its main components and working principles are described in details. The application of the code is demonstrated by modeling the SEDs of two well-known blazars Mkn 501 and PKS 0537-441. Within two different emission scenarios the main parameters of the emitting electrons and the jet parameters are estimated. Then the code is used to model the emission from FSRQs up to now detected in the VHE γ-ray band (PKS 1510-089, PKS 1222+216 and 3C 279). The emission spectra in several flaring and quiescent periods are modeled and the parameters characterizing the emitting electrons and the jet in these two periods are estimated and compared.

In **Chapter 4** the origin of the multiwavelength emission from PKS 1441+25, one of the most distant FSRQ detected in the VHE γ-ray band so far ($z = 0.939$), is investigated. Using HE γ-ray data accumulated from January to December of 2015 quiescent and flaring periods of the source are selected and modeling with one-zone synchrotron/synchrotron self-Compton (SSC) and/or external inverse Compton (EIC) emission scenarios. The origin of the flares is interpreted as change in the location of the emitting region which is either due to the change in the bulk Lorentz factor or due to the change of the location of the emitting region and due to the magnetic field amplification. The results from the modeling

of SEDs observed during the bright flare in January and when the source was emitting VHE γ-rays are compared and discussed.

In **Chapter 5** the origin of broadband emission from another distant blazar CTA 102 ($z = 1.037$) is investigated. The data accumulated from NuSTAR, Swift UVOT/XRT and Fermi LAT observations of CTA 102 during the active periods in 2016-2017 are analyzed and used to constrain SEDs before, during and after the flares. One and two zone leptonic models are used to model the SEDs when contemporaneous or no contemporaneous flux changes in optical, X-ray and γ-ray bands are observed. Considering all relevant photon fields for IC scattering (synchrotron, BLR reflected and torus photons) the SEDs are modeled considering different location for the emitting region.

In **Conclusion** the main results obtained in the thesis are summarized as well as its possible application in current blazar research is demonstrated and briefly the future continuation of the work is discussed.

Chapter 1

1. OBSERVATIONAL PROPERTIES OF BLAZARS

1.1. AGN multiwavelength survey

The recent technological developments enabled to observer and study AGNs in various energy bands (namely in radio, infrared, optical, ultraviolet, X-ray and γ-ray bands). The observations in the individual bands give us insights into different physical processes occurring in AGNs. Each band of observed electromagnetic spectra (i.e. radio, optical, γ, etc.) reveal specific observational features, meanwhile the combination of all observable spectra gives more comprehensive picture of central engine, jet formation and content, physics and nature.

As some of AGNs are powerful radio emitters the radio observations contain significant information. The distinct sensitivity of radio telescopes and smaller angular resolution (e.g., when interferometry is used) allows not only to observe very distant objects, such as AGNs at $z > 7$ redshift but also make detailed investigation of their structure and morphology. Also, the radio observations contain valuable information on the relativistic bulk motions, dynamics of various components and morphology of AGN jets. The main AGNs division being either a radio -loud or –quiet, is based on the radio luminosity ratios to optical one, once more stresses the importance of radio observations.

Infrared observations can help to understand the non-thermal radiation from the jet as well as the thermal radiation produced from a dusty torus surrounding the central source. Understanding the absorption, emission and geometrical properties of the dust in AGNs is one of the central questions in AGN physics.

Optical/UV observations can provide information especially about disk thermal radiation, absorption and emission lines of broad and narrow line regions (henceforth BLR and NLR). The most observational data are collected from AGNs optical survey. Optical/UV observations allow studying the core of AGNs and as farther the host galaxy as brighter the

AGN core luminosity, hence is easier to observe AGN core and distinguish it from the host galaxy.

X-ray observations are carried out only by satellite base telescopes, as the Earth's atmosphere is opaque for the X-ray photons. X-ray emission from AGNs is mostly of nonthermal origin produced from the jet but sometimes also direct thermal emission from accretion disc can be observed as well. In the X-ray band, currently or past operating telescopes discovered more than thousands of AGNs. The observations in the X-ray band are crucial for understanding the origin of emission from different components in AGNs emission spectra.

As AGNs are the dominating extragalactic sources on the γ-ray sky, their observations in the γ-ray band are crucial for understanding their physics. One of the best instruments for studying the γ-ray sky is *Fermi* LAT which is sensitive to photons in the energy range from 100 (20) MeV to 300 GeV which allows continuous monitoring of γ-ray emitting sources more than 10 years. The photons with energy above 100-300 GeV can be only effectively observed with ground-based Cherenkov telescopes, such as MAGIC, H.E.S.S, VERITAS and CTA (under the construction). By these telescopes the photons with energies up to tens of TeV can be observed constraining the highest tail of the non-thermal emission spectra. Also, the observations in the γ-ray band are crucial for distinguishing various emission components in the AGN spectra.

The multiwavelength observations allow to have comprehensive view of ongoing physical processes and can help to understand the jet physics (e.g. their launch, propagation, kinetics, content, etc.), as well as processes responsible for particle acceleration, distribution, propagation and emission.

1.2. Classification of AGNs

Despite there are large number of AGNs classified up to now, they show some common features. Based on the observational properties, the AGNs can be classified in different ways: by their radio emission power (loudness), properties at optical/UV emission spectra, etc.

The radio loudness is defined as the ratio of radio and optical fluxes at $5\,GHz$ and B-bands, respectively, and if the ratio is bigger than 10, the AGN is classifies as radio loud, otherwise radio quiet. The examples of radio quiet AGNs are Seyfert 1 (Sy 1) and Seyfert 2 (Sy 2), quasars, etc., while the radio loud class includes FR 1 and FR 2 type of radio galaxies, BL Lac and FSRQ blazars, etc. (see in fig. 1.3).

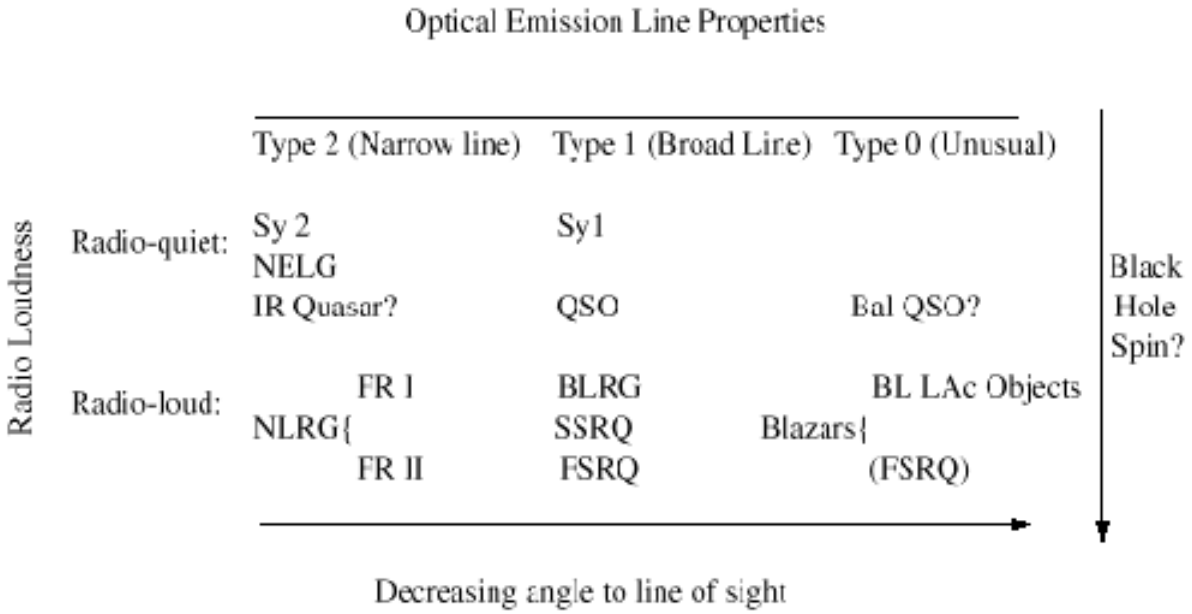

Figure 1.3. AGN taxonomy (15).

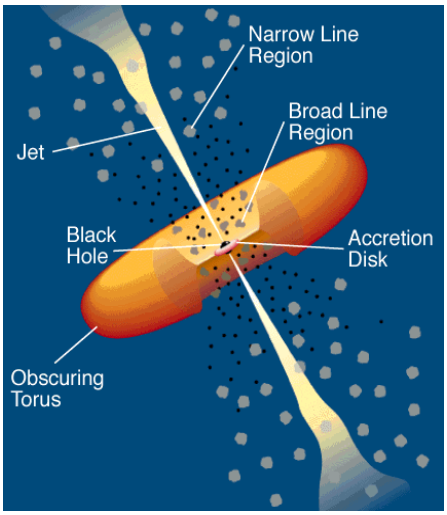

Figure 1.4. AGN compounds.

According to the features at optical/UV spectrum, the whole population of AGNs can be divided into three large groups. The first group (Type 1) is characterized by bright continua and broad emission lines (15). Among the population of Type 1 AGNs, the radio quiet Sy 1 and QSO galaxies are included, which have low and high luminosities and are typically observed at near and large distances, respectively. In the case of radio loud population, two sub-groups, the low- luminosity broad line region galaxies (BLRG), and high- luminosity step spectrum radio quasar (SSRQ) and FSRQ are included (15). Unlike the Type 1 group of AGNs, Type 2 is characterized by a weak emission continuum and only narrow emission lines are observed (BLR either being obscured or missing). In the Type 2 group radio quiet

and loud sources are included. From the radio quite objects, low luminous object such as Sy 2 and high luminous objects such as narrow-emission-line X-ray galaxies (NELG) are included. Radio loud objects are narrow-line-radio-galaxies (NLRG), which are conventionally divided into Fanaroff-Riley (FR) type 1 and FR type 2 galaxies, based on their morphologies. The FR 1 objects typically have symmetric jets, whose brightness falls along the jet moving off the central engine. Alternatively, FR 2 class objects are well-known by their more collimated jets, lobes with bright hot spots (15).

The third, more extreme type (Type 0) of AGNs are characterized with high polarization, short and strong variations both in time and amplitude, and their radio loud sub-classes are divided largely into BL Lacs and FSRQs sources, based on their emission line features, i.e., the lines are either narrow ($< 5^{\circ}$) or missing in BL Lacs objects, instead, very broad emission lines ($> 5^{\circ}$) with a strong thermal component are typically observed in FSRQs.

The unified theory of AGNs proposed by (15), is the most popular model. According to this unified theory, all AGNs have the same inner structure, i.e. accretion disk, BLR and NLR, dusty torus and relativistic jets, and their observed different properties are explained as the result of different orientation of the source in respect to the observer. In this model, if an AGN is observed edge-on to the observer line of sight, i.e. close to the torus plane, the direct radiation from accretion disk and BLR is obscured by the torus, and only narrow lines are observed. Those objects are classified as Sy 2 or narrow line region galaxies (NLRG) for radio quiet and loud cases, respectively (see in fig 1.4). Changing the viewing angle of the jet, in addition to the NLR, also the emission from BLR can be observed. These objects, which make some angle in respect to the torus plane are called either Sy 1 or BLRG depending on their radio quietness and loudness, respectively (see in fig 1.3). Finally, the AGNs which are observed face-on (i.e., which makes small angle) in respect to the observer are classified as blazars (see in fig 1.3).

1.3. Relativistic effects in AGNs: Beaming and Doppler boosting

In the objects when the plasma is moving with relativistic velocities (e.g., the jets of blazars) the relativistic effects are starting to play crucial role. In these systems, when the time, size, emission luminosity etc. are being computed the relativistic effects should be taken into consideration. In the innermost part of blazar jets, usually peculiar phenomenon of superluminal motion can be observed, when the velocity of bright (emitting) regions are estimated to be larger than the speed of light (c). This phenomenon was first predicted by Martin Rees in 1996 and then observed in 1997 by Very Long Baseline Interferometer (VLBI) at radio frequency. In order to explain the effect of superluminal emission the fig. 1.6 is used.

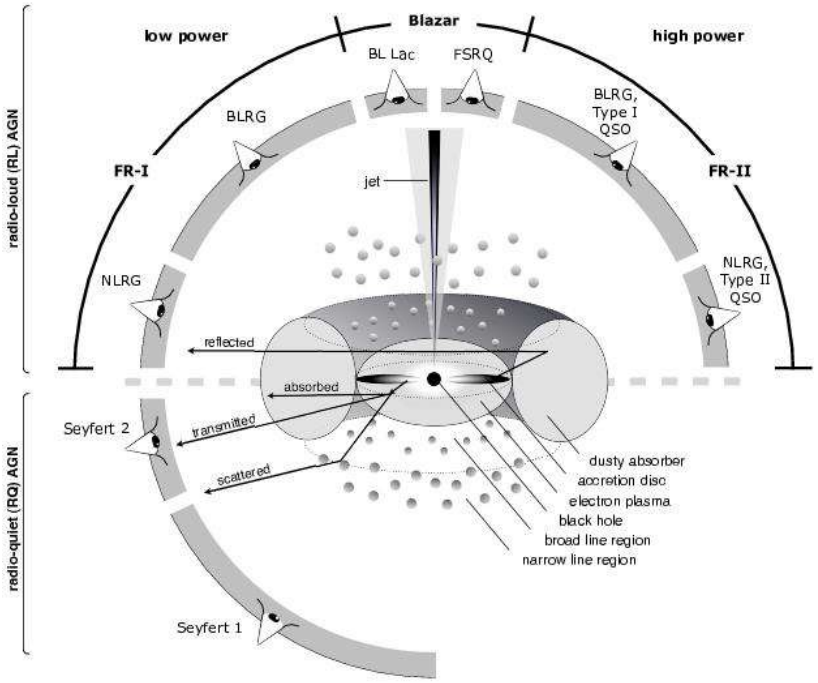

Figure 1.5. Classification of AGNs by viewing angle (7).

Assume we have a source moving with a relativistic velocity V which forms θ angle in respect to the observer. Considering two instant emissions (pulses) from the source at two different positions "S" and "T" (see in fig 1.6), and the travel time between them is Δt. The first pulse will travel a distance of cΔt when the second pulse will leave the source at the

position of "T". So, the observer will measure the time lag between the pulses equal to $t_{obs} = c\Delta t - v\Delta t \cos\theta$, and an apparent velocity of the source is

$$v_{app} = \frac{v\Delta t\, sin\theta}{c\Delta t - v\Delta t\, cos\theta} = \frac{\beta c\, sin\theta}{1 - \beta\, cos\theta}. \quad (1.1)$$

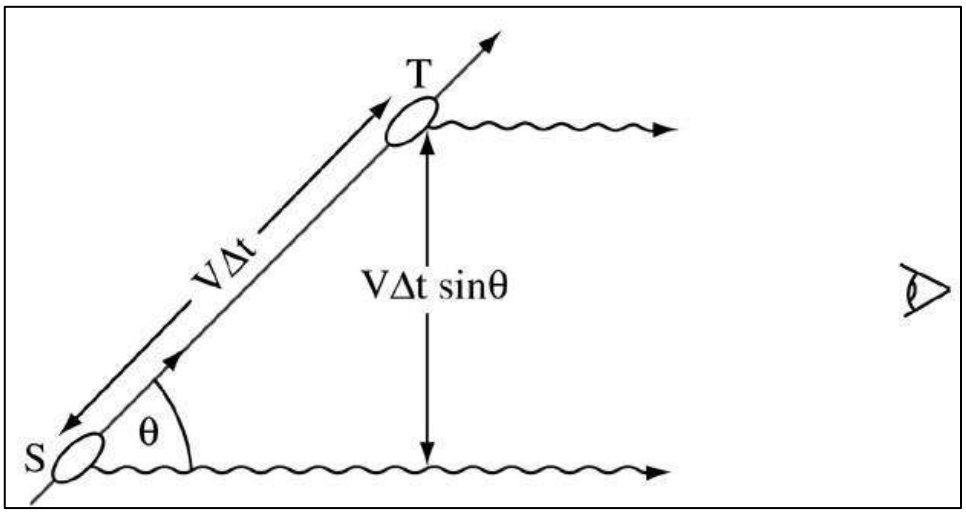

Figure 1.6. Schematic of apparent superluminal motion.

This means, that the observed apparent velocity depends on the speed of the source and angle between the velocity direction and observer's line of sight. It is easy to see, that only if $\theta = 90^{\circ}$ the apparent velocity is equal to the real velocity of the source. For small angles apparent (observed) velocity can be larger than the speed of light.

The non-thermal emission from blazars originates in the regions moving with relativistic speeds and form small angles in respect to the observer's sight, therefore besides the usual Lorentz transformations a Doppler factor (δ) also should be considered, which is related to the velocity and viewing angle of the emitting region. From Lorentz transformations the Lorentz factor is $\Gamma = \frac{1}{\sqrt{1-\beta^2}}$, where $\beta \equiv {}^{v}/_{c}$. The Doppler factor in the relativistic case has a form of $\delta = \frac{1}{\Gamma(1-\beta cos\theta)}$, where θ-is the angle of emitting region moving vector direction with respect to the observer. When the quantities are transformed from the rest frame to the observer frame the Doppler factor should be taken into account. One of the primary measurable quantities is the flux which is linked to the luminosity by $F = 4\pi D^2 L$, where D is the distance from the source. The luminosity is defined as the radiated energy per second

$[erg\ s^{-1}]$. The bolometric luminosity is an integral of monochromatic luminosity (luminosity per unit of frequency) which gives the total luminosity emitted in all bands:

$$L_{bol} = \int_0^\infty L(\nu)\, d\nu \tag{1.2}$$

Going from the rest to the observed frame the bolometric luminosity (flux) is amplified by δ^4. The energy/frequency will be increased by δ $(\nu = \delta\nu')$. Another important quantity is radiative energy density u $[erg\ cm^{-3}]$. Radiative energy density is a radiated energy per volume of space. In order to calculate the radiative energy density of a spherical source, with the luminosity of L and size R, two different scenarios are considered:

A. The observer is outside the source, at the distance of D >> R

B. The observer is inside the source, which emits uniformly

Case A: Let us consider the observer is at the distance of D >> R from the source. The shell with the width of $dD = cdt$ will have $dV = 4\pi D^2 cdt$ volume, and in the time of dt the source will emit $dE = Ldt$ amount of energy (see in fig. 1.7). The radiative energy density will be:

$$u = \frac{dE}{dV} = \frac{Ldt}{4\pi D^2 c\, dt} = \frac{L}{4\pi D^2 c} \tag{1.3}$$

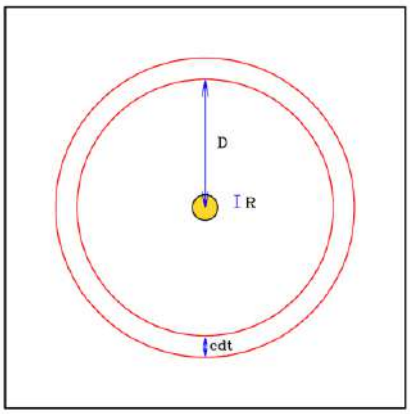

Figure 1.7. Schematic depiction of a source with radius R which emits a luminosity L (16).

The equation is valid also for a uniformly emitting shell, as the energy density is the same in any location inside the shell (16).

Case B: For a case, when the observer is inside a uniformly emitting source, let us assume that the source is optically thin and homogeneous. In such case, the energy density will be proportional to the mean escape time of photons from the source ($u \sim \overline{t_{esc}}$). The mean escape time will be less than R/c, since the photons, originated near the sphere boarders, will leave the source immediately with the probability of 1/2 and a probability less than 1/2 to pass 2R distance. Hence, the mean probability for the sphere will be $\overline{t_{esc}} \approx \frac{3}{4} R/c$, and the radiative energy density is

$$u = \frac{E}{V}\overline{t_{esc}} \approx \frac{3L}{4\pi R^3}\frac{3}{4}\frac{R}{c} = 2.25\frac{L}{4\pi R^2 c}. \quad (1.4)$$

It is worth to note, that the Eq. 1.4 is valid only for optically thin sources (16). The Lorentz transformation for the radiative energy density is (16)

$$u = \delta^2 u'. \quad (1.5)$$

In the Table 1.1 transformation of some quantities from the rest to observer frame is presented.

Table 1.1. Useful transformations.

Frequency	$\nu = \delta\nu'$
Time	$t = t'/\delta$
Volume	$V = \delta V'$
Radiation flux (νF_ν)	$F = \delta^4 F'$
Radiation energy density	$u = \delta^2 u'$

1.4. Blazars: Broadband spectrum

Blazars are the most interesting and extreme class of AGNs. Blazars are the most luminous persistent sources in the Universe, that is why they are observed even in large distances ($z > 7$). According to the unified theory, blazars are AGNs which have jets that are oriented at a small angle to the line of sight of the observer (15). They are characterized by the extreme variability in both amplitude and time (as short as minutes e.g. (17) (18) (19)), strong polarization from radio to optical wavelengths (20) (21), superluminal motion, and very high luminosities (e.g. bolometric luminosities of some blazars exceed 10^{49} $erg\ s^{-1}$) and usually have core-dominated radio structures. The short variability indicates

the compactness of the emitting region. The central source produces collimated outflows with the bulk Lorentz factor typically in the range of $10 - 20$. Therefore, the emission from blazars is affected by relativistic beaming so they are significantly brighter in the observer frame.

Blazars conventionally are divided into two sub-classes, based on their observational features. BL Lac objects exhibit extremely narrow (equivalent width $< 5\text{Å}$) or no emission lines which might be associated with the low accretion rate onto the supermassive black hole, unlike FSRQs where in the optical/UV band very broad lines are observed and they are generally more powerful. The accretion disks of FSRQs are so powerful, that sometimes the thermal radiation dominates over the non-thermal component. Depending on the peak of the synchrotron emission (low component), blazars can be further divided into low- (LSP: $\nu_S < 10^{14}\,Hz$), intermediate- (ISP: $10^{14}\,Hz < \nu_S < 10^{15}\,Hz$) and high-synchrotron-energy peaked sources (HSP: $\nu_S > 10^{15}\,Hz$) (22). The synchrotron peaks of most BL Lac objects are found within $10^{14} - 10^{17}\ Hz$, in contrast to FSRQs case which are typically LSP blazars and tend to exhibit more power in the γ-ray band.

Blazars have been subjects of investigation since their discovery, but several crucial problems for understanding their physics are still unclear. For example, how the jets are formed and remain collimated over large distances, what are the particle acceleration and emission processes, where does the emission originate along the jet? etc. The exact origin of emission from blazar jets is still under debate. The electromagnetic emission from blazars is observed in a wide energy range from radio to HE γ-ray bands. This broadband emission is predominantly of a nonthermal origin, although, sometimes, thermal emission from some components can be also observed. The broadband SED of blazars has two nonthermal peaks - one at optical/UV or X-rays (the low-energy component) and the other at higher energies (the γ-ray band). The observed high-degree polarization indicates that the low-energy component is most likely due to the synchrotron emission of electrons accelerated in the jet. While the synchrotron emission can explain the observed features of the low-energy component, the origin of the HE component is still unclear, so various models/scenarios were proposed. One of the most widely applied models is that the HE

component is produced via IC scattering of soft photons being either internal (e.g., synchrotron photons; SSC (23) (24)) or external: EIC (25) (26) to the jet. These models have been successful in explaining the SEDs of blazars but sometimes fail to reproduce some observed features. As a distinct alternative, models involving the radiative output of protons accelerated in the jet (hadronic models) were proposed (27) (28). The protons carry significant amount of energy and the exact estimation of their content in the jet can be crucial for understanding the physics of the jet. Even in the leptonic scenarios, hadrons (protons) are expected to be present in the jet to ensure the charge neutrality of the plasma. Then these protons can be effectively accelerated and by interacting with a dense target (proton-proton interaction), magnetic (proton-synchrotron) and/or photon fields ($p\gamma$ interaction) produce the observed HE component. In the case of hadronic models, more extreme parameters are required as compared with leptonic models (e.g., in the last two cases the protons should be accelerated beyond $10^{19}\,eV$ and propagate in a magnetic field exceeding $30\,G$ (28) (29) (30)) but in principle these conditions can be formed in the jet and sometimes the hadronic models give better modeling of SEDs (31) (32).

Leptonic one-zone emission scenarios are the most common models applied to explain the broadband emission from blazars. The emitting region is assumed to have a spherical geometry (blob) carrying a magnetic field with an intensity of B and a population of relativistic electrons/positrons. Since the emission region moves along the jet with a bulk Lorentz factor of Γ_{bulk}, the observed radiation will be amplified by a relativistic Doppler factor of $\delta = 1/\Gamma_{bulk}(1 - \beta\, cos(\Theta_{obs}))$, where Θ_{obs} is the jet inclination angle (usually $< 8°$ for blazars). The size of emission region can be constrained by the observed variability time-scale (τ), $R_b \leq \delta\, c\, \tau/(1 + z)$. It has already been noted that blazars are characterized by extreme variability (in both time and amplitude), which implies that the emission region should be very compact. For typical parameters of $t_{var} \sim$ few hours and $\delta \sim 10 \div 20$, the emission region cannot exceed $10^{15} - 10^{16}\,cm$. This implies that blazar observations are unique tools for investigation of the sub-parsec structures of their jets.

As the one-zone models assume the emission is produced from a single population of

electrons, it is expected to have correlated flux changes in various bands (33). However, for some blazars the expected correlations were not observed, so alternative two-zone models were proposed (34). The basic idea of two-zone models is that the multiwavelength emission is produced from two blobs having different size or location along the jet and each containing different population of particles. For example, one of these models assumes that particles are accelerated in one blob, but they emit whenever they are injected in the second blob. As an alternative, in order to explain the rapid variability in the γ-ray band, a model where the emission is produced in two emitting regions of different sizes and distances from the central source was proposed. Of course, two-zone models contain more free parameters, so are easier for modeling, but these are only possibilities, when complex changes of multiwavelength flux are observed. Now in the era of available large amount of multiwavelength data, not only currently known theories can be tested but also new emission models can be proposed. This makes the blazar research one of the hottest topics in astrophysics.

The observations of blazars (especially in the γ-ray band) can help also to understand the formation of the Universe. The detection of distant γ-ray sources is restricted not only by their low emission flux (below telescopes sensitivities), but also the produced photons can be absorbed. They can interact with the photons of diffuse radiation in the universe, so called extragalactic background light (EBL) and produce electron-positron pairs. The density of EBL photon field is composed by the light emitted since the formation of the Universe (stars, galaxies etc.) and it contains valuable information on the history of star and galaxy formation. The EBL density cannot be measured directly and it can be done only indirectly, namely when the γ-ray emission from a very distant blazar is observed, it can help to measure the limit of EBL photon density. Especially are important the observations of very distant blazars with *Fermi* LAT and ground based Cherenkov telescopes (MAGIC, VERITAS, HESS) so combining the data in the MeV/GeV (unabsorbed) and TeV (absorbed) bands can help to constrain the density of EBL. This once more emphasizes the importance of studying blazars in general and the origin of their emission in particular.

Chapter 2

2. EMISSION MECHANISMS OF BLAZARS

Here, the main processes responsible for nonthermal emission in blazars are discussed. Since the physical processes in blazars are taking place under the extreme conditions (e.g. relativistic velocity, large magnetic fields etc.), the investigation/understanding of particle acceleration and emission mechanisms occurring in these sources is one of the most important topics in the modern astrophysics. The main emission mechanisms of electrons, synchrotron radiation and IC scattering, are presented and discussed.

2.1. Synchrotron radiation

The low component of a blazar multiwavelength spectrum, ranging from radio to optical/UV and/or X-ray band, is well described by the synchrotron emission of relativistic electrons. The synchrotron emission is produced when electrons are spiraling around the jet's magnetic field lines. Equation of motion of an electron in a magnetic field is

$$\frac{d(\gamma m\vec{v})}{dt} = \frac{e}{c}[\vec{v} \times \vec{B}], \tag{1.6}$$

where $\vec{v}$- is the vector of an electron velocity and γ- is the Lorentz factor, e is the electron charge, B is the magnetic field, m_e is the electron rest mass. Since the electron spiraling around the magnetic field lines, the force on the electron is perpendicular to the motion and the magnetic field does not do work on the electron, therefore its speed remains constant, i.e. $|\vec{v}| = \text{const}$. The electron velocity is constant, but its direction may change. Let us consider the directions perpendicular and parallel to the magnetic field $\vec{B}$. Let v have components $v_{\perp}$ and $v_{||}$ along these directions. Then

$$\frac{dv_{||}}{dt} = 0 \tag{1.7}$$

and

$$\frac{dv_{\perp}}{dt} = \frac{e}{\gamma mc}\left[\vec{v} \times \vec{B}\right] \tag{1.8}$$

Eq. 1.8 can be rewritten as

$$a = \frac{e}{\gamma m}\beta B \sin\theta, \tag{1.9}$$

where θ is the so-called pitch-angle or the inclination of the velocity vector to the magnetic field lines and $\beta \equiv \frac{v}{c}$.

An electron emitting synchrotron radiation loses some amount of energy which at unit time (radiation power) can be calculated from Larmor formula:

$$P(t) = -\frac{dEe}{dt} = \frac{2e^2 a'^2}{3c^3}\gamma^4 = \frac{2e^2(a_{\perp}'^2 + a_{\parallel}'^2)}{3c^3} = \frac{2e^2 a^2}{3c^3}\gamma^4, \tag{1.10}$$

by taking into account $a_{\parallel}' = 0$ and Lorentz transformation of $a_{\perp}' = \gamma^2 a_{\perp}$ (35), where primed quantities refer to the rest frame of particles and non-primed quantities to the observer's frame. Inserting (5) into (6) for synchrotron radiation loses one will obtain:

$$\frac{dEe}{dt} = \frac{2e^2 a^2}{3c^3}\gamma^4 = \frac{2e^2}{3c^3}\gamma^4\left(\frac{e\beta B}{\gamma m}\sin\theta\right)^2 = \frac{2}{3}r_0^2 c\beta^2\gamma^2 B^2 \sin^2\theta, \tag{1.11}$$

where $r_0 = \frac{e^2}{m\,c^2}$ is the classical electron radius. For an electron population we can assume an isotropic distribution of pitch angles and average $\sin^2\theta$ over the solid angle

$$\overline{\sin^2\theta} = \frac{2}{3}. \tag{1.12}$$

Taking into account Eq. 1.11 and Eq. 1.12 also $\beta \approx 1$ and assignments of $U_B = \frac{B^2}{8\pi}$ magnetic field energy density and $\sigma_T = \frac{4\pi {r_0}^2}{3}$ - Thomson cross-section the energy loss rate of electrons can be rewritten as:

$$\frac{dE_e}{dt} = \frac{4}{3}c\sigma_T\gamma^2 U_B = 1.29 \times 10^{-9} B^2\gamma^2\ s^{-1} \tag{1.13}$$

and the corresponding cooling time will be

$$t_{syn} = \frac{E_e}{\frac{dE_e}{dt}} = \frac{3}{4}\frac{8\pi(m_e c^2)^2}{EeB_0{}^2\sigma_T c}. \tag{1.14}$$

The Eq. 1.14 shows that the higher energy particles loss energy faster. It is demonstrated in the fig. 2.1 where the cooling times of an electron in 1 and 0.1 G magnetic fields are shown.

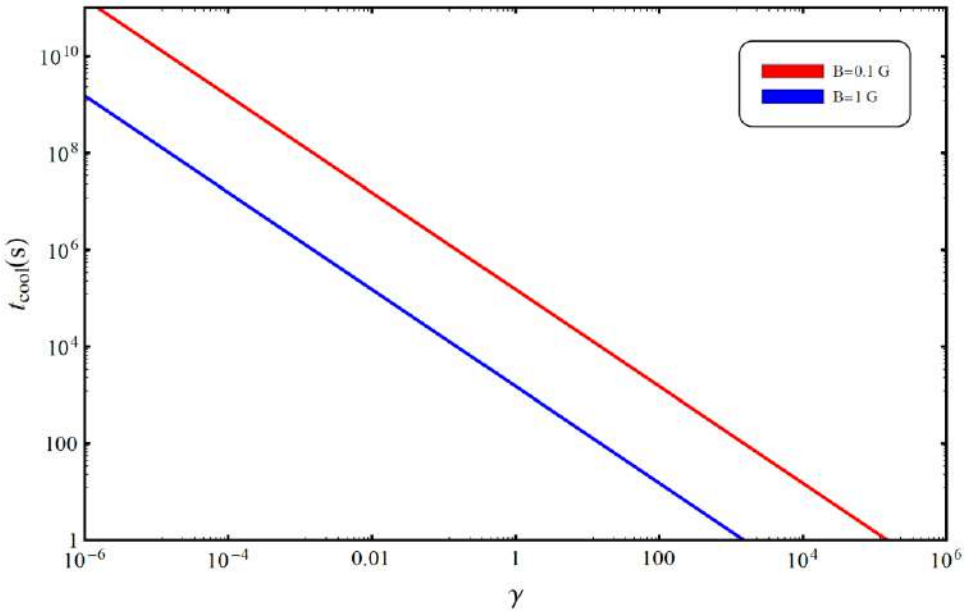

Figure 2.1. The cooling times of an electron in $B = 0.1\ G$ and $B = 1\ G$ magnetic fields.

Eq. 1.13 shows the energy loss rate of an electron when it emits via synchrotron radiation. When the electrons emit photons via the synchrotron emission, the amount of energy that they lose is being transferred to photons. For a single emitting electron with energy E_e in the magnetic field B, the emitted photons will have characteristic frequency (ν_c) of

$$\upsilon_c = \frac{3eB}{4\pi m_e c}\left(\frac{E_e}{m_e c^2}\right)^2 \tag{1.15}$$

and the differential energy spectrum can be computed from

$$\frac{dN_\gamma}{dE_\gamma dt} = \frac{\sqrt{3}}{2\pi}\frac{e^3 B}{m_e c^2 \hbar E_\gamma} F\left(\frac{E_\gamma}{E_c}\right) \tag{1.16}$$

where, $F(x)$ is defined by

$$F(x) = x\int_x^{inf} K_{5/3}(x')dx', \tag{1.17}$$

where $K_{5/3}$ is the modified Bessel function of the order of $5/3$ (36).

In the numerical calculations is more convenient to use an approximation of $F(x)$. This can be approximated by

$$F(x) \approx 2.15x^{1/3}(1+3.06x)^{1/6}\,\frac{1+0.884x^{2/3}+0.471x^{4/3}}{1+1.64x^{2/3}+0.974x^{4/3}}e^{-x} \tag{1.18}$$

which provides better than 0.2% accuracy over the entire range of the variable x. However, in a case of chaotic magnetic field, the Eq. 1.16 should be averaged over directions of magnetic field and $F(x)$ should be replaced by

$$G(x) = \frac{x}{20}\left[(8+3x^2)\left(k_{1/3}\right)^2 + xk_{2/3}\left(2k_{1/3}-3xk_{2/3}\right)\right], \tag{1.19}$$

where $k_{1/3} = K_{1/3}(x/2)$, $k_{2/3} = K_{2/3}(x/2)$. The Eq. 1.19 expression in its turn can be approximated by (36)

$$G(x) \approx \frac{1.808\,x^{1/3}}{\sqrt{1+3.4x^{\frac{2}{3}}}}\frac{1+2.21x^{2/3}+0.347x^{4/3}}{1+1.353x^{2/3}+0.217x^{4/3}}e^{-x}. \tag{1.20}$$

In the fig. 2.2 both functions of $F(x)$ and $G(x)$ are depicted which clearly shows the difference when the magnetic field is averaged or not over the angle.

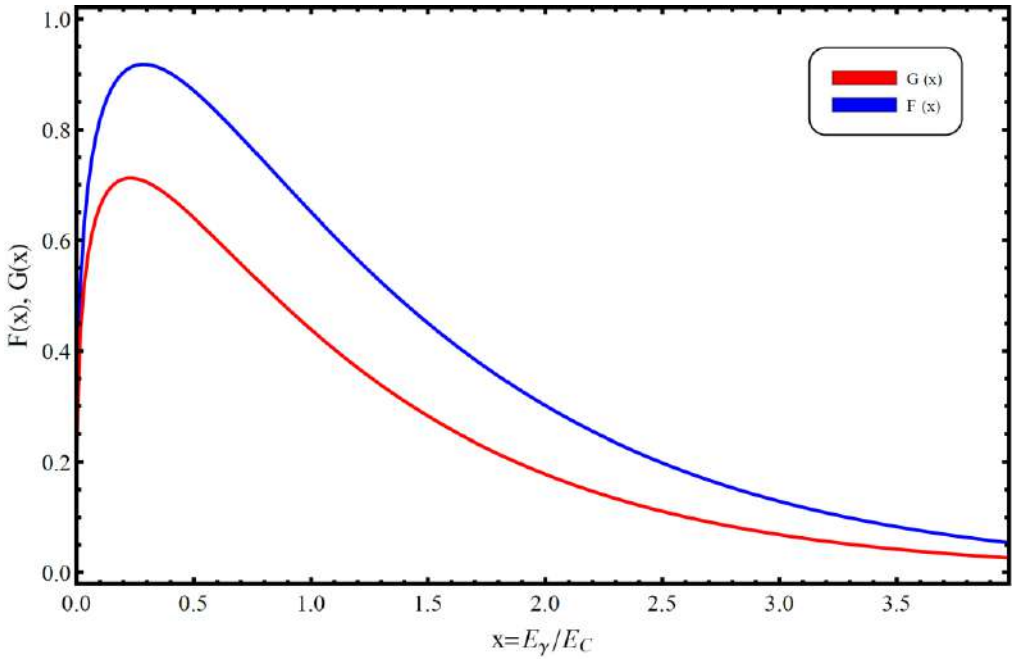

Figure 2.2. The emissivity functions for synchrotron radiation $F(x)$ and $G(x)$.

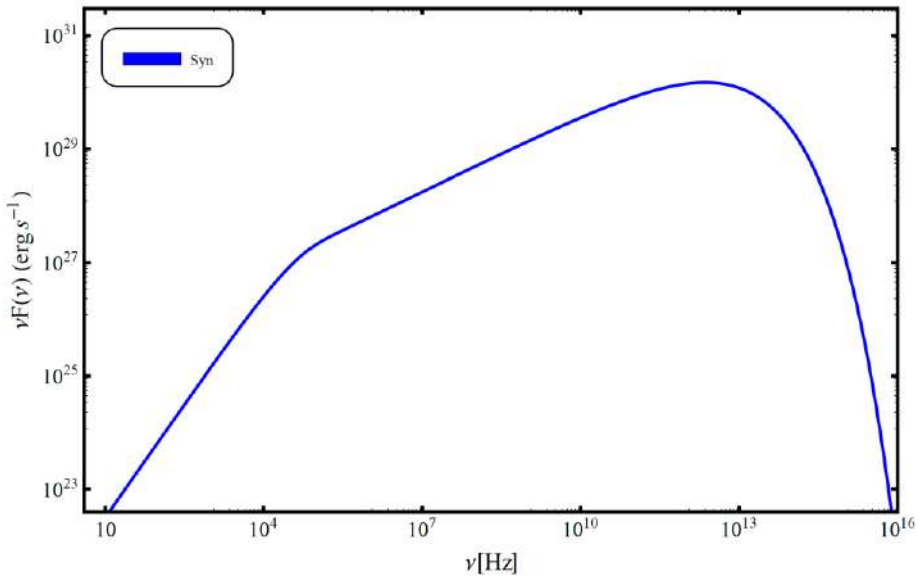

Figure 2.3. Synchrotron $\nu F(\nu)$ emission spectrum.

Above, the emission from a single electron in the magnetic field is discussed, but as in all astronomical sources, also in blazar jets, the emission is produced from population of particles. In order to obtain the differential synchrotron emission spectrum for an electron population, the energy density of the electron population with the single electron spectrum Eq. 1.16 should be integrated over electrons energy:

$$\left(\frac{dN_\gamma}{dE_\gamma dt}\right)_N = \int_{E_{min}}^{E_{max}} \left(\frac{dN_\gamma}{dE_\gamma dt}\right)_1 N(E_e)dE_e, \tag{1.21}$$

for which the luminosity will be

$$\mathrm{L_{syn}} = \mathrm{E_\gamma}^2 \int_{\mathrm{E_{min}}}^{\mathrm{E_{max}}} \left(\frac{\mathrm{dN_\gamma}}{\mathrm{dE_\gamma dt}}\right)_1 \mathrm{N(E_e)dE_e}. \tag{1.22}$$

Assuming the electron energy distribution follows $\sim {E_e}^{-\alpha} Exp[-(E_e/E_{cutoff})]$ law with the electrons total energy of $10^{50}\,eV$, $E_{min} = 0.511\,MeV$, $E_{max} = 5.11\,TeV$, $E_{cut} = 5.11\,GeV$, $B = 1\,mG$, $\alpha = 2.1$, $\delta = 10$ the corresponding spectrum of electron synchrotron emission $(\nu f(\nu))$ is shown in fig 2.3. As one can see, up to the characteristic frequency of photons defined by $\left(\sim \frac{3eB}{4\pi m_e c}\left(\frac{E_{cutoff}}{m_e c^2}\right)^2\right)$ the spectrum follows $\nu^{0.5}$ spectrum (since $f(\nu) = \nu^{-\frac{\alpha-1}{2}}$ for the synchrotron emission) and then starts to decrease when the number of electrons is low

(after E_{cutoff}). This cut-off feature in the electron spectrum sometimes is defined by the X-ray data which allows estimating the maximum energy of accelerated particles from the observations.

2.2. Inverse Compton Scattering

One of the mechanisms to generate HE emission in blazar jets is the IC scattering, when the low energy photons are up-scattered by relativistic electrons. Here, the low energy photon gains additional energy defined by the loss of the electrons. In IC process the cross-section of an electron and a photon interaction depends on the energy of the photon and electron before the interaction and also to the energy of produced photons. Depending on the initial energies of the interacting photons and electrons, the interaction can be either in Thomson or Klein-Nishina regimes. In the Thomson regime the energy of a scattered photon is proportional to γ^2, instead for Klein-Nishina regime it is proportional to γ. In general, if the photon energy before and after interaction is $\varepsilon \text{ and } \varepsilon_1$, respectively, then the differential spectrum of the IC scattering is given by (37):

$$\frac{dN}{dt\, d\varepsilon_1} = \frac{2\,\pi\, {r_0}^2 m_e c}{\gamma^2} \frac{n(\varepsilon) d\varepsilon}{\varepsilon}\, F_c(q, \Gamma_e), \tag{2.1}$$

where

$$F_c(q, \Gamma_e) = \left[2q\, ln[q] + \,(1+2q)(1-q) + \frac{1}{2}\,\frac{(\Gamma_e q)^2}{1+\Gamma_e q}(1-q)\right] \tag{2.2}$$

$$E_1 = \varepsilon_1(\gamma\, m_e c^2), \quad q = \frac{E_1}{\Gamma_e(1-E_1)}, \qquad \Gamma_e = \frac{4\gamma\varepsilon}{m_e c^2},$$

is the total IC scattering cross-section (monochromatic differential cross-section) and $n(\varepsilon)$ is the target photon distribution, γ is the energy of interacting electrons. The Eq. 2.1 is given for one electron and in order to obtain the emission spectrum for electrons population Eq. 2.1 should be integrated over the whole energies of electrons. For the case of isotropic and homogeneous distributions of photons and electrons the luminosity $[erg\, s^{-1}]$ can be calculated by (38)

$$L_{IC}(\varepsilon_s) = \frac{3}{4} c\sigma_T \, \varepsilon_s^2 \int_0^{\infty} d\varepsilon \frac{u(\varepsilon)}{\varepsilon^2} \int_{\gamma_{min}}^{\infty} d\gamma \, \frac{N_e(\gamma)}{\gamma^2} F_c(q, \Gamma_e), \tag{2.3}$$

where $u(\varepsilon) = \varepsilon \, n(\varepsilon)$ and $N_e(\gamma)$ are the photon and electron energy densities, respectively, and ε_s is the scattered photon energy. In the fig. 2.4 is plotted the IC scattering of CMB photons on the electrons, having the same parameters as in the case of fig 2.3. In this plot the same features as in the case of synchrotron emission can be noticed, since it is well known that also the IC scattering spectrum in Thomson regime follows $f(\nu) = \nu^{-\frac{\alpha-1}{2}}$ law.

The calculation of electron energy loss rate by IC mechanism is more complicated than in the case of synchrotron emission. When the energy loss of electrons is being calculated, it is necessary to distinguish, whether it is in the Thomson or Klein-Nishina regimes. The Thomson regime can be described in the framework of classical electro-dynamics, while in the case of Klein-Nishina process the quantum treatment is necessary. In general, the energy lose rate is given by,

$$\frac{d\gamma}{dt} = \frac{4 \, c \, \sigma_T}{3 m_e c^2} \, U_0 \gamma^2 F_{KN}, \quad F_{KN} = \frac{1}{U_0} \int_{\varepsilon min}^{\varepsilon max} f_{KN}(\tilde{b}) \, U_\varepsilon d\varepsilon \tag{2.4}$$

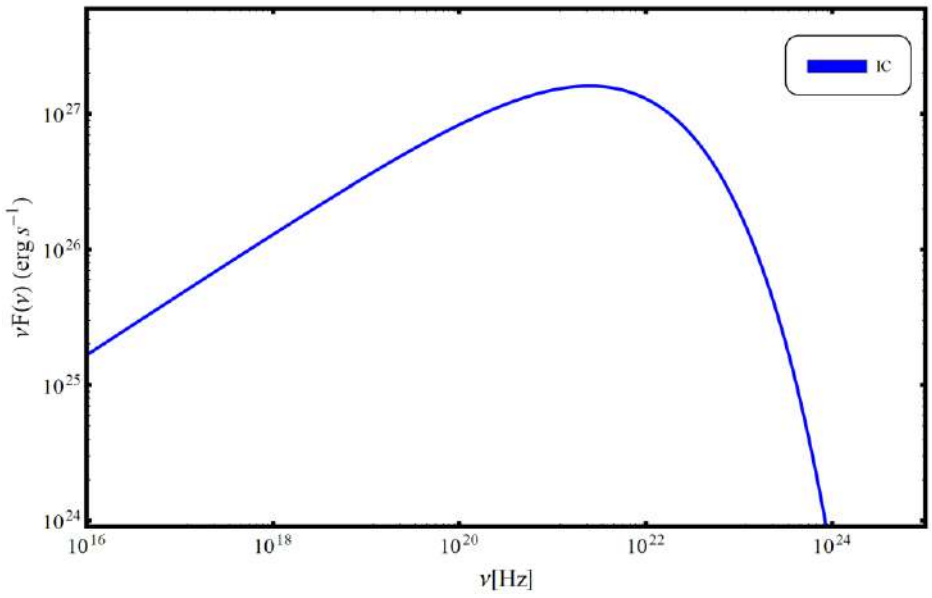

Figure 2.4. Inverse Compton $\nu F(\nu)$ emission spectrum.

where $U_0 = \int_{\varepsilon min}^{\varepsilon max} U_\varepsilon \, d\varepsilon$ is the whole energy density of low energy photon field, U_ε is the energy distribution of photons and $\tilde{b} = 4\gamma\varepsilon/m_e c^2$. In the Thomson regime, when the energy of photons (in the frame of electron) with regard to the electron rest energy is too

small ($\tilde{b} \ll 1$), $f_{KN} = 1$, however, in Klein-Nishina regime, when $\tilde{b} \gg 1$, $f_{KN} \cong \frac{9}{2\tilde{b}^2}(\,ln(\tilde{b}) - 11/6)$. For the cases of $\tilde{b} \ll 10^4$, f_{KN} function can be approximated by the following equation $f_{KN} \cong \frac{1}{(1+\tilde{b})^{1.5}}$, therefore (39):

$$\frac{d\gamma}{dt} = \frac{4}{3}\sigma_T c U_o \gamma^2 \frac{1}{(1+\tilde{b})^{1.5}}. \tag{2.5}$$

Eq. 2.5 implies, that in the case of low energies (Thomson regime) $\frac{d\gamma}{dt} \sim \gamma^2$, and in the case of high energies (Klein-Nishina regime), $\frac{d\gamma}{dt} \sim ln(\gamma)$. In the fig. 2.5 the energy loss of electrons is plotted for the synchrotron (in $1\ \mu G$ magnetic field) and IC (with CMB photons) processes. Since in both cases at low energies the energy loss rate depends on γ^2, then the energy loss rate will be dominated by the IC scattering, because the energy density of $1\ \mu G$ magnetic field is approximately 9 times smaller than the density of CMB photons. When the IC scattering takes place in Klein-Nishina regime, the energy loss rate rapidly decreases.

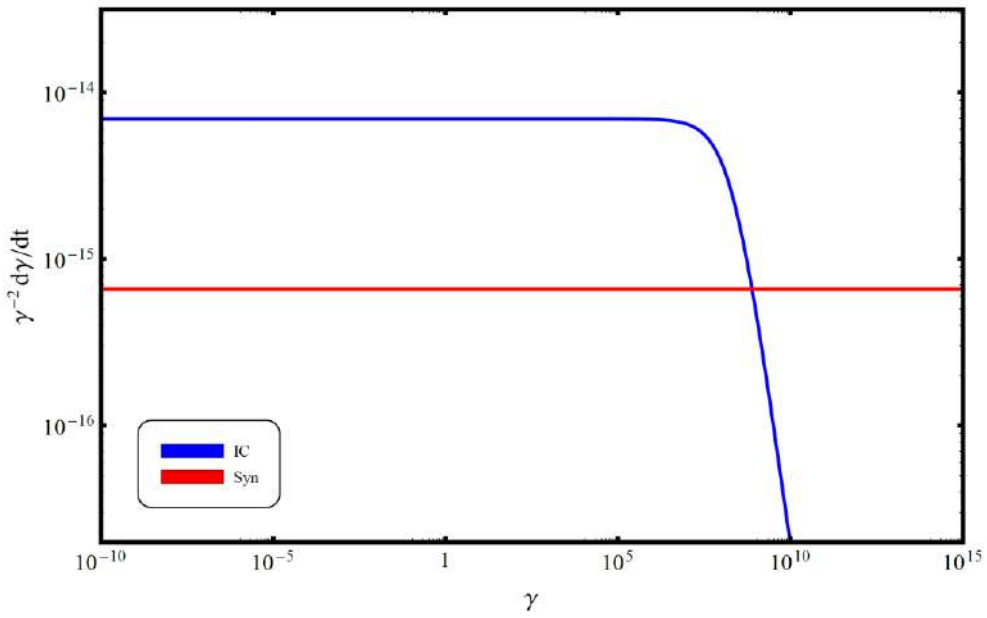

Figure 2.5. Electron energy loss by synchrotron (in $B = 1\ \mu G$ magnetic field) and IC radiations (in CMB photon field).

As one can see from Eq. 2.5, the energy loss rate depends on the density of low energy photons. In general, HE component of blazar emission can be produced by the IC scattering of

- Synchrotron photons
- Accretion disk photons (the photons produced by thermal radiation of accretion disk)
- BLR photons (accretion disk's photons reflected from broad line-region)
- Torus photons (IR photons from dusty torus)

Below, the IC scattering considering all above mentioned photon fields is discussed.

2.2.1. Synchrotron self-Compton radiation

In blazars, under the influence of magnetic field, the relativistic electrons radiate photons (synchrotron radiation), a fraction of which can be scattered on the same electrons through the inverse Compton scattering, because the emitting region is compact. The up scattering of synchrotron photons on the same electron population is called SSC. The electron energy loss in SSC process can be calculated by Eq. 2.5, as well as the emission spectrum of isotropic and homogenous photon and electron distributions can be computed through Eq. 2.3, by substituting $u(\varepsilon) = u_{SSC}(\varepsilon)$ with the following limits of the parameters $q \leq 1$ and $q \geq 1/4\gamma^2$ and $\gamma_{min} = \frac{1}{2}\frac{\varepsilon_s(1+z)}{\delta_D}\left(1 + \sqrt{1 + \frac{1}{\varepsilon\frac{\varepsilon_s(1+z)}{\delta_D}}}\right)$. The photon energy density of synchrotron radiation can be computed by

$$u_{SSC}(\varepsilon) = \frac{2.24\, L_{syn}(\varepsilon)}{4\,\pi\, c\, {R'_b}^2}, \tag{2.6}$$

where $\mathrm{R_b}$ is the radius of emitting region. It is assumed that the emission is produced in a relativistic moving spherical emission region with the volume of $V_b = \frac{4}{3}\pi {R'_b}^3$, which moves with a Γ- bulk Lorentz factor. The radius of an emitting region can be constrained from the temporal variability:

$$R'_b \leq \frac{\delta_D c\, t_v}{(1+z)}, \tag{2.7}$$

where t_v is the observed variability. In the fig. 2.6 the SEDs of synchrotron and SSC emission are plotted, for the parameters of $R'_b = 10^{16}\, cm, \quad B = 100\, mG, \ (\delta_D \approx \Gamma = 10)$; and the electrons have a power-law with exponential cutoff distribution with $\alpha = 2$, $E_{cut} = 0.511\ GeV, E_{min} = 5.11\, MeV, E_{max} = 5.11\, TeV$.

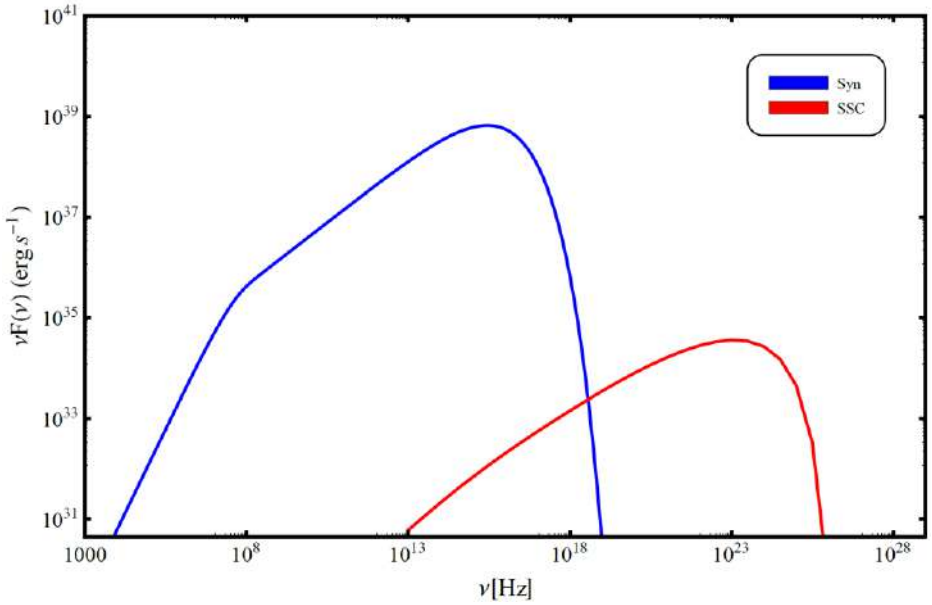

Figure 2.6. SED of synchrotron and SSC radiations.

2.2.2. Inverse Compton scattering of external radiation field

In contrast to SSC process, when the seed photon field is originated within the jet, for the EIC the source of low energy photons is outside the jet. Main photon fields, which can contribute to the radiation in IC process are: photons emitted from the accretion disk directly, and/or when the same photons are reflected by the BLR and/or thermal radiation of dusty torus. Since the seed photons are originated outside the jet, then the photon field and electron population are in different co-moving frames, so in order to calculate the EIC radiation, there are two different approaches:

1. Convert an external photon field to the co-moving frame (jet frame), then calculate the emission (38).
2. Convert the electron distribution to the frame of a photon field and then calculate the emission (40).

In the case of the first approach, the formula 2.3 can be re-written as:

$$L_{EIC} = 3c\sigma_{SB}\varepsilon_S^2\ {\delta_D}^2 \int_0^\infty d\varepsilon' \frac{u'(\varepsilon')}{\varepsilon'^2} \int_{\gamma'_{min}}^\infty d\gamma\ \frac{N'_e(\gamma')}{\gamma'^2} F_c(q, \Gamma_e), \tag{2.8}$$

where the primed quantities refer to the source (initial) frame. In Eq. 2.38 all quantities are transferred into jet's co-moving frame: $u(\varepsilon) = \delta^2\, u'\left(\frac{\varepsilon'}{\delta_D}\right), N(\gamma) = N'_e(\gamma'),\ \varepsilon = \delta_D \varepsilon'$. So when the density of seed photons is known, the spectra of the HE component can be easily computed.

Accretion disk: To calculation the radiation of the accretion disk, we will consider the disc has annulus structure emitting by black body. From the equality of the viscous dissipation rate of Keplerian disk: $D(R) = \frac{3GM\dot{M}}{4\pi R^3}[1 - \left(\frac{R_*}{R}\right)^{1/2}]$ and blackbody flux: $\sigma_{SB}\, T^4$ the temperature of an accretion disk, depending on the radius, can be calculated by

$$T(R) = \frac{3\, R_S L_{disk}}{16\varepsilon\pi\sigma_{SB} R^3}[1 - \left(\frac{3R_S}{R}\right)^{1/2}], \tag{2.9}$$

$$R_S{}^2 \approx \frac{0.14^4 L_{disk}}{\varepsilon\pi T_{disk}^{peak\,4}\sigma_{SB}},$$

$$\sigma_{SB} = 5{,}6704 \times 10^{-5} erg\ cm^{-2} s^{-1} K^{-4},$$

where R_S is Schwarzschild radius, L_{disk} – the maximum luminosity radiated from the disk, T_{disk}^{peak}- the maximum temperature of the disk, σ_{SB}- Stefan-Boltzman constant and ε- a coefficient which indicates the efficiency of the accretion. Typically, $\approx 0.1\,(10\%)$, 10 % of the whole accretion disk radiation. Each ring of the disk will radiate

$$I_\upsilon = B_\upsilon\big(T(R)\big) = \frac{2\upsilon^3\, h}{c^2\left(e^{\frac{h\upsilon}{KT}} - 1\right)}, (erg\ s^{-1} cm^{-2} Hz^{-1} sr^{-1}) \tag{2.10}$$

amount of energy, and by taking into account the Eq. 2.9 we can calculate the disk radiation by integrating the emission of rings within the inner and outer radii ($R_{in} = 3R_s$ and R_{out}) :

$$\upsilon F_\upsilon(\upsilon) = \frac{4\pi h\upsilon^4}{c^2 dL^2}\int_{R_{in}}^{R_{out}} \frac{RdR}{e^{\frac{h\upsilon}{KT(R)}} - 1} \tag{2.11}$$

In the blazar jet, the emitting region is characterized with large bulk Lorentz factor, and the contribution of accretion disk direct radiated photons is negligible because of the de-beaming effects. However, these photons can be reflected/ reproduced from the gas in the BLR clouds, and serve as a strong (beamed) seed photon field for the IC process. BLR is a

region at the distance of $10^{15} - 10^{18}\ cm$ (sub-parsec) from the central clouds, filled with small clouds rotating in high speeds ($1000 - 10000\ km\ s^{-1}$). Doppler broadened emission lines at optical and UV bands are observed from BLR which is believed to be produced in the photoionization gas. Another strong seed photon field can be the dusty torus, which is located far from central source beyond the BLR. Dusty torus is believed to have a toroidal shape, from several hundreds to few thousands kelvin temperature and emits mostly in the IR band.

The radiation luminosity of the external fields can be computed by (38):

$$L_{ext}(\varepsilon) = \frac{15}{\pi^4}\xi_{ext}L_{disk}\frac{(\varepsilon/kT_{ext})^4}{Exp\left[{}^{\varepsilon}/_{kT_{ext}}\right]-1}, \tag{2.12}$$

where ξ_{ext} is the fraction of the reprocessed emission from the accretion disk ($\mathrm{L_{disk}}$), which typically are $\xi_{dust} = 0.3$, $\xi_{BLR} = 0.6$ and T_{ext} is the temperature. The corresponding photon energy densities are (41) (42)

$$u_{ext}(\varepsilon, r) = \frac{L_{ext}(\varepsilon)}{4\,\pi\,c\,{R_{ext}}^2}\frac{1}{1+(r/R_{ext})^{n_{ext}}}, \tag{2.13}$$

where "ext" can be either dusty torus or BLR, and $n_{ext} = 3$ and 4 are used correspondingly for BLR and dusty torus, r - is the distance of the emission region from the central source. The distance of BLR and dusty torus from the central source can be calculated as $R_{BLR} = 10^{17}\left(\frac{L_{disk}}{10^{45}}\right)^{0.5} cm$ (33) and $R_{dust} = 0.4(L_{disk}/10^{45})^{0.5}(1500\ K/T_{dust})^{2.6}\ pc$ (43).

Eq. 2.13 shows that the photon energy density is defined by the position of the emitting region along the jet. In the fig 2.7, the energy densities of CMB, BLR, torus depending on the position of the emitting region are plotted. As one can see, for some combinations of parameters, the external photon fields can dominate over the synchrotron photon field. Moreover, within the BLR, the photon field reflected from BLR clouds are dominating but their density drops out of BLR and IR from dusty torus starts to dominate.

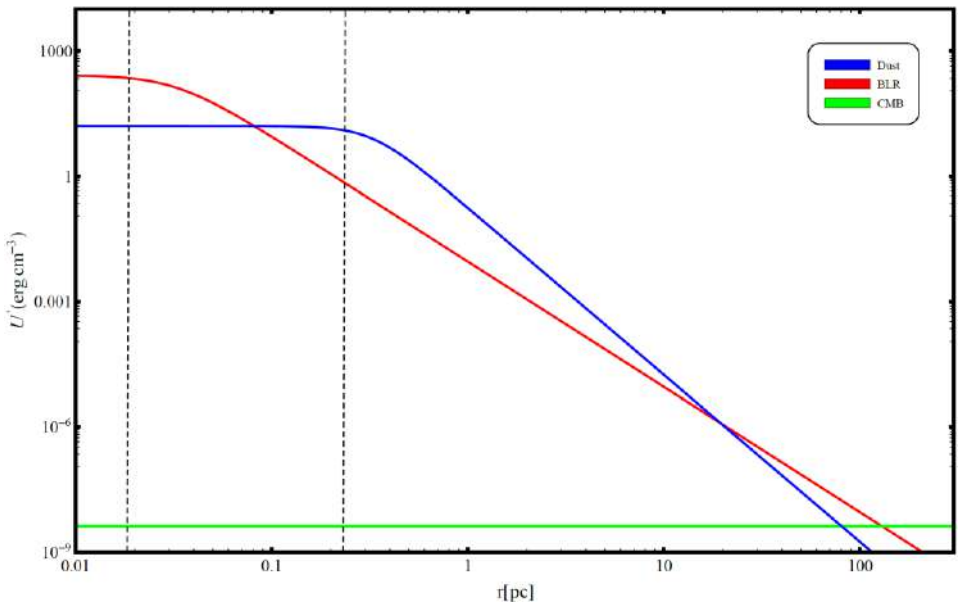

Figure 2.7. Dependence of energy density of different photon fields on the distance of emission region from the central source.

The spectra produced by SSC and EIC are presented in the fig 2.8 (right panel). It is calculated for the electron population having a power-law with exponential cut-off distribution with $\alpha = 2$, $\gamma_{min} = 2$, $\gamma_{max} = 1 \times 10^8$, $\gamma_{cut} = 1 \times 10^5$ and $B = 0.1\ G$, $R = 3 \times 10^{15}\ cm$ (emission region radius), $L_{disk} = 10^{45}\ erg\ s^{-1}$. On the left side, the photon energy density of different fields is depicted assuming the emission region is located within the BLR. The plots show the spectra of HE components when the emission is dominated by various fields.

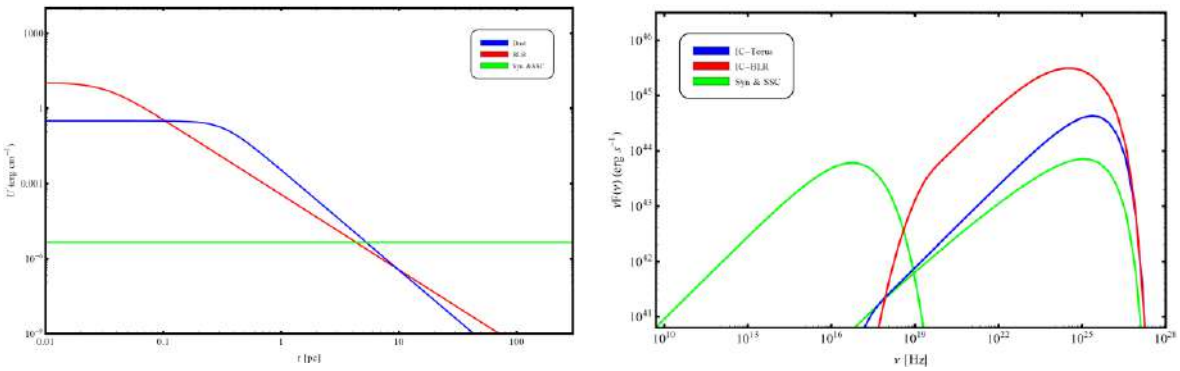

Figure 2.8. Left panel: the energy densities of the photon fields of synchrotron, BLR and dusty torus. Right panel: the corresponding SEDs.

2.3. Particle acceleration mechanisms in jets

The exact mechanism responsible for the acceleration of electrons in blazar jets is still under debate. The non-thermal emission is extended from tens of parsecs up to kpc scales, which primarily indicates the existence of very powerful acceleration mechanisms within the jets. It is believed, that acceleration in blazars is through conversion of magnetic field energy to bulk kinetic energy. The kinetic energy which then transforms to radiation can be driven by the reconnection of magnetic field lines and/or dissipation of shocks (11) (44). The dominance of different acceleration and emission mechanisms will lead to the formation of different emitting particle spectra. For example, one of the most expected mechanisms for electrons acceleration is the diffuse shock acceleration (Fermi acceleration) which predicts a power-law spectrum (45), or when the efficiency of shock acceleration mechanism is considered, this spectrum becomes a power-law with an exponential cutoff distribution (46). When the accelerated particles cool in reasonable timescales, then a broken power-law electron spectrum can be formed (46) (47); and when the main particle acceleration mechanism is stochastic acceleration, then a log-parabolic spectrum will be formed (48). In general the spectra described below can be used in the theoretical modeling:

- power-law

$$N(E_e) = W_e \left(\frac{E_e}{E_0}\right)^{-\alpha}, \tag{2.14}$$

where W_e is the total energy in electrons, E_e and E_0 are the electron energy and normalization, and α is the slope,

- broken power-law

$$N(E_e) = \begin{cases} W_e \left(\frac{E_e}{E_0}\right)^{-\alpha 1} & E_e \leq E_{br} \\ W_e \left(\frac{E_{br}}{E_0}\right)^{\alpha 2-\alpha 1} \left(\frac{E_e}{E_0}\right)^{-\alpha 2} & E_e > E_{br} \end{cases}, \tag{2.15}$$

where E_{br} is the break energy, α_1 and α_2 are the power-law indices before and after the break, respectively,

- exponential cutoff power-law

$$N(E_e) = W_e \left(\frac{E_e}{E_0}\right)^{-\alpha} exp\left(-\left(\frac{E_e}{E_{cutoff}}\right)^{\beta}\right), \tag{2.16}$$

where E_{cutoff} is the cutoff energy and β is the rate of exponential decay, and

- log-parabola

$$N(E_e) = W_e \left(\frac{E_e}{E_0}\right)^{-\alpha-\beta\, log\left(\frac{E_e}{E_0}\right)}, \tag{2.17}$$

where β defines the curvature in the spectra.

Chapter 3

3. Theoretical modeling of blazar SEDs

3.1. Parameter optimization and fitting technique

Statistics is widely used in astrophysics, from classification different sources to analyzing and modeling observed data. In the modeling each theoretical scenario contains several free parameters that cannot be directly derived from the observations. One of the methods to find or at least constrain the free parameters is by fitting the observed spectra with the proposed model. Since different combinations of model free parameters the observed data can be equally good modeled some statistical approach should be applied to differentiate between various models. Among different parameters, the computation of Bayesian factor is the best way to select which model provides better fit to the observed data. This is known as Bayesian model comparison. In the Bayesian formulation, the parameter quantifying the usefulness of the model M for explaining the given dataset is called posterior distribution and is given by

$$p(M|D) = \frac{p(D|M) \times p(M)}{p(D)}, \tag{3.1}$$

where $p(M)$-is the prior model probability, $p(D)$ is a normalization constant which also independent of the model, $p(D|M)$-is the likelihood distribution. In order to compare two M_1 and M_2 models, for the given data, the Bayesian factor, i.e. the ratio of $p(M_1|D)$ and $p(M_2|D)$ needs to compute,

$$B_{2,1} = \frac{p(M_2|D)}{p(M_1|D)} = \frac{p(D|M_2)p(M_2)}{p(D|M_1)p(M_1)}, \tag{3.2}$$

which determines the model, which better explains the given data.

Once a model is specified, the next step is to find the parameter values of a model that best fit the data. In general, fitting of observed data is equivalent to derive free coefficients of variables (parameters) of a function (model) describing the process which is believed to

produce the observed data. Finding parameters of a model, which statistically best describe the observed data, is perhaps one of the most actual problems in the fitting the multiwavelength SEDs of blazars.

There are two main methods of optimizing model free parameters: analytic (e.g. chi-square (χ^2) minimization, maximum log-likelihood estimation, etc.) and numerical (e.g. Newton's, steepest-descent, MCMC methods). Among analytical methods perhaps the simplest method defining the best fit of a function is the chi-square minimization, the idea of which is to minimize the difference between the observed data and prediction by the model:

$$\chi^2 = \sum_{i=1}^{N} \left(\frac{y_i^{OBS} - y_i^{MOD}}{y_i^{MOD}} \right)^2, \tag{3.3}$$

where y_i^{MOD} and y_i^{OBS} are the predicted and observed values, respectively. For a simplest linear function (model) of

$$y^{MOD} = \beta_0 + \beta_1 x, \tag{3.4}$$

through the minimization of

$$J(\beta_0, \beta_1) = \sum_{i=1}^{N} (y_i^{OBS} - y_i^{MOD})^2 = \sum_{i=1}^{N} (y_i^{OBS} - \beta_0 - \beta_1 x_i)^2 \tag{3.5}$$

one can easily derive the statistically best values for β_0 and β_1

$$\begin{cases} \beta_0 = \bar{y} - \beta_1 \bar{x} \\ \beta_1 = \dfrac{\sum_{i=1}^{N} (x_i - \bar{x})(y_i - \bar{y})}{\sum_{i=1}^{N} (x_i - \bar{x})^2} \end{cases} \tag{3.6}$$

where $\bar{y} \equiv \frac{1}{N} \sum_{i=1}^{N} y_i$, $\bar{x} \equiv \frac{1}{N} \sum_{i=1}^{N} x_i$.

Also important to calculate the reduced chi-square (χ_ν^2) as a chi-square per degree of freedom ν, defined as the difference between numbers of data points and fitted parameters. The reduced chi-square value enables to estimate the goodness of match between the data and model in accordance to the data error, e.g., if $\chi_\nu^2 < 1$ there is overfitting and when $\chi_\nu^2 > 1$ there is a poor fitting and a good fit is obtained when $\chi_\nu^2 \approx 1$.

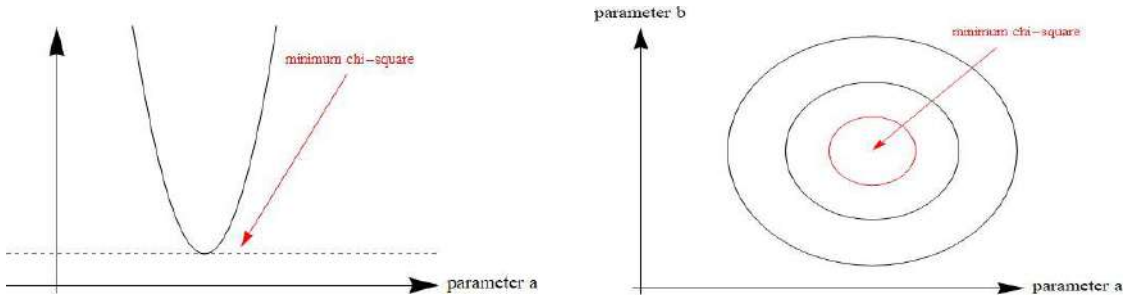

Figure 3.1. Minimization of model / function free parameters through minimum chi-square method. For left: one parameter and right: two parameters space function (49).

Unlike the chi-square method, which is primarily a descriptive tool, the maximum likelihood estimation method is widely accepted method of optimizing model parameters, especially for cases of non-linear modeling. The method allows to estimate free parameters of a given model such to maximize the likelihood that the model can produce the observed data. If individual observations ($x_i{}^{OBS}$) are statistically independent of each other, so the likelihood can be expressed as the product of individual probabilities for a given set of θ,

$$\mathcal{L}(\theta|x^{OBS}) = \prod_{i=1}^{n} p(x_i{}^{OBS}|\theta). \tag{3.7}$$

To maximize the likelihood function, the Eq. 3.7 should be expressed in logarithmic form,

$$ln[\mathcal{L}(\theta|x^{OBS})] = \sum_{i=1}^{n} ln[\, p(x_i{}^{OBS}|\theta)]. \tag{3.8}$$

With the form of Eq. 3.8 the maximization of log-probability function is easy and is just a calculus of the following equation,

$$\frac{\partial ln[\mathcal{L}(\theta|x^{OBS})]}{\partial \theta} = 0 \tag{3.9}$$

Eq. 3.9 gives the global/local maximum or minimum of the function, and as we are interested in the maximum of log-probability function, we will check by,

$$\frac{\partial^2 ln[\mathcal{L}(\theta|x^{OBS})]}{\partial \theta} < 0. \tag{3.10}$$

3.2. Markov Chain Monte Carlo Method

Discussed parameter optimization methods are widely used in astrophysics, however, for models containing many free parameters those analytical methods are not efficient (e.g. expensive to compute) and therefore, much more complex methods should be applied. For high-dimensional problems, the probability distribution function $p(\theta|D)$ of parameters θ explaining the data needs to be numerically evaluated using sampling methods. The most commonly used random sampling methods are MCMC methods (e.g. Metropolis method, Gibbs and slice samplings etc.), which provide an efficient way to sample points from any given distribution which is analogous to evaluating the distribution. MCMC methods comprise a Markov chain process which generates a sequence of states $\{X(t)\}$, such as, the probability of a certain $X(t)$ state depends only upon the previous state of the chain, $X(t-1)$:

$$p(X_5|X_4, X_3, X_2, X_1) = p(X_5|X_4). \tag{3.11}$$

In simple words, if we have n states, the probability of being in each state is equal to $P(X(t))$ and the transition probability from one state to another is $Q(X(t); Y)$, then we can calculate the probability of being at each state after any iterations. For example, if the initial probability (i.e. probability of being at initial state $t = 0$) is $P(X(0))$ and the transition probability is $Q(X(t); Y)$, then after one iteration the probability of being at the state of $t = 1$ will be defined as $P(X(1)) = P(X(0)) \times Q(X(0); X(1))$, similarly after n iterations we will have a probability of $P(X(n)) = P(X(0)) \times Q^n(X(t); Y)$. Apparently, for the first iterations the current state of the chain will be dependent on the starting $P(X(0))$ state, and only after some number of iterations the chain will gradually 'forget' the initial state and start behaving independently. The former phase is called burn-in, and the latter one - posterior (stationary phase). These two main phases of the Markov chain are depicted in the fig. 3.2.

In other words:

Burn in: It is the initial iterations of the chain (states) which are not relevant and not close

to the converging phase. Usually the probabilities of some states are not counted and being removed as they may over-sample regions with low-probabilities.

Posterior: This is the chain after burn in phase, where the walkers (values) being oscillated around a certain (desired) value.

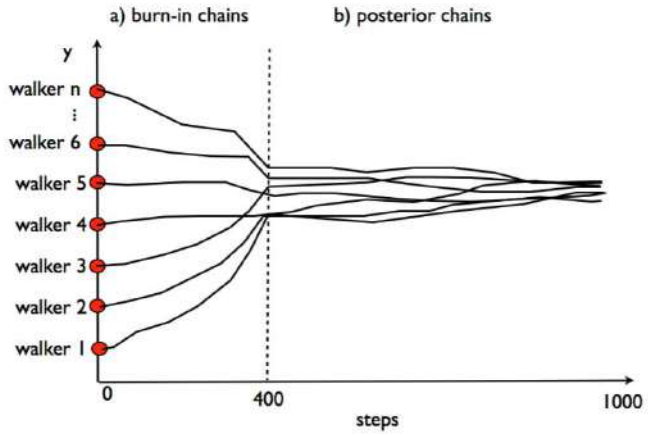

Figure 3.2. Two main phases of Markov chain process: burn-in and posterior (49).

The simplest MCMC algorithm is the "random walk" Metropolis algorithm (50), the efficiency of which depends on a specific task and the dimensionality of the parameter space, as the efficiency decreases while dimensionality increases.

The Metropolis-Hastings Algorithm: In the MCMC methods the Metropolis-Hastings (M-H) is the simplest and most often used algorithm. Assume, we are interested to sample a distribution of $p(X|D)$. To move the sample of parameters from a position $X(t)$ to a new proposal position Y the transition kernel $Q(Y; X(t))$ should be determined. The new move $X(t+1) -> Y$ will be accepted with a probability of

$$min\left(1, \frac{p(Y|D)}{p(X(t)|D)} \frac{Q(X(t);Y)}{Q(Y;X(t))}\right), \tag{3.12}$$

otherwise, the sample of parameters for this step won't change the position, i.e. $X(t+1) -> X(t)$. The M-H algorithm of the MCMC method can be effectively used to solve many problems, however, its efficiency strongly depends on the scaling of the proposal density: when the variance of the proposal is too small, the chain will converge slowly and in the contrary when the variance is too large, the Metropolis algorithm will reject high proportion of its proposed moves (51).

Affine-invariant ensemble sampling algorithm: An affine-invariant ensemble (AIE) sampling algorithm is proposed by (52) and is usually preferred over the standard M-H algorithms, since it is significantly faster especially on highly skewed distributions. In this algorithm, one step of the Markov chain, $X(t) -> X(t+1)$, is considered to consist of a cycle through L walkers in the ensemble (52). For a single position move this is expressed in pseudo-code as,

for k = 1,…,L

$X_k(t) \rightarrow X_k(t+1)$

Each walker X_k is updated using the current position of one (randomly chosen) complementary walker $X_j \in X_{[k]}$, where

$$X_{[k]}(t) = \{X_1(t+1), X_2(t+1), \dots, X_{k-1}(t+1), X_{k+1}(t), \dots, X_L(t)\}. \tag{3.13}$$

The new position through "stretch move" is proposed by (see fig. 3.3):

$$X_k(t) \rightarrow Y = X_j + Z\big(X_k(t) - X_j\big), \tag{3.14}$$

where Z is a scaling variable randomly drawn from a distribution $g(Z)$ (53). The move is symmetric, i.e. $(Pr[X_k(t) \rightarrow Y] = Pr[Y \rightarrow X_k(t)])$, when $g\left(\frac{1}{z}\right) = z\, g(z)$ (53). Under this condition, the move $X_k(t+1) = Y$ will be accepted with the probability of

$$q = min\left(1, Z^{N-1}\frac{p(Y)}{p\big(X_k(t)\big)}\right), \tag{3.15}$$

where N is the dimension of the parameter space (52), otherwise set $X_k(t+1) = X_k(t)$. Note, that the proposal value Y lies on the ray

$$y - X_j = \lambda\big(X_k(t) - X_j\big) \quad \lambda > 0, \tag{3.16}$$

where y belongs to the real coordinate space of N dimensions (52).

In summary, to update $X(t)$ a "stretch move" approach for per walker is applied. For each walker "k" a randomly chosen $X_j \in X_{[k]}$ is used, then $Y = X_j + Z\big(X_k(t) - X_j\big)$ is generated, where all of Z-s are chosen independently, consequently, the stretch move of $X_k(t) \rightarrow X_k(t+1) = Y$ is accepted with the probability of q (in Eq. 3.15), otherwise being rejected and set $X_k(t+1) = X_k(t)$.

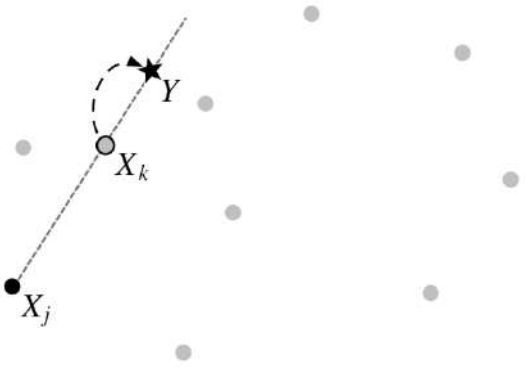

Figure 2.3. Shift of X_k position. The gray dots represent $X_{[k]}$ walkers not participating in this move. The Y proposal is generated by stretching along the straight line connecting X_k to X_j (52).

In (54) the authors parallelized the "stretch move" algorithm which allows to update each walker simultaneously based on the condition of the ensemble, instead of advancing the walkers in series. To implement this, in (54) they split the full ensemble into two subsets $S_1 = \left\{X_k;\ k = 1, \dots, \frac{L}{2}\right\}$ and $S_2 = \{X_k; k = \frac{L}{2} + 1, \dots, L\}$ and updated S_1 by means of "stretch move" technique based on the current positions of the walkers in S_2 set , then vice versa. The MCMC algorithm, proposed in (52) and briefly discussed above, was adopted in emcee package (54) which has wide applicability in various astrophysical tasks, ranging from Hubble constant measurement (55) through estimation of parameters of neutron stars (56) and late-type M dwarf (57). For example, in (57), the emcee package is applied to estimate the values of unobservable star parameters such as the mass and age (for more applications of *emcee* see (58)). The advantages of the *emcee* package are applied in the modeling of the SEDs of blazars.

3.3. Application

In order to optimize the free parameters, when multiwavelength SEDs of blazars are modeled, during the PhD I developed a python code. It is based on the *Naima* package (59), which is based on the emcee package, enables to constrain a model's free parameters by performing MCMC fitting. The MCMC approach, which is based on the Bayesian statistics, is superior to the grid approach with a more efficient sampling of the parameter space of interest, especially for high dimensions (60). The algorithm behind

the code is the affine-invariant ensemble sampling algorithm for MCMC method (discussed in section 3.2) proposed by Goodman & Weare (52), which has several advantages over traditional MCMC sampling methods (e.g. the Metropolis-Hastings algorithm) and excellent performance as measured by the autocorrelation time (54). The code derives the best-fit model and uncertainty distributions of spectral model parameters through MCMC sampling of their likelihood distributions. The measurements and uncertainties in the observed data are assumed to be correct, Gaussian, and independent (59). Under this assumption, the likelihood of the observed data given the spectral model $S(\vec{p}; E)$, for a parameter vector $\vec{p}$, is

$$\mathcal{L} = \prod_{i=1}^{N} \frac{1}{\sqrt{2\pi\sigma_i^2}} exp\left(-\frac{(S(\vec{p}; E_i) - F_i)^2}{2\sigma_i^2}\right), \tag{3.17}$$

where (F_i, σ_i) are the flux measurement and uncertainty at E_i over N spectral measurements. The corresponding log-likelihood will be:

$$ln\,\mathcal{L} = K - \sum_{i=1}^{N} \frac{(S(\vec{p}; E_i) - F_i)^2}{2\sigma_i^2}. \tag{3.18}$$

Given that the MCMC procedure will sample the areas of the distribution with maximum value of the objective function, it is useful to define the objective function as the log-likelihood disregarding the constant factor:

$$ln\,\mathcal{L} \propto \sum_{i=1}^{N} \frac{(S(\vec{p}; E_i) - F_i)^2}{2\sigma_i^2}. \tag{3.19}$$

The $ln\,\mathcal{L}$ function, in this assumption, can be related to the χ^2 parameter as $\chi^2 = -2ln\,\mathcal{L}$, so that maximization of the log-likelihood is equivalent to the minimization of χ^2 (59). In addition to the likelihood from the data points, a prior likelihood for all free parameters should be considered. This prior likelihood should be constrained using our knowledge of parameters, for example if it can be inferred from observed parameters or from previous modeling. The combination of the prior and data likelihood functions are used to initiate MCMC run to find parameters best describing the data.

The prepared package consists of three major sub-packages: *radiative models*- where

all cross-sections of electron interaction are defined (see section 2.1-2.2), *electron spectral models*- where all possible electron spectra expected from their acceleration and cooling are defined (see section 2.3), and *optimization* sub-package- that optimize the model free parameters. Each of them should be properly defined before running the program.

Before starting the fit, the initial values for all considered parameters should be provided together with the parameters known from the observations (e.g., size of the emission region, Doppler factor etc.). Also, the parameters for the external photon field(s) should be provided and defined which fields should be considered for the IC calculations. In order to optimize the step for providing initial parameters for the electron energy distribution (EED) and magnetic field, after lunching the program an interactive window will appear (see in fig 3.4), which allows to change the parameters manually in order to reach reasonable fit to data (visual). Especially in the cases of complex models (e.g. synchrotron + SSC + EIC) visual fitting the curve to the data will allow the program to escape of getting stuck in a local maximum. Also, this optimization can be done with the defined Nelder-Mead algorithm. Nelder-Mead algorithm is an effective and computationally compact way to search the maximum likelihood of parameter vector and/or a local minimum/maximum of a multivariable function (see more in (61)).

The programs allow to the users to perform the fitting in fast (*nwalkers* = 32, *nburn* = 10, *nrun* = 10, *thread* = 4) and slow (*nwalkers* = 64, *nburn* = 100, *nrun* = 100, *thread* = 4) modes, which use different division of the provided range of parameters. The *nwalkers* parameter is defined in Goodman & Weare (52), which specifies how many walkers will be used in the sampling procedure; *nburn* specifies how many steps should be run as burn-in and after *nburn* steps the sampler is reset and the chain history discarded; the *nrun* specifies how many steps to run after the burn-in and save these samples in the sampler object, and the *thread* is the number of threads to use for sampling (59). The user can choose which mode is better, depending on the number of data points and free parameters.

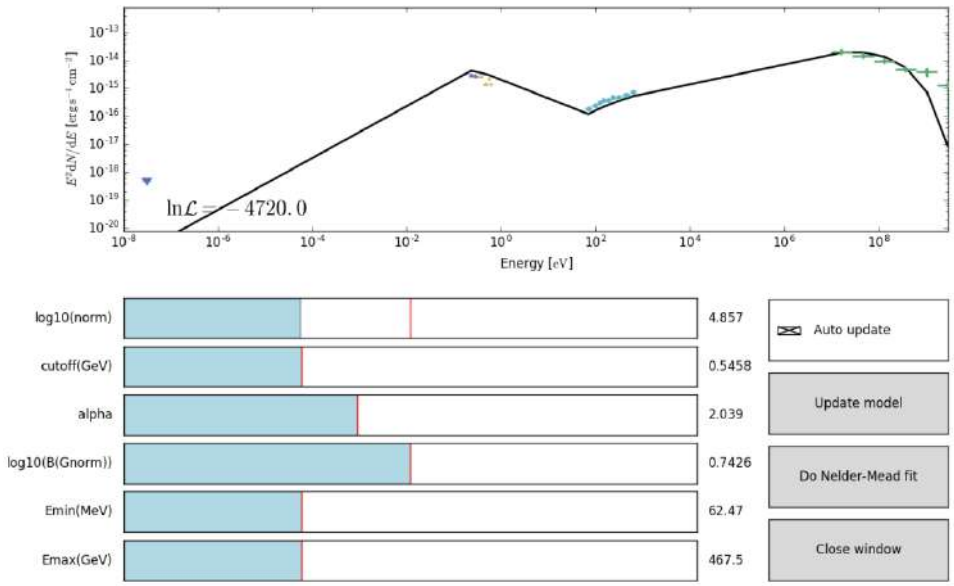

Figure 3.4. Interactive window before fitting, which enables to set the best initial parameters.

Sometimes the emission from distant blazars can be absorbed, when the produced photons interact with EBL photons and in the modeling this absorption should be taken into account. The code includes several models for EBL absorption (e.g., (62), (63) , etc.) which can be defined by the user. As a result, the code creates several files including a table of derived values with uncertainties of parameters, distribution plot of each parameter, all curves (including the best) of attempted fits, etc.

In order to show practical application of the code the modeling of SEDs of two well-known blazars PKS 0537-441 and Mkn 501 is illustrated. These two sources are selected from both types of blazars, the first one is a BL Lac, and the second one is a FSRQ to demonstrate the data fitting using both SSC and EIC models.

Mkn 501 at a redshift $z = 0.034$ is among the most studied BL Lacs in the γ-ray band (64). For the modeling, the simultaneous data observed between 2009 March 15 (MJD 54905) to 2009 August 1 (MJD 55044) are used. The emission is assumed to be produced from a region (“blob”) with a size of $R = 1.3 \times 10^{17}\ cm$ and a Doppler factor of $\delta = 12$ (64).

PKS 0537-441 is a bright FSRQ blazar at the distance of $z = 0.896$ (65). For modeling the averaged spectrum observed during 2008 August 4–2010 February 4 (MJD

546 82–552 31) is used. The blob with a size of $R = 1.6 \times 10^{17}\ cm$ (65) is assumed to move with a bulk Lorentz factor of $\Gamma_{bulk} = \delta = 50$. It is assumed, that the emitting region is outside the BLR and the torus photons are dominating. The torus is assumed to have a blackbody spectrum with a luminosity of $L_{dust} = 3.3 \times 10^{42}\ erg\ s^{-1}$ and a temperature of $T_{dust} = 3 \times 10^{2}\ K$ (65) and fills a volume that for simplicity is approximated as a spherical shell with a radius of $R_{dust} = 0.4(L_{disk}/10^{45})^{0.5}(1500\ K/T_{dust})^{2.6}\ pc$ (43).

The broadband SEDs of Mkn 501 and PKS 0537-441 are shown in fig. 3.5, where the data are from (64) and (65), respectively. The data are modeled with slow-mode, because of the large number of data points, in the framework of one-zone leptonic model involving synchrotron, SSC and EIC processes. In the modeling of the SEDs of Mkn 501 and PKS 0537-441, the synchrotron/SSC and synchrotron/EIC scenarios have been correspondingly considered.

The electron energy distribution responsible for the nonthermal emission is assumed to be broken power-law, which is naturally formed from the cooling of relativistic electrons (46) (47). The prior likelihood, our prior knowledge of the probability distribution of a given model parameter, and the data likelihood functions are passed on to the emcee sampler (54) function for an affine-invariant MCMC run. There are seven model free parameters (e.g. the magnetic field, electron spectral indices etc.) and for each of them physically reasonable ranges are provided: $1 \leq (\alpha_{1,2}) \leq 10$, $0.511\ MeV \leq E_{(br,min,max)} \leq 1\ TeV$, and W_e and B are defined as positive parameters. Using MCMC fitting, the predicted emission spectra for each combination of the seven parameters are calculated and combined with the data, and then the maximum log-likelihoods are obtained. The modeling results of SEDs are shown in fig. 3.5 and the estimated parameters are in Table 3.1. In addition, the posterior distributions of spectral model parameters are obtained, and two of them with the posterior distribution and parameter values with respect to the step number of the chains are depicted in fig. 3.6. Since a strong EBL absorption is expected for the distance of PKS 0537-441 ($z = 0.896$), in the SED modeling the EBL absorption was taken into account using the model

of *Franceschini et al. (2008)* (62).

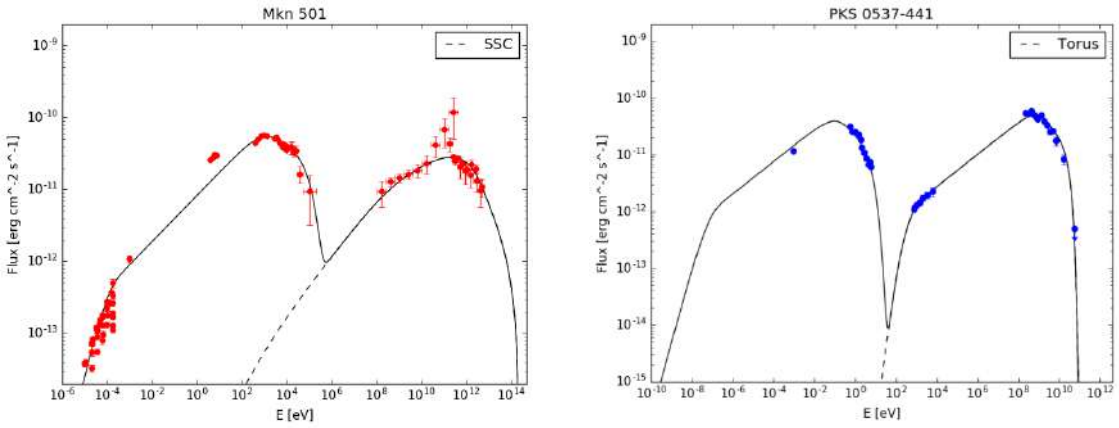

Figure 3.5: Modeling the broadband SEDs of Mkn 501 and PKS 0537. Dotted lines show the high-energy models. The model parameters are presented in Table 3.1.

Table 3.1. Model parameters.

	Parameter	Mkn 501	PKS 0537-441
Doppler factor	δ	12	50
Total electron energy	$W_e \times 10^{50}\ erg$	0.11	2.72
Low-energy electron spectral index	α_1	$2.36^{+0.08}_{-0.05}$	$2.429^{+0.005}_{-0.010}$
High-energy electron spectral index	α_2	3.39 ± 0.01	3.68 ± 0.03
Minimum electron energy	$E_{min}(MeV)$	$126.41^{+19.60}_{-11.20}$	$0.73^{+0.01}_{-0.09}$
Break electron energy	$E_{br}(GeV)$	$431.91^{+30.29}_{-59.43}$	$1.00^{+0.04}_{-0.02}$
Maximum electron energy	$E_{max}(TeV)$	$3.80^{+0.39}_{-0.73}$	$6.05^{+0.03}_{-0.05}$
Magnetic field	$B[mG]$	$7.95^{+3.77}_{-1.49}$	$67.47^{+0.66}_{-0.52}$
Jet power in magnetic field	$L_B \times 10^{42} erg\ s^{-1}$	0.58	1092.62
Jet power in electrons	$L_e \times 10^{45} erg\ s^{-1}$	0.28	95.69

The application is further used to investigate the physical processes taking place in four different FSRQs which are detected in VHE γ-ray band (66). The majority of the blazars detected in the VHE γ-ray band are high-frequency-peaked BL Lacs for which the synchrotron bump is in the UV/X-ray bands. In addition to BL Lacs, there are also 7 FSRQs, S3 0218+35, TON 0599, PKS 0736+017, PKS 1222+216, 3C 279, PKS 1441+25 and PKS 1510-089, detected in the VHE γ-ray band which is rather surprising, since the BLR

structure of these objects, which is rich in optical-UV photons, makes these environments strongly opaque to VHE γ-rays.

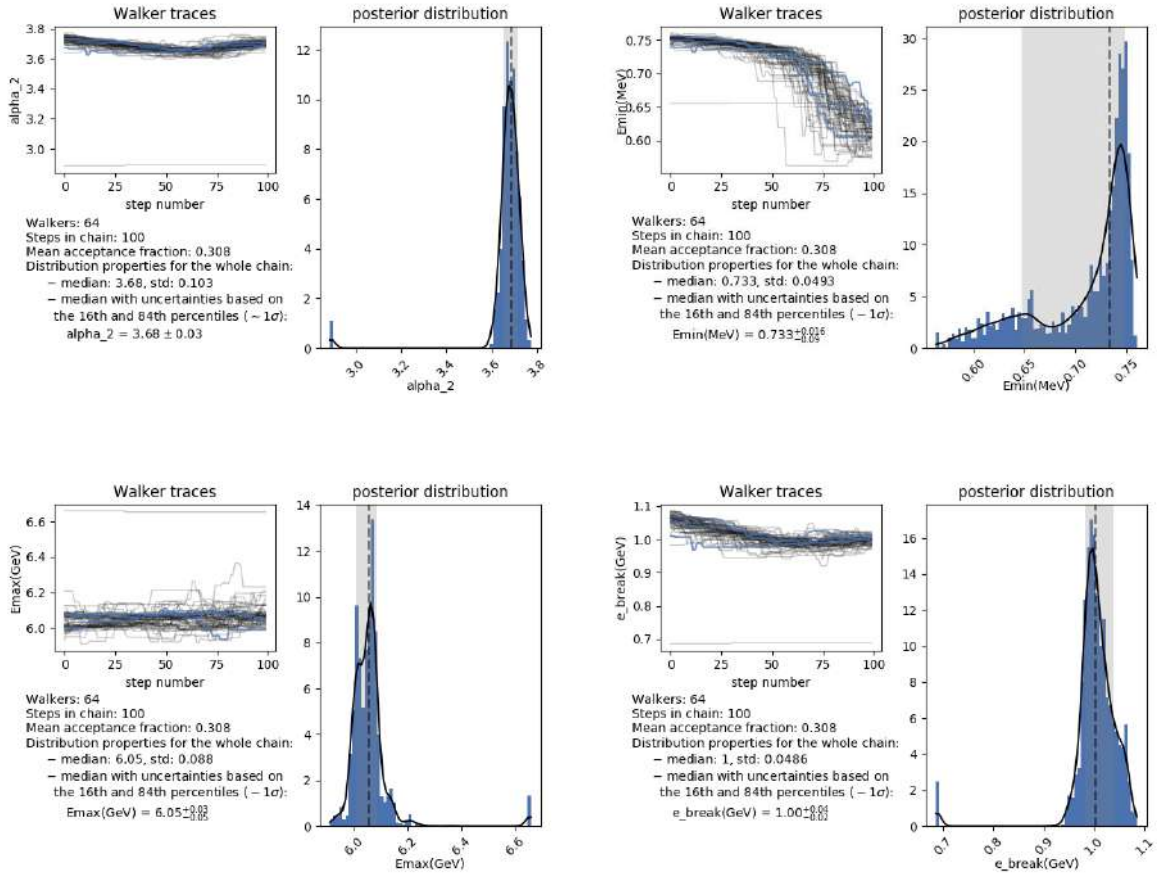

Figure 3.6. The posterior distributions for α_2, E_{min}, E_{max}, E_{br} and parameters of PKS 0537-441 fitting, assessed through MCMC sampling, with several statistical and computational parameters are plotted.

In this section, we investigate the emission from 3 FSRQs, PKS 1510-089, PKS 1222+216 and 3C 279, which are alternatingly in the flaring or quiescent states.

PKS 1510-089 at a redshift $z = 0.361$ is a γ-ray bright quasar (67), (68). It is monitored in many energy bands, showing several bright periods with most rapid changes observed in the HE γ-ray band (the flux doubling timescale is as short as ~ 20 $minutes$ (18)). From many flares we selected these observed in March 2009 (69), in February-April 2012 (68), on 18 May 2015 (2015A) and on 22 May 2015 (2015B) (70) which demonstrated interesting modification of the flux and photon index. The data in the quiescent state are time-averaged spectra from ASI science data center (71).

PKS 1222+216 has been active in the MeV/GeV band since September 2009 followed by brightening also in other observable wavebands. The source underwent two major flares with the maximum of $F_{\gamma,>100\,MeV} = 10^{-5}\,photon\,cm^{-2}s^{-1}$ in April and June 2010 (72). During the second flare the MAGIC telescope also observed increased γ-ray emission with a flux doubling timescale of $\sim 10\,min$ (17). The data for Flare 1 are from (73), while for the quiescent state (collected from August 2008 to 12 September 2009) and Flare 2 are from (74).

3C 279 is probably one of the best and most studied blazar in the γ-ray sky. The emission from this blazar is variable in almost all observed frequencies. Sometimes the flares are simultaneous while in general different time lags are observed. In (42), analyzing multiwavelength light curves, they found at least 5 periods between 2008 and 2010 when the source was in the flaring state. Each of these flares is different (by means of the flux changes observed in different bands) and needs to be studied individually. For the current study we picked the Flare B (19 November- 9 December 2008) and G (30 July - 2 August 2009) from (42). During the first flare, the flux in the optical and γ-ray bands increased simultaneously, while the X-ray flux was relatively constant. On the contrary, during the second flare, the increase was observed in all bands (optical, X-ray and γ-ray). For the quiescent state the data collected from April to July 2010 are used (75).

3.4. The Origin of Emission in the Quiescent and Flaring States: PKS 1510-089, PKS 1222+216 and 3C 279

In fig. 3.7 the multiwavelength SEDs of PKS 1510-089, PKS 1222+216 and 3C 279 are shown in the quiescent and flaring states. The observed fast variability indicates that their emission regions are compact but their localization is an open problem. Along the jet, the emission can be produced in different zones, and depending on the distance from the central black hole different components can contribute to the observed emission (41).

The strong amplification of the emission from blazars can be explained by means of introducing changes in the emission region parameters, e.g., in the magnetic field, emitting region size, bulk Lorentz factor and others, and/or particle energy distribution. Usually, the

change in one or two parameters is enough to explain the flares. An interesting study of the flaring activity in FSRQs as a result of changes in different parameters has been performed

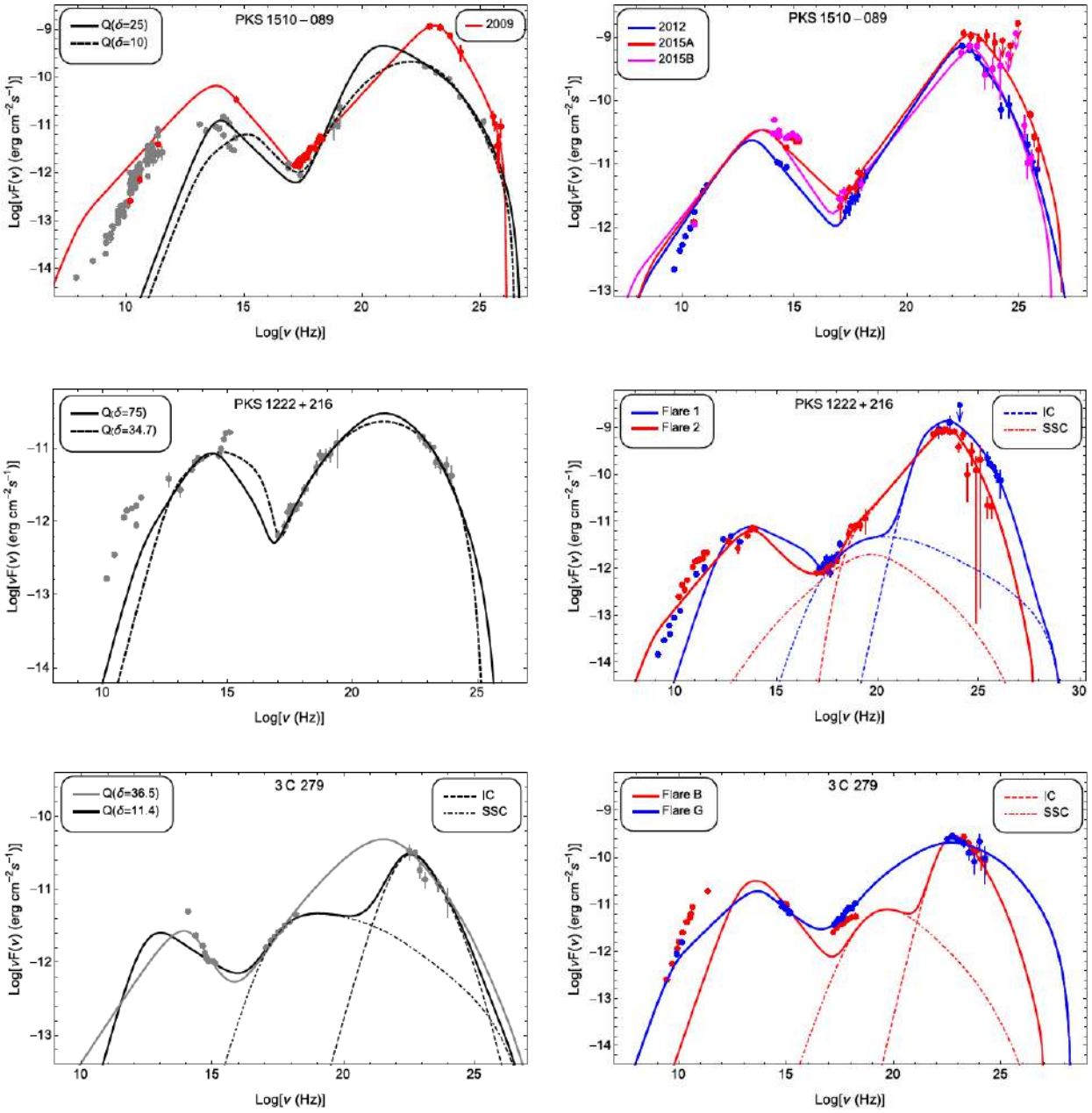

Figure 3.7. The broadband SEDs of blazars in the flaring and quiescent states. When EBL absorption is significant, the model and data are corrected for EBL absorption

in (76). During the flaring periods considered here both the low-energy and HE components are increased but the modification of HE emission component is more drastic. The increase of the second component is most likely due to moving of the emitting region outside the BLR. In principle, there are two possibilities: *i)* either the emitting region moves faster due to increasing bulk Lorentz factor and leaves the BLR or *ii)* the bulk Lorentz

factor is unchanged and only the emitting region is moving beyond the BLR. In the first case, since the external photon density in the commoving frame of the jet depends on the Doppler boosting factor, a strong increase in the Compton dominance will be observed. We note that the change of the bulk Lorentz factor will also affect the low-energy component. In the second case, the flaring activity is due to the change of the location of the emitting region and due to the magnetic field amplification. Accordingly, in the modeling of broadband SEDs we discuss two possibilities. First, we assume that δ has increased from the quiescent to the flaring periods (the values are given in Table 3.2), and then we assume that it was constant.

3.4.1. Emission processes

We modeled the SEDs during high and quiescent states in the framework of single-zone leptonic models that include the synchrotron, SSC, and EIC processes. The emission region (the "blob"), assumed to be a sphere with a radius of R which is moving with a bulk Lorentz factor of Γ, carries a magnetic field with an intensity of B and a population of relativistic electrons. The blob velocity makes a small angle with respect to the line of sight, so the emission is amplified by a relativistic Doppler factor of δ. The energy spectrum of the population of electrons in the jet frame, which is responsible for the non-thermal emission, is assumed to have a broken power-law shape: $N'_e(E'_e) = N'_0(\frac{E'_e}{m_e c^2})^{-\alpha_1}$ when $E'_{min} \leq E'_e \leq E'_{br}$ and $N'_e(E'_e) = N'_0(\frac{E'_{br}}{m_e c^2})^{\alpha_2-\alpha_1}(\frac{E'_e}{m_e c^2})^{-\alpha_2}$ when $E'_{br} \leq E'_e \leq E'_{max}$ where α_1 and α_2 are the low and high indexes of electrons correspondingly below and above the break energy E'_{br} and E'_{min} and E'_{max} are the minimum and maximum energies of electrons in the jet frame, respectively. The low-energy (from radio to optical/X-ray) emission is due to the synchrotron emission of electrons in a homogeneous and randomly oriented magnetic field. For the quiescent state we assume the energy dissipation occurs close to the central source region and it is explained as an IC scattering of synchrotron photons (SSC). Instead, the high state emission is dominated by that from a region well outside the BLR in order to avoid the strong absorption of VHE photons. In this case the dominant external photon field is the IR radiation from the dusty torus which, as we assume, has a blackbody spectrum

with a luminosity of $L_{IR} = \eta\, L_{disk}$ ($\delta = 0.6$, (26)) and a temperature of $\mathrm{T} = 1200\ \mathrm{K}$ and fills a volume that for simplicity is approximated as a spherical shell, the radius of which is defined from the relation $R_{IR} = 3.54 \times 10^{18} (L_{disk}/10^{45})^{0.5}\ cm$ (43).

For the emitting region size the following parameters were considered: for PKS 1510-089: $R = 4 \times 10^{14}\ cm$ and $R = 10^{15} cm$ for the quiescent and flaring states respectively; for PKS 1222+216: $R = 4.6 \times 10^{14}\ cm$ and $R = 10^{15} cm$ for the quiescent and flaring states respectively; for 3C 279: $R = 3.4 \times 10^{15} cm$, $R = 1.1 \times 10^{16}\ cm$ and $R = 1.4 \times 10^{18}\ cm$ for the quiescent, periods B and G respectively.

In order to constrain the model free parameters, the code described in Chapter 3.3 is used. In the parameter sampling, the following expected ranges are considered: $1.5 \leq (\alpha_{1,2}) \leq 10$, $0.511\ MeV \leq E'_{min,br,max} \leq 1\ TeV$ and N_0 and B are defined as positive parameters. The synchrotron emission is calculated using the parameterization of the emissivity function of synchrotron radiation in random magnetic fields presented in (77) while the IC emission is computed based on the monochromatic differential cross section of (78).

3.4.2. Results

The results of the SEDs modeling are shown in fig. 3.7 with the corresponding parameters in Table 3.2 where along with the best fit values also the uncertainties in the parameter estimation are provided.

Table 3.2. The parameters derived from the modeling of the SEDs of blazars in the quiescent and flaring states.

	α_1	α_2	$\mathrm{E}'_{\mathrm{br}}(GeV)$	$B(G)$	$\mathrm{L_B}/10^{41}$ $(erg\ s^{-1})$	$\mathrm{L_e}/10^{44}$ $(erg\ s^{-1})$
			PKS 1510-089			
Q $(\boldsymbol{\delta = 10})$	$2.13^{+0.03}_{-0.06}$	$4.05^{+0.16}_{-0.18}$	$1.39^{+0.20}_{-0.28}$	$5.23^{+0.46}_{-0.60}$	16.4	1.5
Q $(\boldsymbol{\delta = 25})$	$1.83^{+0.05}_{-0.04}$	$3.96^{+0.02}_{-0.02}$	$0.58^{+0.02}_{-0.02}$	$0.37^{+0.01}_{-0.01}$	3.2	22.0

Table 3.2. (Continued)

2009 $(\delta = 25)$	$1.91^{+0.01}_{-0.01}$	$4.13^{+0.20}_{-0.20}$	$0.63^{+0.01}_{-0.01}$	$0.45^{+0.01}_{-0.01}$	4.9	537.0
2012 $(\delta = 25)$	$1.93^{+0.03}_{-0.03}$	$3.84^{+0.03}_{-0.02}$	$0.30^{+0.01}_{-0.01}$	$0.36^{+0.002}_{-0.002}$	3.0	604.4
2015A $(\delta = 25)$	$2.02^{+0.10}_{-0.06}$	$3.68^{+0.08}_{-0.06}$	$0.46^{+0.08}_{-0.08}$	$0.34^{+0.01}_{-0.02}$	2.7	759.0
2015B $(\delta = 25)$	$2.11^{+0.04}_{-0.04}$	$4.04^{+0.12}_{-0.09}$	$0.52^{+0.07}_{-0.04}$	$0.46^{+0.02}_{-0.02}$	5.0	598.2
			PKS 1222+216			
Q $(\delta = 34.7)$	$2.26^{+0.09}_{-0.07}$	$3.24^{+0.04}_{-0.04}$	$0.50^{+0.07}_{-0.04}$	$2.26^{+0.03}_{-0.03}$	49.8	3.2
Q $(\delta = 75)$	$1.86^{+0.02}_{-0.01}$	$3.93^{+0.06}_{-0.04}$	$1.07^{+0.04}_{-0.02}$	$0.16^{+0.003}_{-0.003}$	5.5	30.3
Flare1 $(\delta = 75)$	$2.24^{+0.42}_{-0.32}$	$3.41^{+0.16}_{-0.14}$	$0.31^{+0.07}_{-0.07}$	$0.42^{+0.03}_{-0.03}$	36.8	10.5
Flare2 $(\delta = 75)$	$1.96^{+0.005}_{-0.004}$	$3.91^{+0.01}_{-0.01}$	$0.33^{+0.005}_{-0.005}$	$0.47^{+0.002}_{-0.002}$	47.2	15.2
			3C 279			
Q $(\delta = 11.4)$	$1.98^{+0.09}_{-0.13}$	$3.47^{+0.08}_{-0.03}$	$0.14^{+0.01}_{-0.01}$	$2.07^{+0.03}_{-0.06}$	242.0	3.7
Q $(\delta = 36.5)$	$1.91^{+0.01}_{-0.01}$	$4.28^{+0.04}_{-0.07}$	$2.86^{+0.07}_{-0.14}$	$0.02^{+0.0009}_{-0.0003}$	2.3	285.7
Flare B $(\delta = 36.5)$	$2.60^{+0.31}_{-0.54}$	$4.17^{+0.43}_{-0.38}$	$0.48^{+0.11}_{-0.09}$	$0.56^{+0.06}_{-0.06}$	1872.7	9.3
Flare G $(\delta = 36.5)$	$2.10^{+0.05}_{-0.05}$	$3.74^{+0.03}_{-0.03}$	$11.72^{+1.01}_{-0.96}$	$(5.60 \pm 0.30) \times 10^{-4}$	32.0	4801.6

PKS 1510-089: The multiwavelength SED in the quiescent state has been modeled using one-zone synchrotron/SSC emission model, assuming that the jet Doppler boosting factor is $\delta = 10$ which then increases to $\delta = 25$ (upper left panel in fig. 3.7). When $\delta = 10$, the power-law indexes and break energy of underlying electron distribution are $\alpha_1 = 2.13 \pm 0.05$, $\alpha_2 = 4.05 \pm 0.17$ and $E'_{br} = 1.39 \pm 0.24\, GeV$. The magnetic field is $B = 5.23 \pm 0.53\, G$ and its luminosity corresponds to the small fraction of the total jet luminosity $L_{jet} = L_B +$

$L_e = 1.5 \times 10^{44}\, erg\, s^{-1}$. When δ increases to $\delta = 25$, $\alpha_1 = 1.83 \pm 0.05$ and $\alpha_2 = 3.96 \pm 0.02$ with lower $E'_{br} = 0.58 \pm 0.02\, GeV$ and $B = 0.37 \pm 0.01\, G$ are obtained. These decreases are due to the increase of δ (accordingly also the emitting region size) and are necessary to not overproduce the low energy component by the synchrotron emission. The required total jet luminosity increases to $L_{jet} = 2.2 \times 10^{45}\, erg\, s^{-1}$ and again mostly dominated by the non-thermal energy of electrons.

Since during the flaring periods also VHE γ-ray emission above ≥ 100 GeV has been detected, the emitting region should be well outside the BLR, in order to avoid the strong absorption of these photons. In this case the dominant external photon field is the IR radiation from the dusty torus, and the HE emission is modeled assuming that it is entirely due to the IC scattering of external photons. When the SEDs are modeled (fig. 3.7 upper right panel), the electron distribution as well as the magnetic field should vary. The parameter ranges which can reproduce the observed data are: power-law indexes of electrons $\alpha_1 = (1.91 - 2.11)$ and $\alpha_2 = (3.68 - 4.13)$, the break energy $E'_{br} = (0.30 - 0.63)\, GeV$ and the magnetic field $B = (0.34 - 0.46)\, G$. Noticeable is the change in the total jet power; $L_{jet} = (5.4 - 7.6) \times 10^{46}\, erg\, s^{-1}$ is needed to explain the increase of the flux. Also, in order to explain large Compton dominance, the jet should be strongly particle-energy-dominant with $U_e/U_B \geq 10^5$.

PKS 1222+216: The data from the quiescent state allow to constrain both the low- (Swift XRT/BAT) and high- (*Fermi* LAT) energy power-law indexes of the underlying electron distribution (middle left panel in fig. 3.7). The synchrotron/SSC model can explain the observed data in the quiescent state when $\delta = 34.7$, if the power-law index changes from $\alpha_1 = 2.26 \pm 0.08$ to $\alpha_2 = 3.24 \pm 0.04$ at the break energy of $E'_{br} = 0.50 \pm 0.06\, GeV$. When $\delta = 75$, the corresponding parameters are $\alpha_1 = 1.86 \pm 0.02$, $\alpha_2 = 3.93 \pm 0.05$ and $E'_{br} = 1.07 \pm 0.03\, GeV$. This change of parameters is related with the changes in the emitting region size and magnetic field, e.g., α_1 is defined by the HE component (SSC) which strongly depends on the magnetic field which changes from $B = (2.26 \pm 0.03)\, G$ to $B = (0.16 \pm 0.003)\, G$ resulting in the change of α_1. A larger E'_{br} is needed when $\delta = 75$ is considered, since due to the drop of the magnetic field, E'_{br} should increase to produce the

peaks (both low- and high-energy) around the same frequency. A total jet luminosity up to $L_{jet} = 3.0 \times 10^{45}\ erg\ s^{-1}$ is needed to account for the observed data.

During the flares the second emission peak increased by intensity and shifted to HEs (middle right panel in fig. 3.7). The large Compton dominance and the detection of VHEs γ-rays indicates that *i)* the main contribution is from the photon fields external to the jet and *ii)* the emission region should be outside the BLR. Moreover, the different properties observed in the X-ray and γ-ray bands (e.g., the variability time scales, the flux increase amplitude, etc.) indicate that perhaps two different components are responsible for the emission in the X- and γ-ray bands. Accordingly, we assume that the X-ray emission is due to IC scattering of synchrotron photons, while the emission in the MeV/GeV bands is due to IC scattering of dusty torus photons. Both flares can be modeled not changing significantly $E'_{br} \approx 0.30\ GeV$ and $B = (0.42 - 0.47)\ G$. For Flare 1 and Flare 2 different α_1 are estimated, $\alpha_1 = 2.24 \pm 0.37$ and $\alpha_1 = 1.96 \pm 0.004$, respectively, since it is defined by the SSC component, and the X-ray spectrum, which is different for these flares. The required total jet luminosity did not change by much and is almost the same as in the quiescent state.

3C 279: Among the considered sources, most interesting and complex SEDs are observed for 3C 279 (lower panel in fig. 3.7). In the quiescent state the tail of the synchrotron emission is defined by the optical data, implying that the peak of the low-energy (synchrotron) component should be $< 10^{14}\ Hz$. The IC scattering of these synchrotron photons is in the Klein-Nishina regime ($\sim \gamma\ \nu_{syn}$), which means that it can explain the observed γ-ray data only if high δ is assumed. Thus, we assume two possibilities: when $\delta = 11.4$ is considered, the emission is explained by SSC, plus an additional contribution from BLR photons, instead, when $\delta = 36.5$, the emission in both X- and γ-ray bands are from IC scattering of synchrotron photons. In both cases, α_1 does not change significantly: $\alpha_1 = 1.98 \pm 0.11$ and $\alpha_1 = 1.91 \pm 0.01$ for $\delta = 11.4$ and $\delta = 36.5$, respectively. The break energy is higher when $\delta = 36.5$ is used ($E'_{br} = (2.86 \pm 0.11)\ GeV$ versus $E'_{br} = (0.14 \pm 0.01)\ GeV$), since the average energy of synchrotron photons is lower than that of BLR photons. When SSC+BLR model is used, the data can be explained for the jet with a total luminosity of $L_{jet} = 3.9 \times 10^{44}\ erg\ s^{-1}$, and both the electrons and the

magnetic field are almost in equipartition $U_e/U_B = 15.3$. For only SSC model, $L_{jet} = 2.9 \times 10^{46}\ erg\ s^{-1}$ and $U_e/U_B = 1.3 \times 10^5$.

During the Flare B, the emission in both optical and γ-ray bands increased, but it was almost constant in the X-ray band. Accordingly, in the fit we assume that the X-rays are due to another component, and require that SSC emission from the electron population producing the radio to optical emission does not over predict the observed X-ray flux (low right panel in fig. 3.7). HE emission is modeled by IC scattering of dusty torus photons on the electrons with the power-law indexes $\alpha_1 = 2.56 \pm 0.44$ and $\alpha_2 = 4.17 \pm 0.41$ changing at $E'_{br} \approx (0.48 \pm 0.10)\ GeV$, and $L_{jet} = 1.1 \times 10^{45}\ erg\ s^{-1}$.

During the Flare G, due to the simultaneous increase observed in the optical, X-ray and γ-ray bands, we conclude that the same SSC component is responsible for the emission in these bands. The emitting region size is larger (in (42) it has been shown that the flux variation time is 15 days), so a lower magnetic field $B = (560 \pm 30)\ uG$ is obtained which results in the change of other parameters, e.g., $E'_{br} = 11.72 \pm 0.98\ GeV$. The X-ray data allows the precise estimate of α_1 to be 2.10 ± 0.05, a value which is expected from strong shock acceleration theories. In the jet the particle energy strongly dominates over the magnetic field ($U_e/U_B > 10^5$) and the jet total luminosity is $L_{jet} = 4.8 \times 10^{47}\ erg\ s^{-1}$.

3.4.3. Discussions

The results of the study of the multiwavelength emission from PKS 1510-089, PKS 1222+216 and 3C 279 FSRQs are presented. The SEDs observed during quiescent and flaring states are modeled using one-zone leptonic synchrotron and IC models, taking into account the seed photons originating inside and outside of the jet. The obtained results allow to quantitatively evaluate the jet energetics, break energy in the underlying electron distribution in different states which are crucial for investigating the changes in the physical state of the jet which caused the flares. However, the parameters describing the underlying electron distribution below the break are poorly constrained, because the data describing the rising part of both low-energy and HE components are missing. It did not allow us to exactly identify the processes responsible for the acceleration of particles in the jet. In

principle, a similar study for the periods identified by the X-ray data can provide a chance to investigate the dominant particle acceleration processes, if the X-ray spectra define the rising part of the HE component.

Chapter 4

4. High Energy Gamma-Ray Emission from PKS 1441+25

4.1. INTRODUCTION

As it has been already mentioned, studying the emission from blazars not only helps to understand the physical processes occurring in the relativistic jets but sometimes also to measure the density of EBL photons. In this regards, particularly interesting are blazars observed at the large distances. The observed curvatures in the spectra from MeV/GeV to TeV bands puts straightforward constrain on the density of EBL photons. However, theoretical investigation of the processes occurring in the jets are necessary to check whether the curvatures in the spectra are due to similar features in the emitting particle spectra or are naturally formed due to EBL absorption. Therefore, particle acceleration and emission processes are deeply investigated in the distant blazars, PKS 1441+25 and CTA 102 (next chapter).

I start with very brief introduction on blazars (summarizing from previous chapters). Blazars are an extreme class of AGNs which have jets that are forming a small angle with respect to the line of sight (15). By their emission line features blazars are commonly grouped as BL Lacs and FSRQs (15). BL Lacs have weak or no emission lines, while FSRQs have stronger emission lines. Blazars are known to emit electromagnetic radiation in almost all frequencies that are currently being observed. Their broadband spectrum is mainly dominated by non-thermal emissions produced in a relativistic jet pointing toward the observer. A key feature of their nonthermal emission is the distinct variability at all frequencies (with different variability time scales - from years down to a few minutes). The shortest variability time scales are usually observed for the highest energy band; an example is the minute scale variability of PKS 2155-304 (79) and IC 310 (80) which implies that the emission is produced in a very compact region. Their SED has two broad non-

thermal peaks - one at the IR/optical/UV/X-ray and the other at the HE γ-ray band. The low-energy peak is believed to be due to the non-thermal synchrotron emission of relativistic electrons while for the origin of the second component IC scattering of low energy photons are proposed. The emission from BL Lacs are successfully explained by synchrotron/SSC processes while for FSRQs usually EIC models which are used. The external photon field can be dominated either by the photons reflected by (BLR; (25)) or by photons from a dusty torus (81) (26). Domination of one of the components mostly depends on the localization of the emitting region; for example, if the energy dissipation occurs within BLR then the observed HE emission is mostly due to IC scattering of BLR reflected photons, otherwise, if the emitting region is far from the central source, then the IC scattering of torus photons will dominate. SSC and EC models assume that the emission is produced by the same population of electrons, though up to now it is not clear whether it is produced in the same part of the jet or by different electron populations. Alternatively, the HE emission can be explained by the interaction of energetic protons; e.g., a significant fraction of the jet power goes for acceleration of protons so that they reach the threshold for pion production (30) (82).

The majority of the blazars detected in VHE γ-ray band are high-frequency-peaked BL Lacs for which the synchrotron bump is in the UV/X-ray bands. In addition to BL Lacs, there are also 5 FSRQs detected in the VHE γ-ray band (in 2017) which is rather surprising, since the BLR structure of these objects, which is rich in optical-UV photons, makes these environments strongly opaque to VHE γ-rays (83) (84). Moreover, FSRQs have a relatively steep photon index in the energy range of $> 100\ MeV$ as was observed with the *Fermi* LAT which does not make them as strong emitters of VHE γ-ray photons. Detection of FSRQs in the VHE γ-ray band is challenging for the near-black-hole dissipation scenarios; it assumes that the γ-rays are most likely produced farther from the central source, outside the BLR, where the dominant photon field is the IR emission from the dusty torus. Typically, the temperature of torus photons $\sim 10^3\ K$ is lower than that of the photons reflected in the BLR $\sim 10^5\ K$, and, in principle, VHE photons with energy up to $\sim 1\ TeV$ can escape from the region. Thus, the observations of FSRQs in VHE γ-ray band provide an alternative view of

blazar emission as compared to BL Lacs. Moreover, since FSRQs are more luminous than BL Lacs, they could, in principle, be observed at greater distances. Indeed, the farthest sources detected in the VHE γ-ray band are the FSRQs at a redshift of $z \geq 0.9$ (e.g., PKS 1441+25 (85), (86) and S3 0218+35 (87)). That is why FSRQs are ideal for estimation of the intensity of Extragalactic Background Light (EBL) through the absorption of VHE photons when they interact with the EBL photons (88), (89).

Among FSRQs, PKS 1441+25 is one of the most distant sources detected so far at $z = 0.939$ (90). In April 2015 both VERITAS and MAGIC collaborations announced the detection of VHE γ-rays from PKS 1441+25 (with up to 250 GeV photons) (91), (92). A strong emission from the source had been detected on April 20 to 27, 2015. During the same period, the source had been also observed with the telescopes Swift and NuSTAR. The origin of the multiwavelength emission from PKS 1441+25 observed in April is modeled assuming the emission region is beyond the BLR, and the emission in the VHE γ-ray band is mostly due to the IC scattering of the dusty torus photons (85) (86). Moreover, the large distance to PKS 1441+25 allowed to indirectly probe the EBL absorption at redshifts up to $z \sim 1$ with the help of ground-based γ-ray instruments.

In the theoretical interpretation of the multiwavelength emission from blazars, the size/location of the emitting region, magnetic field and electron energy distribution are uncertain. Only during flaring periods some of the unknown parameters can be constrained based on the observations in different bands. The observations of PKS 1441+25 during the bright period in April 2015 by different instruments provide us with data on the maximums of the emitting components (Swift UVOT/ASAS-SN and *Fermi* LAT) as well as on the transition region between these components in the energy range from 0.3 to 30 keV (Swift XRT and NuSTAR) (85). Similar data (up to HE γ-ray band) are available also from the observations carried out on January 06 to 28, 2015, which is the period of the large flare that was observed with *Fermi* LAT. Thus, by modeling the emission in these two periods and estimating the parameter space that describes the underlying particle distribution responsible for the emission through MCMC technique, one can investigate and explore particle acceleration/emission processes and jet properties in these two significant flaring

periods which are crucial for understanding the origin of the flares. This motivated us to have a new look at the origin of the multiwavelength emission from PKS 1441+25, using currently available data from Swift, NuSTAR and *Fermi* LAT.

4.2. Fermi LAT DATA ANALYSIS

The Large Area Telescope on board the Fermi satellite is a pair-conversion telescope sensitive to γ-rays in the energy range from $20\,MeV$ to $300\,GeV$. It constantly scans the whole sky every 3 hours already more than 8 years. More details about *Fermi* LAT can be found in (93). For studying the spectra of PKS 1441+25 during the flaring periods, the publicly available Fermi LAT data acquired in the periods from January 06 to 28 and from April 15 to 26, 2015. These two periods have been picked, because they are contemporaneous with the Swift XRT observations of the source (85). The data were analyzed with the standard *Fermi* Science Tools v10r0p5 software package released on May 18, 2015 available from the *Fermi* Science Support Center (94). The latest reprocessed PASS 8 events and spacecraft data are used with the instrument response function P8R2_ SOURCE_ V6. The photons in the energy range from 100 MeV to 100 GeV from a region of interest defined as a circle of a 20°radius centered at the γ-ray position of PKS 1441+25 $(RA, Dec) = (220.996, 25.039)$ (95) are downloaded. Only the events with higher probability of being photons $(evclass = 128\, evtype = 3)$ have been considered in the analysis. A cut on the zenith angle of 90° is applied to reduce contamination from the Earth-limb γ-rays produced by cosmic rays at their interaction with the upper atmosphere. The model file, describing the region of interest, contains point sources from the *Fermi* LAT third source catalog (95) (3FGL) within 25° from the target, as well as contains Galactic gll_iem_v05_rev1 and isotropic iso_source_v05 diffuse components. All point-source spectra were modeled with those given in the catalog, allowing the photon index and normalization of the sources within 20° to be free in the analysis. Also, the normalization of diffuse background components was not fixed.

Table 4.1. The best parameters obtained with *gtlike* for power-law modeling. For each time period, photon flux in the range $0.1 - 100\ GeV$, photon index and detection significance are presented.

Parameter name	*Blue*	*Red*
Flux $(photon\ cm^{-2}s^{-1})$	$(5.89 \pm 0.30) \times 10^{-7}$	$(3.63 \pm 0.36) \times 10^{-7}$
α	1.99 ± 0.04	1.74 ± 0.06
TS	2174	910

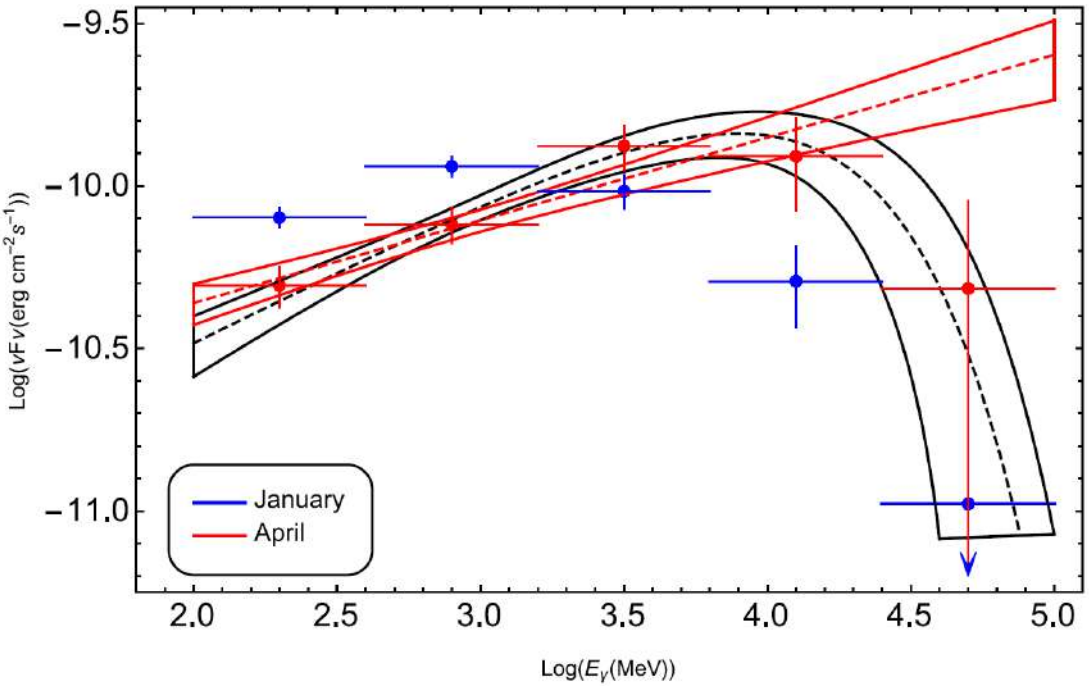

Figure 4.1. The γ-ray spectrum of PKS 1441+25 above $100\ MeV$ averaged over the *Fermi* LAT observations in January (blue) and April (red).

4.2.1. Spectral analysis

In order to find the best matches between spectral models and events, an unbinned likelihood analysis is performed with *gtlike*. The PKS 1441+25 spectrum has been initially modeled as a power-law function where the normalization and the power-law index are taken as free parameters. The best fit parameters obtained with *gtlike* analysis are presented in Table 4.1 and the corresponding spectrum is shown in fig. 4.1 (blue and red data for January and April, respectively). The spectrum is calculated by separately running *gtlike* for 5 energy bands equal on a log scale.

The fluxes presented in Table 4.1 significantly exceed the averaged flux given in 3FGL ($\approx 1.28 \times 10^{-8}\ photon\ cm^{-2}s^{-1}$) (95). The photon index estimated in January 2015 is consistent with the value reported in 3FGL $\alpha = 2.13$ (averaged over 4 years of

observations); however, a relative hardening of $\alpha = 1.74 \pm 0.06$ is observed in April, which is rarely observed for FSRQs. Moreover, we note an indication of deviation of the power-law model with respect to the data above $10\,s$ of GeV energies observed in April (red bowtie plot in fig. 4.1). In order to check for a statistically significant curvature in the spectrum, an alternative fit of the power-law with an exponential cutoff function in the form of $dN/dE \sim E_\gamma^{-\alpha} \times Exp(-E_\gamma/E_{cut})$ is done, which results in $\alpha = 1.56 \pm 0.1$ and $E_{cut} = 17.7 \pm 8.9\,GeV$ (black bowtie plot in fig 4.1). The power-law and cutoff models are compared with a log likelihood ratio test: the TS is twice the difference in the log likelihoods, which gives 8 for this case. Note that the TS probability distribution can be approximated by a χ^2 distribution with 1 degree of freedom (dof) corresponding to the difference of the dof between the two functions. The results give $P(\chi^2) = 0.0046$, which again indicates a deviation from a simple power-law function. The best-fit cutoff power-law function is shown as a black bowtie line in fig. 4.1. However, 2.8σ is not a high enough significance to claim for a statistically significant curvature although it is as high as $3.86\,\sigma$ if the data collected during the whole month of April are considered.

4.2.2. Temporal analysis

In order to investigate the size of the γ-ray emitting region, light curves with different time binning are generated. A characteristic timescale for flux variation τ would limit the (intrinsic) size of the emission region to $R \leq c \times \delta \times \tau/(z+1)$. Thus, it is crucial to do a variability analysis in order to distinguish between different emission processes.

The light curve of PKS 1441+25 for the period from January to December 2015 has been calculated by the *gtlike* tool, applying the unbinned likelihood analysis method. $(0.1 - 100)\,GeV$ photons from a region with a 10° radius centered on the position of PKS 1441+25 are used in the analysis with the appropriate quality cuts applied as in the previous case. During the analysis, in order to reduce the uncertainty in the flux estimations, in the model file the photon indices of all background sources are fixed to the best guess values. Two different sets of light curves are calculated, considering the power-law index of PKS 1441+25 as being fixed and then as free. Since no variability is expected for the background

diffuse emission, the normalization of both background components is also fixed to the values obtained for the whole time period.

The γ-ray light curve of PKS 1441+25 obtained with one-day and three-days binning is presented in fig. 4.2 (a) (blue and green data respectively). In the light curve there can be identified several periods when the flux was in high as well as in quiescent states. A major increase of the γ-ray flux had been detected in the period from January 21 to 28, 2015, with a daily averaged maximum of $(1.55 \pm 0.18) \times 10^{-6}\, photon\, cm^{-2} s^{-1}$ observed on January 25, 2015. Unfortunately, the peak flare of January 25 was not observed by Swift. The γ-ray photon index evolution in time in a three-day long binning is shown in fig. 4.2 (c) with green data (three-day long binning is used since the photon index uncertainties are less than in one-day binning). During the flaring period the photon index is $1.9 - 2.0$. Also an increase in the flux can be noticed around January 22nd which lasted just one day. In order to check if this brightening is statistically significant, light curves with denser time sampling (half a day and 4 hours) are generated. However, the corresponding flux increase is within the uncertainty of the surrounding bins, while the peak of the flux around 25th of January is present in both light curves. In addition, a substantial increase in the γ-ray flux was observed in April, from June to about July 15, mid-August and around October-November; but the maximum flux intensity was lower as compared with that observed during the strong γ-ray outburst of January 21 to 28 (fig. 4.2). The active state in April is the period when PKS 1441+25 was observed by MAGIC on MJD 57130-57139 and VERITAS on MJD 57133-57140 (85), (86). The γ-ray light curve with three-day binning shows that, between MJD 57125.56- 57140.64 (from April 13 to April 28, 2015), the γ-ray photon index is significantly harder, $\Gamma = (1.73 - 1.79)$. It implies that during the observations in the VHE band the source was in a state characterized by a hard γ-ray photon index in the MeV-to-GeV range.

Next, in order to investigate the flux changes in time, and in particular in the flaring periods, the light curves have been generated by an adaptive binning method. In this method, the time bin widths are flexible and chosen to produce bins with constant flux uncertainty (96). This method allows detailed investigation of the flaring periods, since at

times of a high source flux, the time bins are narrower than during lower flux levels, therefore the rapid changes of the flux can be found. In order to reach the necessary relative flux uncertainty, the integral fluxes are computed above the optimal energies (96) which correspond to $E_0 = 215.4\ MeV$ in this case.

Figure 4.2. The γ-ray light curve of PKS 1441+25 from 2015 January to December (a). The bin intervals correspond to 1 day (blue data) and 3 days (green data). The light curve obtained by adaptive binning method assuming 20 per cent of uncertainty is presented in red (b). The changes of photon index for 3-day binning (green) and with adaptive binning method are shown in (c).

Adaptively binned light curves in the $215\ MeV - 300\ GeV$ energy range with 20% and 15% uncertainties have been generated. Flare is present in both light curves. The light curve with 20% flux uncertainty at each bin is presented in fig. 4.2 (b) with red color. It confirms all the features visible in the constant-bin-width light curve, but also allows us to investigate fast variability during high-flux states in greater detail. The first flare episode occurred

during MJD 57043.30-57049.38, when the time width was less than $\sim 15\ hours$. A strong flaring period is observed around the $24th - 25th$ of January. The flux peak of $(1.14 \pm 0.24) \times 10^{-6}\ photon\ cm^{-2}\ s^{-1}$ was observed on the $24th$ of January at 22:35 pm in a bin with a half-width of $3.1\ hours$. The analysis of the data acquired in the mentioned period on the energies of $> 100\ MeV$ results in a flux of $(2.22 \pm 0.38) \times 10^{-6}\ photon\ cm^{-2} s^{-1}$, which is the highest photon flux detected from this source. The data analysis for the entire flaring period (January 21-28) resulted in a flux of $(1.05 \pm 0.06) \times 10^{-6}\ photon\ cm^{-2} s^{-1}$ and a photon index of $\sim 1.98 \pm 0.04$ (97). After MJD 57049.38, PKS 1441+25 was in its quiescent state, and the data should be accumulated for more than a day to reach 20 % uncertainty. Then from MJD 57109.89 to MJD 57143.91, PKS 1441+25 was again in its active state which was characterized by emission with a significantly hardened γ-ray photon index. Starting from MJD 57126.70 to MJD 57141.93, the photon index of PKS 1441+25 hardened and reached ≤ 1.9 most of the time. Measured within a few hours, the photon index kept varying from $\Gamma = 1.73$ to $\Gamma = 1.91$. The hardest photon index of $\Gamma = 1.54 \pm 0.16$ was observed on MJD 57131.46 with 11.8σ and the data being accumulated for $\approx 29\ hours$. Other periods, when PKS 1441+25 was bright enough to be detected on sub-day scales, are MJD 57177.38-57199.76 and MJD 57243.02-57249.39. For the rest of the time the source was in its quiescent state and the data should be accumulated for a few days or even longer in order to detect the source. The analysis of the light curve with the new adaptive binning method for the first time allowed us to investigate the flaring activity of PKS 1441+25 with a sub-day resolution and to perform detailed investigation of the flux and photon index changes.

Furthermore, to derive the flare doubling timescales and understand the nature of the January flare, the light curve is fitted with an exponential function in the form of (98)

$$F(t) = F_c + F_0 \times \left(e^{\frac{t-t_0}{t_r}} + e^{\frac{t_0-t}{t_d}} \right)^{-1}, \tag{4.1}$$

where t_0 is the time of the maximum intensity of the flare (F_0), F_c is the constant level present in the flare, t_r and t_d are the rise and decay time constants, respectively.

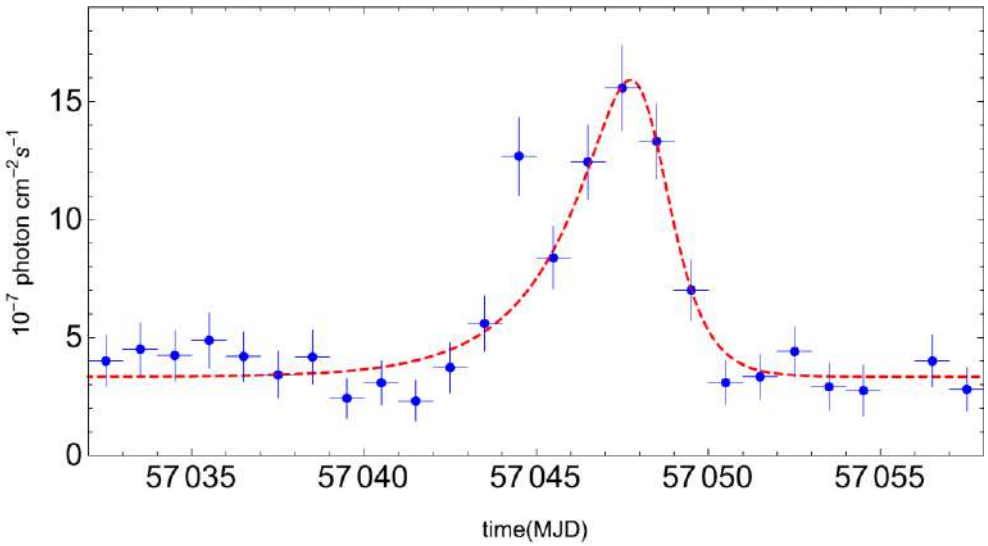

Figure 4.3. The light curve's sub interval that covers a major flaring period. The red dashed line shows the flare fit with Eq. 4.1.

The fit shows that the flare is best explained when $t_0 = 57048.25 \pm 0.18$, $t_r = 1.92 \pm 0.3$, $t_d = 0.72 \pm 0.1$ and $F_0 = (22.6 \pm 1.4) \times 10^{-7}\ photon\ cm^{-2}s^{-1}$. The fit of the flaring period is shown in fig. 4.3 with a dashed red line. Using this technique, it is also possible to estimate the shortest time variability (flux doubling) defined by $\tau = 2t_{r,d}$, corresponding to $\tau = 1.44\ days$ which is used to put an important constraint on the radiative region size. We note that the previous PKS 1441+25 γ-ray emission studies with the *Fermi* LAT data that covered only the period in April did not allow to properly estimate the γ-ray emitting region size, while here the analysis of the flaring period in January allowed to constrain the flare doubling time which is necessary for constraining the γ-ray emission region size.

4.3. BROADBAND SED MODELLING

It is hard to make theoretical modeling of the observed broadband SED because the structure of the central region of blazars is complex and the exact localization of emitting regions is unknown. The observed fast variability indicates compactness of the emitting region but its localization remains an open problem. Along the jet, the emission can be produced in different zones and depending on the distance from the central black hole different components can contribute to the observed emission (41).

4.3.1 Broadband SED

The broadband SEDs of PKS 1441+25 for different periods are shown in fig. 4.4 where with red and blue colors are the SED observed in January and April respectively, while the archival data from ASI science data center (99) are shown with gray color. We note that during the high states, the second emission peak increased by intensity and shifted to HEs. This kind of change has already been observed during the flaring state of 4C+49.22 (100) and PKS 1510-089 (101). During the flaring periods the low-energy component's intensity increased as compared with the quiescent state; the increase in April exceeded that one observed in January (although the power-law photon index in the X-ray band (≈ 2.3) had been relatively constant during both observations). More evident and drastic is the change of the peak intensity of the low energy component; from January to April it increased by nearly an order of magnitude and as compared with the quiescent state it increased ≥ 15 times. On the contrary, the peak of the second component (in the HE γ-ray band) is relatively constant, only the photon index in the MeV-GeV energy range is harder during the observations in April. The Compton dominance of the source is stronger and evident during the flaring periods, which suggests that the density of the external photon fields significantly exceeds the synchrotron photon density ($U_{ext}/U_{syn} \gg 1$).

Such a strong amplification of the emission from blazars can be explained by means of introducing changes in the emission region parameters, e.g., in the magnetic field, emitting region size, bulk Lorentz factor and others, and/or particle energy distribution. In principle, all the parameters describing the emitting region can be changed at the same time if the flares are due to a global change in the physical processes in the jet, which also affect the jet dynamics and properties. However, usually, the change in one or two parameters is enough to explain the flares. An interesting study of the flaring activity in FSRQs as a result of changes in different parameters has been investigated in (76). Namely, the emission spectra evolution as a function of changes in different parameters (e.g., bulk Lorentz factor, magnetic field, accretion rate, etc.) is investigated. In the case of PKS 1441+25, during its flaring periods, both the low energy and HE components increased several times. The increase of the second component is most likely due to moving of the emitting region

outside its BLR. In principle, there are two possibilities: *i)* either the emitting region moves faster due to increasing bulk Lorentz factor and leaves the BLR or ii) the bulk Lorentz factor is unchanged and only the emitting region is moving beyond the BLR. In the first case, since the external photon density in the commoving frame of the jet depends on the Doppler boosting factor, a strong increase in the Compton dominance will be observed. We note that the change of the bulk Lorentz factor will also affect the low energy component. In the second case, the flaring activity is due to the change of the location of the emitting region and due to the magnetic field amplification. Additional increase of the magnetic field from January to April is also evident when the low energy component kept increasing (this corresponds to the case shown in fig. 1 (b) in (76)). Accordingly, we discuss two possibilities. First, we assume that δ has increased from 10 in the quiescent to 18 in the flaring periods, and then we assume that it was constant ($\delta = 18$) in both periods. These values are below and above the estimated mean bulk Lorentz factor of FSRQs obtained from the analysis of a large sample of γ-ray emitting FSRQs (102). The emission region size can be estimated through the observed variability time scale $\tau = 1.44\, d$ implying that $R_b \leq \delta c\tau/(1+z) \approx 3.5 \times 10^{16}\, cm$ when $\delta = 18$ and $R_b = 1.92 \times 10^{16}\, cm$ when $\delta = 10$.

4.3.2. Theoretical modeling

The SEDs in the high states of January and April as well as in the quiescent state are modelled. Even if a quiescent state SED is constrained with non-simultaneous data, its modeling provides an insight into the dominant physical processes which are constantly present in the jet but are covered by the flaring components during the high states.

We modeled the PKS 1441+25 SED for high and quiescent states in the framework of single-zone leptonic models that include the synchrotron, SSC, and EC processes. The emission region (the "blob"), assumed to be a sphere with a radius of R which is moving with a bulk Lorentz factor of Γ, carries a magnetic field with an intensity of B and a population of relativistic electrons. The blob velocity makes a small angle with respect to the line of sight, so the emission is amplified by a relativistic Doppler factor of δ. The energy spectrum of the population of electrons in the jet frame, which is responsible for the non-

thermal emission is assumed to have a broken power-law shape:

$$N'_e(E'_e) = \begin{cases} N'_0 \left(\frac{E'_e}{m_e c^2}\right)^{-\alpha_1} & E'_{e,min} \leq E'_e \leq E'_{br} \\ N'_0 \left(\frac{E'_{br}}{m_e c^2}\right)^{\alpha_2-\alpha_1} \left(\frac{E'_e}{m_e c^2}\right)^{-\alpha_2} & E'_{br} \leq E'_e \leq E'_{e,max} \end{cases} \quad (4.2)$$

Where N'_0 is connected with the total electron energy $U_e = \int_{E'_{e,min}}^{E'_{e,max}} E'_e N'_e(E'_e) dE'_e$, α_1 and α_2 are the low and high indexes of electrons correspondingly below and above the break energy E'_{br}, and $E'_{e,min}$ and $E'_{e,max}$ are the minimum and maximum energies of electrons in the jet frame, respectively. The electron spectrum given in Eq. 4.2 is naturally formed from the cooling of relativistic electrons (47) (46).

The low-energy (from radio to optical/X-ray) emission is due to the synchrotron emission of electrons with an energy spectrum as given by Eq. 4.2 in a homogeneous and randomly oriented magnetic field. For the quiescent state we assume the energy dissipation occurs close to the central source region and it is explained as an IC scattering of synchrotron photons (SSC). Instead the high state emission is dominated by that from a region well outside the BLR in order to avoid the strong absorption of photons with energies $\geq 100\, GeV$ (similar assumptions have been already made in (85), (86)). In this case the dominant external photon field is the IR radiation from the dusty torus which, as we assume, has a blackbody spectrum with a luminosity of $L_{IR} = \eta L_{disk}$ ($\eta = 06$, (26)) and a temperature of $T = 10^3\, K$ and fills a volume that for simplicity is approximated as a spherical shell with a radius of $R_{IR} = 3.54 \times 10^{18} (L_{disk}/10^{45})^{0.5}\ cm$ (43). The disk luminosity is estimated from the BLR luminosity, $L_{disk} = 10 \times L_{BLR} \approx 2 \times 10^{45}\, erg\, s^{-1}$ (103).

4.3.3. Fitting technique

In order to constrain the model parameters, the code described in Chapter 3.3 is used. It uses MCMC method, which enables to derive the confidence intervals for each model parameter. It derives the best-fit and uncertainty distributions of spectral model parameters through MCMC sampling of their likelihood distributions. The prior likelihood, our prior knowledge of the probability distribution of a given model

parameter and the data likelihood functions are passed onto the emcee sampler function for an affine-invariant MCMC run. We run the sampling with 64 simultaneous walkers, for 100 steps of burn-in, and 100 steps of run. In the parameter sampling, the following expected ranges are considered: $1.5 \leq (\alpha_{1,2}) \leq 10$, $0.511\,MeV \leq E'_{(br,min,max)} \leq 1\,TeV$, and N_0 and B are defined as positive parameters. The synchrotron emission is calculated using the parameterization of the emissivity function of synchrotron radiation in random magnetic fields presented in (77) while the IC emission is computed based on the monochromatic differential cross section of (78).

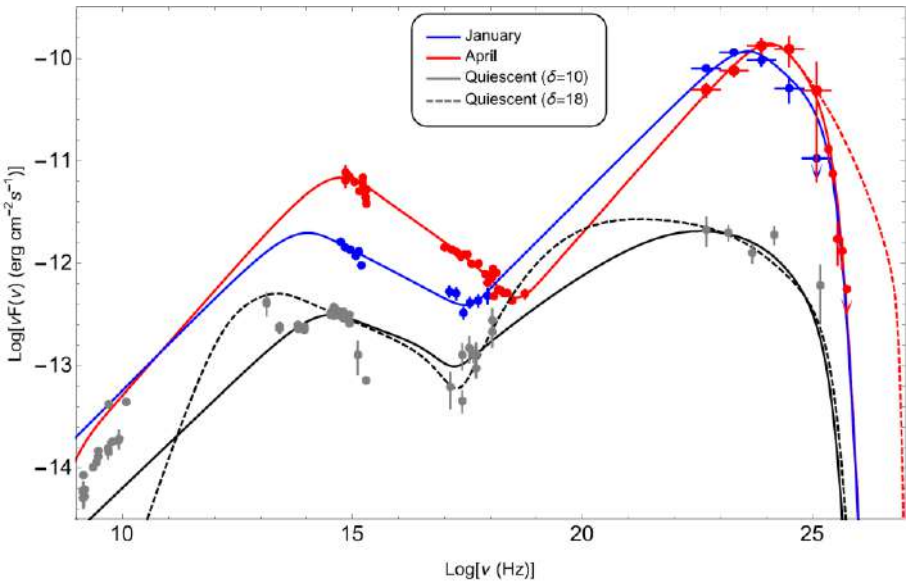

Figure 4.4. The broadband SED of PKS 1441+25 for January (red), April (blue) and for the quiescent state (gray). The blue, red and gray lines are the models fitting the data with the electron spectrum given by Eq. 4.2 for January, April and for the quiescent state, respectively. The model parameters are presented in Table 4.2. The UV-X-ray and VHE γ-ray data observed in January and April are from (85) and HE γ-ray data (*Fermi* LAT) are from this work.

4.3.4. SED modeling and results

The results of SED modeling are shown in fig. 4.4 with the corresponding parameters in Table 4.2. The radio emission is due to the low-energy electrons which are accumulated for longer periods, that is why, the radio data are treated as an upper limit for the purposes of our modeling. To have an indication of a change in the energetic contents of the jet, as well as of changes in the radiating particle distribution, first we try to fit the SED in a quiescent

state which is modeled assuming two different Doppler boosting factors. The gray solid line in fig. 4.4 shows the synchrotron/SSC emission assuming that the jet Doppler boosting factor is $\delta = 10$, and the gray dashed line is the case of $\delta = 18$. In case of $\delta = 10$, as the emitting region size is as small as $R_b = 1.92 \times 10^{16}\, cm$, the magnetic field should be as strong as $B = 0.19\, G$ to account for the observed data, while at $\delta = 18$ the magnetic field is much weaker, $B = 0.046\, G$. Also, the underlying electron distribution for the case of $\delta = 10$ is characterized by a slightly higher break ($2.83\, GeV$ versus $1.11\, GeV$) in order to account for the observed emission.

The emission in flaring periods is modeled assuming that the HE emission is entirely due to the IC scattering of external photons (fig. 4.4). In all calculations the absorption due to the EBL was taken into account using a model from (62) since a strong absorption is evident at $\geq 100\, GeV$ (red dashed line in fig. 4.4). In both periods the HE electron spectral index is within the range of $\alpha_2 \sim (3.46 - 3.64)$ which is required to explain the UV-X-ray data with a photon index of ≈ 2.3. The lack of low-energy data makes the precise estimation of the low energy electron index harder. Only the Swift XRT/NuSTAR data from the observation of the transition region between low and high energy (HE;$> 100\, MeV$) components allows to define the parameters E_{min} and α_1. The low energy electron index is in a typical range expected from shock acceleration theories, $\alpha_1 \approx 2$.

Table 4.2. Model parameters

	Parameter	***Quiescent***	***Quiescent***	***January***	***April***
Doppler factor	δ	10	18	18	18
Normalization of electron distribution	$N_0' \times 10^{48} eV^{-1}$	$10.68^{+3.09}_{-2.64}$	$43.44^{+6.59}_{-7.76}$	$23.83^{+8.11}_{-7.32}$	$6.12^{+1.67}_{-1.56}$
Low-energy electron spectral index	α_1	2.14 ± 0.04	$2.09^{+0.03}_{-0.04}$	$2.10^{+0.04}_{-0.05}$	1.98 ± 0.03
High-energy electron spectral index	α_2	$3.39^{+0.27}_{-0.14}$	3.38 ± 0.06	3.46 ± 0.06	3.64 ± 0.01
Minimum electron energy	$E'_{min}(MeV)$	$1.84^{+1.75}_{-1.23}$	$286.37^{+30.64}_{-25.39}$	$1.97^{+0.31}_{-0.34}$	$4.16^{+1.00}_{-1.86}$

Table 4.2. (Continued)

Break electron energy	$E'_{br}\ (GeV)$	$2.83^{+0.51}_{-0.31}$	$1.11^{+0.14}_{-0.12}$	$1.62^{+0.23}_{-0.15}$	$3.11^{+0.15}_{-0.23}$
Maximum electron energy	$E'_{max}\ (GeV)$	$46.27^{+49.74}_{-13.76}$	$82.32^{+13.47}_{-17.14}$	$127.82^{+26.74}_{-24.75}$	$202.79^{+21.2}_{-14.6}$
Magnetic field	$B\ [G]$	0.19 ± 0.013	0.046 ± 0.002	$0.11^{+0.005}_{-0.004}$	$0.18^{+0.009}_{-0.006}$
Jet power in magnetic field	$L_B \times 10^{43} ergs^{-1}$	0.49	0.31	1.71	4.51
Jet power in electrons	$L_e \times 10^{45} ergs^{-1}$	2.11	4.07	9.60	4.47

As distinct from the quiescent state, in order to explain the flaring activities, both, the electron distribution and the magnetic field should be varying. We note that the magnetic field required for modeling of flaring periods, $B \geq 0.11\,G$, is weaker than that one estimated in the quiescent state in case of $\delta = 10$ ($B \sim 0.19\,G$). Since the synchrotron emission depends on the total number of emitting electrons N_e, δ and magnetic field strength B, in case of smaller δ (and emitting region size) the magnetic field should be stronger. Instead, when δ is constantly equal to 18 in both states, the magnetic field should be nearly ~ 2.4 and ~ 3.9 times stronger in January and April, respectively, in order to explain the observed data. As the synchrotron photon density is proportional to B^2, the increase in the magnetic field strength resulted in the observed increase of the synchrotron flux by a factor of 5.7 and 15.3 (fig. 4.4). In the modeling of the SEDs observed in the flaring periods of January and April, the magnetic field should be changed in accordance with the increase in the low energy component. Since the emission in the HE band is dominated by the IC scattering of external photons, this component remains stable during those periods (this corresponds to fig. 1 (b) in (76)).

The electron spectra obtained during the fit of SEDs in quiescent and flaring states are shown in fig. 4.5. It is clear the evolution of the electron spectra during the quiescent and high states. The low energy indexes of the underlying electron distribution in the quiescent state ($\delta = 10$) are softer as compared with the flaring period (April). The total electron energy for modeling the emission in the quiescent period, when $\delta = 18$, is almost of the

same order as that in the flaring periods, which is expected, as the magnetic field is weaker, most of the jet energy is carried by particles.

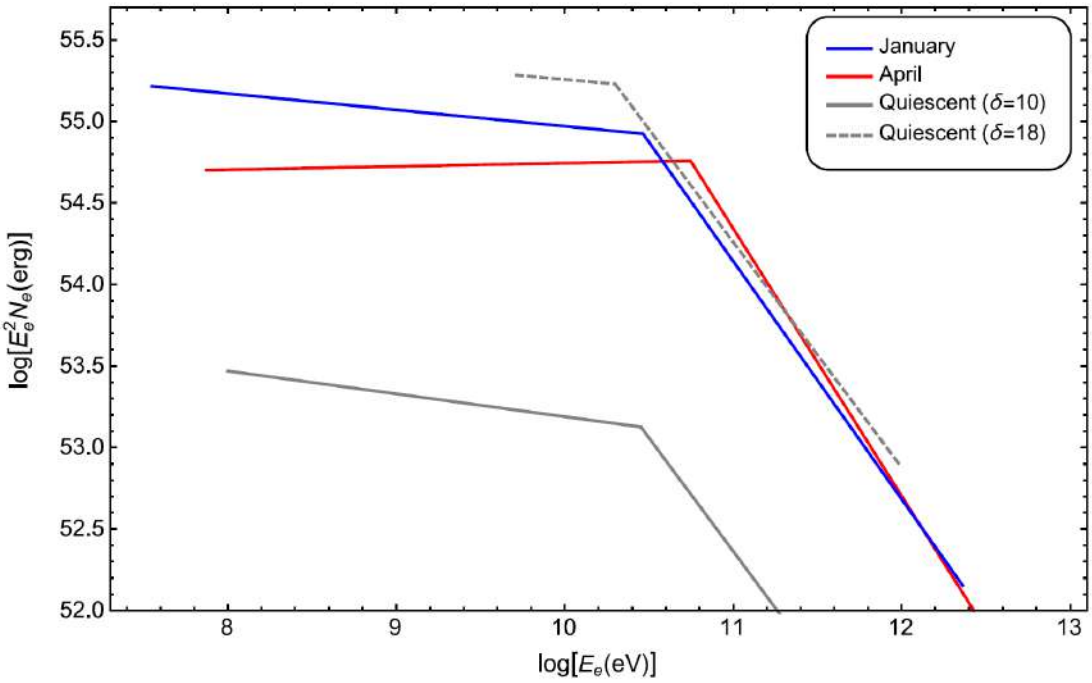

Figure 4.5. The electron spectra (broken power laws) obtained from the fit of the quiescent and flaring states of PKS 1441+25. Details on the parameter values are given in Table 4.2.

During the flaring periods, there are evident changes also in the underlying electron distribution. The electron distribution best describing the data observed in April hints at *i)* hardening of the low energy index, *ii)* a higher break at $\sim 3.1\ GeV$ and maximum energies of $\sim 203\ GeV$. E_{br} and E_{max} are expected to shift, as the γ-ray spectrum observed in April is slightly inclined toward HEs, as compared with the January spectrum (see fig. 4.4). However, due to the large uncertainties in the estimations, especially for α_1 (since the data in between $100\ keV$ and $100\ MeV$ are missing), no definite conclusions can be drawn. For a statistically significant claim for hardening, there are required additional data in the energy range characterizing the rising part of the low and HE components, which will allow to constrain α_1 with higher confidence. We note, however, that the significant hardening of the γ-ray emission observed in April (fig. 4.2 (c)) supports and strengthens the assumptions on the hardening of the low energy electron index.

Similar modeling of the SED of PKS 1441+25 observed in April has been already done in (85), but it was done in a different manner. For example, in (86) the low electron energy

index is fixed to be $\alpha_1 = 2$, a value expected from strong shock acceleration theories, while in our case all the parameters can vary in the fitting procedure. After having observed the hardening of the γ-ray photon index in April, we believe that exact estimation of α_1 is important. Moreover, possible hardening or softening of α_1 would point out the acceleration processes in the jet. However, the main difference in the modeling presented here, as compared with the previous ones, is the size of the emitting region (blob). They used larger blob size, $5 \times 10^{16}\, cm$, in (86) and $4 \times 10^{17}\, cm$ in (85). In our case, the modeling of the January flare time profile allowed us to constrain the emitting region size by $R_b \leq 3.5 \times 10^{16} \left(\frac{\delta}{18}\right) cm$. Another difference with the previously reported parameters is that in our case the electron energy density is nearly 100 times higher than the magnetic field energy density. In (85) $U_e/U_B = 1.5$, which is related to the fact that much bigger emitting region size is used. We note that in (86), where the considered blob size is similar to our case, they also found that $U_e/U_B \geq 10$. Moreover, in our case the radius of the IR torus is derived from a different scaling law, which can cause additional difference in the estimation of the total energy. Despite using different approaches and parameters as compared with those used in the previous modelings, we note, that the main parameters for the underlying electron distribution obtained during April are similar to the previously reported values.

4.4. DISCUSSION and CONCLUSIONS

We present the results of the study of the γ-ray emission from PKS 1441+25 during January-December 2015. The data from the observations of a bright GeV flare in January allow us to estimate the emitting region size whereas the modeling of the broadband SED of PKS 1441+25 in January and April provided a chance to probe into the physical process during the flaring periods.

The γ-ray light curve generated with an adaptive binning method shows that the source entered its high activity state around MJD 57043.3 and the flux reached its maximum on January 24, when, within a few hours, the flux increases up to $F_\gamma(> 100MeV) = (2.22 \pm 0.38) \times 10^{-6}\ photon\, cm^{-2}\, s^{-1}$. During this γ-ray brightening the fit of the flare profile

shows a slow rise and a fast decay trend with the shortest variability (flux doubling) time being $\tau_d = 1.44\ days$. The rise of the flare can be attributed to the shock acceleration, whereas the decay phase cannot be explained by cooling of particles. Indeed, for the electrons that emit γ-rays with $\epsilon_\gamma = 1\ GeV$, as measured in the observer frame, the corresponding cooling timescale would then be $\sim(3m_e c/\sigma_T u_{IR}) \times (\epsilon_{IR}(1+z)/\epsilon_\gamma)^{0.5}$ (19) which corresponds to $0.47\ days$ in this case. This timescale is shorter than the observed e-folding decay timescales of the flares, implying that the observed flux decrease is related to the processes other than radiative losses.

After the flare on MJD 57049.38, the source is in its quiet state and the next increase in the flux is observed starting from MJD 57109.89. Even if during this period, the flux amplitude is lower than one that observed in January, an interesting modification of the γ-ray emission spectrum is observed. First, the γ-ray photon index hardened during MJD 57126.70-57141.93, it was ≤ 1.9. This period coincides with the one when VHE γ-rays from PKS 1441+25 were detected. The hardest γ-ray photon index, $\Gamma = 1.54 \pm 0.16$, has been observed on MJD 57131.46 with a convincingly high detection significance of 11.8σ. This photon index is unusual for FSRQs which are with an averaged photon index of 2.4 in the third *Fermi*-LAT AGN catalog (see fig. 8 of (104)). This photon index is even harder than the index of B3 1151+408 ($\Gamma = 1.77$) which has the hardest photon indexes in the clean sample of *Fermi* LAT detected FSRQs. Although, hard photon indexes have been occasionally observed during rapid flaring events in FSRQs (105). The observed hardening was perhaps related to the emission of new energetic particles that were either injected into the emitting region or re-accelerated. Next, the data analysis covering only the period in April shows that the γ-ray flux hints at a spectral curvature and a power-law with an exponential cut-off model is preferred over the simple power-law modeling assuming a break around $E_{cut} = 17.7 \pm 8.9\ GeV$ with a significance of 2.8σ. Although the low statistics does not allow to claim for a statistically significant curvature in the spectrum, the γ-ray photon index observed in the VHE γ-ray band ($\sim$5.4, which corresponds to an intrinsic index of 3.4 after correction for the EBL) strongly supports the presence of a break or a cut-off in the PKS 1441+25 spectrum around tens of GeV. Most likely, this break is defined by the break

present in the radiating electron spectrum rather than is caused by the absorption within BLR (84) (otherwise the photons with $> 100\ GeV$ would be strongly absorbed).

The origin of multiwavelength emission: The SEDs observed during quiescent and flaring states are modeled using one-zone leptonic models and the model parameters are estimated using the MCMC method. The HE γ-ray emission observed in the flaring states can be explained by IC scattering of IR photons from the dusty torus whereas the SSC model gives a satisfactory representation of the data observed during the quiescent state. The flares observed in January and April can be explained assuming there are changes in the bulk Lorentz factor or in the magnetic field. If the emitting region leaves the BLR region due to the increase of the bulk Lorentz factor (from $\delta = 10$ to $\delta = 18$), the Compton dominance will increase as it has been observed in the γ-ray band. Indeed in the flaring states, the IC to synchrotron luminosities ratio $\mathrm{L}_\gamma / \mathrm{L}_{\mathrm{syn}} \approx 200$ and ≈ 28 in January and April, respectively as compared with that in the quiescent state $\mathrm{L}_\gamma / \mathrm{L}_{\mathrm{syn}} \approx (2-4)$. At the same time, the increase in the low energy component indicates that the magnetic field also increased between the flares in January and April (76). On the other hand, if the bulk Lorentz factor is unchanged ($\delta = 18$), only the change in the emitting region location and amplification of the magnetic field can explain the multifrequency behavior observed during the flares. It is possible to distinguish between these two scenarios, provided there are data in the hard X-ray or soft γ-ray band, as the modeling with $\delta = 18$ predicts a higher flux in the hard X-ray band than when $\delta = 10$ is assumed (grey dashed and solid lines in fig. 4.2). Such data are missing in this case, making it hard to give exact interpretation of the origin of the flare. Anyway, physically reasonable parameters are used in both of these scenarios.

When comparing the electron parameters required for the modeling of the SEDs in January and April, we find a hint of possible hardening of the low energy electron index in April. We note, however, that no definite conclusions can be drawn since α_1 is poorly constrained (due to missing or nonsufficient data). For all that, the April hardening of the γ-ray photon index in the MeV-GeV energy region supports our assumptions on hardening of the power-law index of the underlying electron distribution.

Jet Energetics: The jet power in the form of magnetic field and electron kinetic energy

are calculated by $L_B = \pi c R_b^2 \Gamma^2 U_B$ and $L_e = \pi c R_b^2 \Gamma^2 U_e$, respectively, and are given in Table 4.2. The jet power in the electrons changes in the range $(4.5 - 9.6) \times 10^{45}\ erg\ s^{-1}$ during the flares, while in the quiescent state it is of the order of $(2.1 - 4.1) \times 10^{45}\ erg\ s^{-1}$. Assuming one proton per relativistic electron (e.g., (106), (16)), the total kinetic energy in the jet is $L_{kin} = 8.02 \times 10^{47}\ erg\ s^{-1}$ and $L_{kin} = 1.35 \times 10^{47}\ erg\ s^{-1}$ for January and April, respectively. The maximum γ-ray flux during the period of high activity is $(2.22 \pm 0.38) \times 10^{-6}\ photon\ cm^{-2} s^{-1}$ which corresponds to an isotropic γ-ray luminosity of $L_\gamma = 1.22 \times 10^{49}\ erg\ s^{-1}$ (using a distance of $d_L \approx 6112.8\ Mpc$). Likewise, the γ-ray luminosities in the periods of January and April were $L_\gamma = 3.48 \times 10^{48}\ erg\ s^{-1}$ and $L_\gamma = 5.21 \times 10^{48}\ erg\ s^{-1}$, respectively. Yet, at $\delta = 18$ the total power emitted in the γ-ray band in the proper frame of the jet would be $L_{em,\gamma} = {}^{L_\gamma}/_{2\,\delta^2} = 1.89 \times 10^{46}\ erg\ s^{-1}$ during the peak flux and would change within $L_{em,\gamma} = (5.38 - 8.04) \times 10^{45}\ erg\ s^{-1}$ in January and April. These luminosity values account for only a small fraction ($\leq 6.7\%$) of the total kinetic energy of the jet. However, assuming that the standard radiative efficiency of the accretion disk η_{disk}~10%, the accretion power would be $L_{acc} = 2 \times 10^{46}\ erg\ s^{-1}$. Thus during the flaring period the power emitted as γ-ray photons constitutes the bulk of the total accretion power $L_{em,\gamma}/L_{acc} \approx 1$, while in January and April it made a substantial fraction of it - $L_{em,\gamma}/L_{acc} \approx (0.3 - 0.4)$; this is in a good agreement with the recent results by (107), which showed that the radiative jet power in blazars is higher than (or of the order of) the accretion disk luminosity.

The observations in both X-ray and γ-ray bands show that after the activity observed in January and April the emission from the source again enters a quiescent state. A small increase in the γ-ray flux has been observed only in June, August and October-November 2015. Also, the UV/X-ray flux measured by Swift in May 2015 (85) shows that the synchrotron component is weaker than it was in April. Thus, this indicates that the magnetic field in the emitting region started to decrease. In addition, in the γ-ray band, the flux slowly decreases down to a few times $10^{-7}\ photon\ cm^{-2} s^{-1}$ for most of the time after August 2015, and the γ-ray photon index reaches its mean level. These point out that the emission from the blob outside the BLR region weakened, and the decrease of the

Compton component shows that the emission responsible for the emission in the quiescent state (SSC) starts to dominate again. Since in this case the emission occurs close to the central source, due to the strong absorption, it is not expected to have emission of VHE γ-ray photons.

The multiwavelength observations of PKS 1441+25 during the flaring periods allowed us to investigate and discuss the changes that possibly took place in the jets and caused flaring activities. However, the parameters describing the underlying electron distribution below the break are poorly constrained, because the data describing the rising part of both low and HE components are missing. It did not allow us to exactly identify the processes responsible for the acceleration of particles in the jet. However, the future possible observations of flaring periods also in other energy bands will provide a chance to investigate the dominant particle acceleration processes.

Chapter 5

5. On the multi-wavelength Emission from CTA 102

The modeling of blazar SEDs in quiescent and flaring states enables to understand the physical processes responsible for the emission. However, considering only the seven FSRQs detected in VHE γ-ray band we are limited for detailed investigation of the emission processes. Since the data only for observation in short periods are available and sometimes they are not simultaneous. Therefore, studying the emission only from FSRQs detected in the VHE γ-ray band does not allow to investigate the radiative output of emitting region while it moves along the jet. In order to study the emission produced from different zones of the jet we investigated the emission from well know blazar CTA 102. This source was selected since it is continuously monitored in various energy bands which provides huge amount of data allowing to study not only temporal correlation of emission in various bands but also model SEDs with simultaneous data observed in various periods. CTA 102 is a distant HE γ-ray emitting blazar ($z = 1.037$) detected but due to its distant most likely it cannot be observed in the VHE γ-ray band due to EBL strong absorption. For this blazar the large amount of data in radio, optical, X-ray and γ-ray bands are available, which enable to investigate the physical processes in both quiescent and active states of the jet, as well as distinguish the emission regions along the jet in different active periods.

5.1. Introduction

The blazars are the most extreme class of radio-loud AGNs and they are dominant sources in the extragalactic γ-ray sky. After the lunch of Fermi Large Area Telescope (*Fermi* LAT) several thousand blazars were detected in the γ-ray band (104) which opens new perspectives for investigation of the broadband emission from them. The observations indirectly show that the γ-rays can be produced either close to or far from the central black hole. As the γ-ray emission regions are very compact, inferred from extreme short time scale variabilities (e.g., in minute scales (108) (109) (18) (110) (111) (112) (19) (113)) and that

there is a sharp break in the GeV γ-ray spectra of some blazars (84), the emission is most likely produced within the BLR. On the other hand, the recent detection of $\geq 100\ GeV$ photons from several FSRQs (86), (68) (17) (97) implies that the γ-ray emission region should most likely be beyond the BLR in order to bypass strong absorption of VHE photons (84) (83). Unfortunately, the angular resolution of γ-ray instruments is not high enough (and will not be in the near future) to resolve and localize the γ-ray emission regions which makes it difficult to determine the exact origin of γ-ray emission from blazars as the jet dissipation can occur at any distance from the central black hole.

Among the FSRQs detected by *Fermi* LAT, the powerful GeV γ-ray emitter CTA 102, $z = 1.037$ (114), is flaring frequently, its γ-ray flux sometimes exceeding $10^{-5}\ photon\ cm^{-2}\ s^{-1}$. CTA 102 is a luminous, well-studied highly polarized quasar (115) having variable optical emission (116). It has been initially identified by Compton Gamma Ray Observatory mission as a γ-ray emitter (the flux $> 100\ MeV$ being $(2.4 \pm 0.5) \times 10^{-7}\ photon\ cm^{-2}s^{-1}$, and then it is being included in all the point source catalogs of *Fermi* LAT (95). Since 2016, CTA 102 was in the enhanced emission state in the UV/optical, X-ray and HE γ-ray bands (117) (118) (119) (120) (121) (122) (123) (124) (125) (126) with several prominent γ-ray bright periods. Considering the available large amount of multiwavelength data which allows to constrain the emitting region size and location, magnetic field and electron energy distribution, etc., CTA 102 is an ideal object for exploring the physics of FSRQ jets.

5.2. Observations and Data Reduction

5.2.1. γ-ray observations: Fermi LAT

For the present study we use the publicly available *Fermi* LAT data acquired in the period from 01 January 2016 to 09 January 2018 when large-amplitude flares of CTA 102 were observed. Fermi Science Tools v10r0p5 was used to analyze the data with *P8R2_SOURCE_V6* instrument response function. Only the 100 MeV - 300 GeV events extracted from a 12° region of interest (ROI) centered on the location of CTA 102 $[(RA, dec) = (338.139, 11.720)]$ have been analyzed. However, the results were checked by

repeating the same analyses selecting ROI radii of 10° and 15°. To eliminate the Earth limb events, the recommended quality cuts, $(DATA\_QUAL == 1)$ && $(LAT\_CONFIG == 1)$ and a zenith angle cut at 90° were applied. After binning the data into pixels of $0.1^{\circ} \times 0.1^{\circ}$ and into 34 equal logarithmically-spaced energy bins, with the help of *gtlike* a binned likelihood analysis is performed. The model file describing ROI was created using the *Fermi* LAT third source catalog (95) (3FGL) which contains sources within ROI+5° from the target, as well as Galactic *gll_iem_v06* and *iso_P8R2_SOURCE_V6_v06* diffuse components.

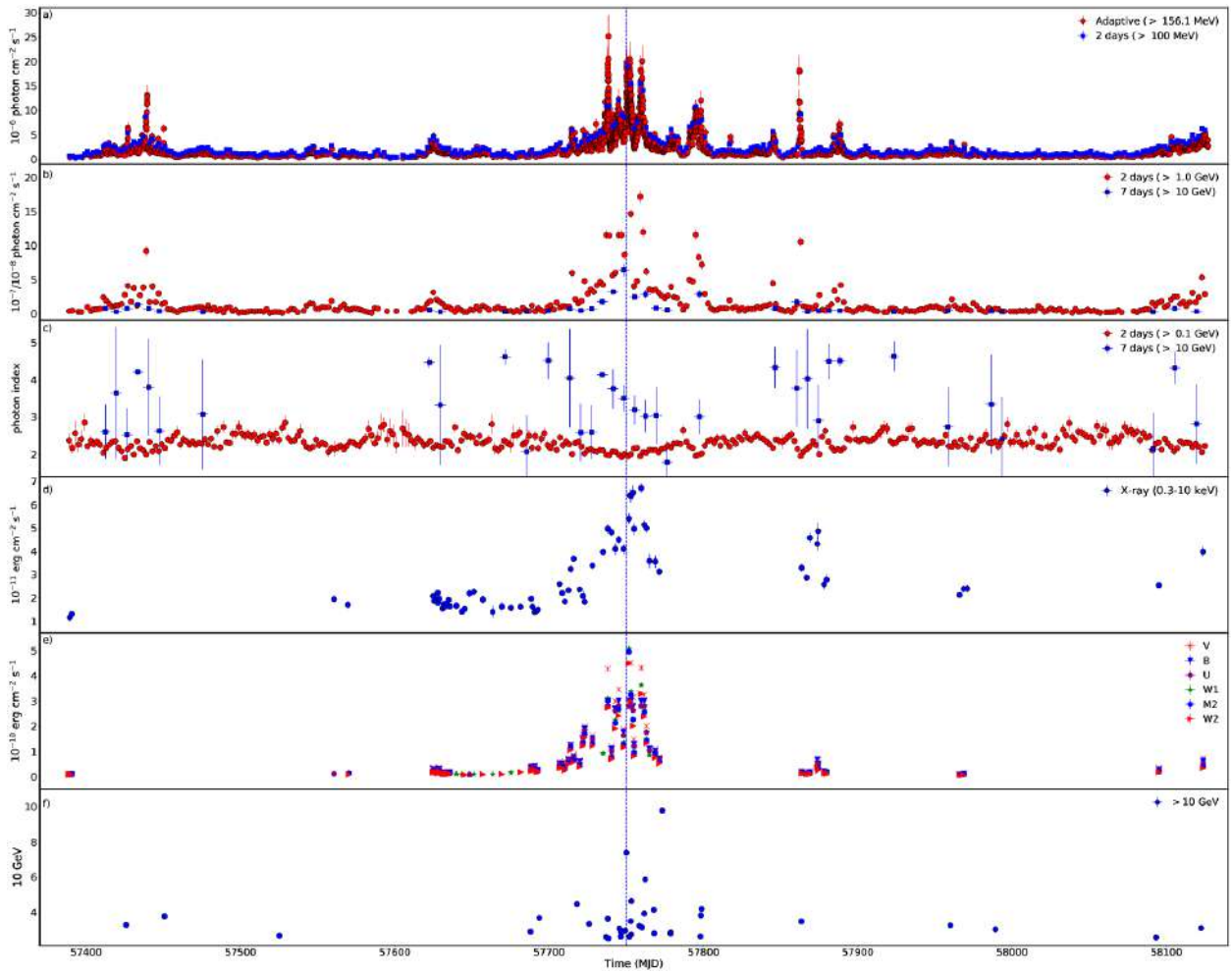

Figure 5.1. Multifrequency light curve of CTA 102 obtained for the period from 2008 August to 2018 January. *a)* γ-ray light curves with adaptive (red; $\geq 156.1\, MeV$) and 2-day (blue; $100\, MeV$) bins, *b)* and *c)* the flux and photon index with 2- and 7-days binning, *d)* Swift XRT light curve in the $0.3 - 10\, keV$ range, *e)* UV/optical fluxes in V, B, U, $W1$, $M2$ and $W2$ bands and *f)* the energy and arrival times of the highest-energy photons. The vertical blue dashed line shows the period when a large flare in the R- band was observed (28 December 2016).

All point-source spectra were modeled with those given in the catalog, allowing the photon index and normalization of the sources within 12° to be free in the analysis. Also, the normalization of diffuse background components are free. To check if there are new γ-ray sources in the ROI, a Test Statistics (TS) map (TS defined as $TS = 2(logL - logL_0)$, where L and L_0 are the likelihoods whether or not the source is included) is created with *gttsmap* tool which places a point source at each pixel and evaluates its TS. In the TS map, there are new hotspots (pixels) with $TS > 25\,(5\,\sigma)$ which possibly hints at the presence of new sources. For each new hotspot we sequentially added a new point source with a power-law spectral definition. For the further analysis the model file containing these additional point sources is used.

In the whole-time analysis, the γ-ray spectrum of CTA 102 was first modeled using a log-parabola (127) as in 3FGL and then assuming a power-law shape. The latter will be used in the light curve calculations, as shorter periods will be considered and a power law can be a good approximation of the spectrum. During the analysis of each individual flare a different model file obtained from the analyses of the data accumulated during one/two- month periods covering the flares was also used. An unbinned maximum likelihood analysis was performed using $(0.1 - 300)\ GeV$ photons with the appropriate quality cuts mentioned above, to obtain the γ-ray light curves. Since no variability is expected from the underlying background diffuse emission, we fix the normalization of both background components to the best fit values obtained for the whole time period.

Initially, the light curve was calculated with the help of an adaptive binning method. At regular (fixed) time binning, the long bins will smooth out the fast variation while short bins might result in many upper limits during the low-activity periods. In the adaptive binning method, the time bin widths are adjusted to produce bins with constant flux uncertainty above the optimal energies (96) meant to find rapid changes in γ-ray fluxes. The adaptively binned light curve with 15% uncertainty and above $E_0 = 156.1\ MeV$ in fig. 5.1 shows several bright γ-ray states: from MJD 57420 to MJD 57445 and from MJD 57700 to MJD 57900. The peak flux of $(2.52 \pm 0.42) \times 10^{-5}\ photon\ cm^{-2}s^{-1}$ with a photon index of $\Gamma = 1.99 \pm 0.15$ was observed on MJD 57738.47 within 4.31 minutes with a convincingly

high $\sim 20.0\,\sigma$. It corresponds to a flux of $(3.55 \pm 0.55) \times 10^{-5}\ photon\ cm^{-2} s^{-1}$ above $100\,MeV$ which ~ 221 times exceeds the average γ-ray flux given in 3FGL ($\approx 1.60 \times 10^{-7}$ $photon\ cm^{-2}\,s^{-1}$ but the source is variable with a variability index of 1602.3 in 3FGL). In addition, we used *gtfindsrc* tool to determine the best coordinates of the γ-ray emission in this period, yielding $(RA, dec) = (338.115, 11.746)$ with a 95% confidence error circle radius of $r_{95} = 0.06$. These coordinates are offset only by 0.03° from the γ-ray position of CTA 102, indicating that it is the most likely source of the emission. The hardest photon index of 1.61 ± 0.10 $(22.56\,\sigma)$ was observed on MJD 57752.45 within $9.46\ minutes$, which is significantly harder than the mean photon index observed during the considered period, $\Gamma_{mean} = 2.22$.

In the adaptively binned light curve there is a hint at flux changes in minute scales. For example, the interval of MJD 57737.88- MJD 57739.00 ($\sim 1.13\ days$), contains 67 adaptive bins each having a width of the order of a few minutes and a detection significance of $> 14.3\sigma$. Another such active period was observed on MJD 57752.0, though the time bin widths were a few tens of minute. Many times during the considered period, the source flux exceeded $10^{-5}\ photon\ cm^{-2}\,s^{-1}$, mostly observed during the extremely active period from MJD 57736.4 to MJD 57798.46 as well as a few times on MJD 57439.0 and MJD 57862.0. During these periods, the photon flux and index vary within $(1.01 - 2.52) \times 10^{-5}\ photon\ cm^{-2}\,s^{-1}$ and $1.61 - 2.56$, respectively, the minimum and maximum bin widths being 4.31 and 194.54 minutes and the detection significance varying from 13.18σ to 22.61σ.

fig. 5.1 b) shows the γ-ray light curve $> 1\ GeV$ (2 days; red color) and $> 10\ GeV$ (7 days; blue color) with a noticeable increase in the flux, the peaks being $(2.32 \pm 0.10) \times 10^{-6}$ $photon\ cm^{-2}\,s^{-1}$ and $(6.43 \pm 0.94) \times 10^{-8}\ photon\ cm^{-2}\,s^{-1}$, at 2-day and 7-day binning, respectively. Above 10 GeV, among 105 total bins only in 36 the detection significance is at least 4σ, but, e.g., on MJD 57741.0 and MJD 57748.0 it is as large as $\approx 29\sigma$, N_{pred} varying within 46-55.

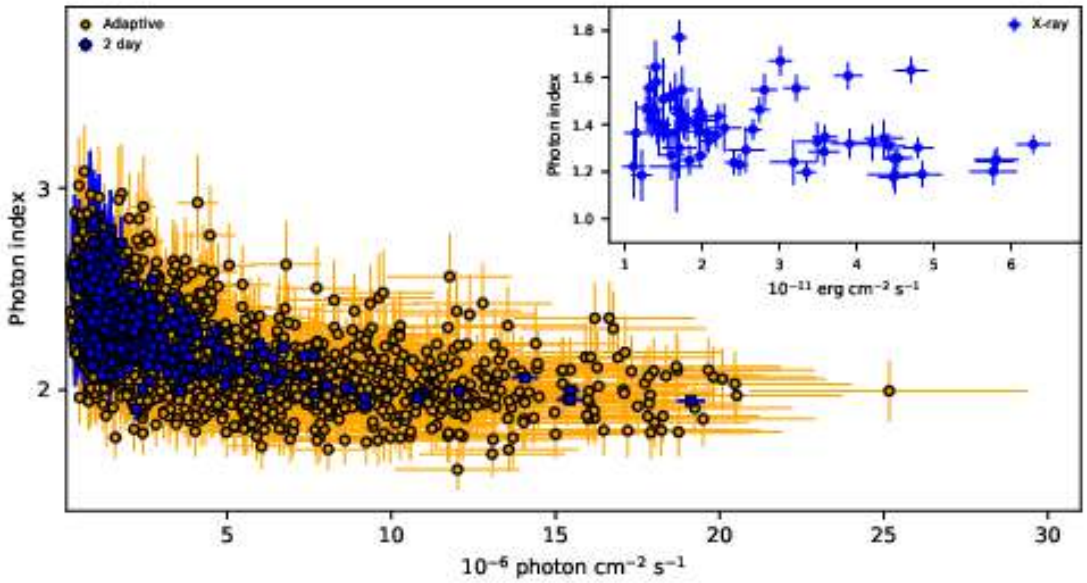

Figure 5.2. CTA 102 γ-ray photon index vs. flux in adaptive (orange) and two-day bins (blue). Similar plot for the X-ray band is shown in the insert.

The γ-ray photon index variation above 0.1 and 10 GeV is shown in the fig. 5.1 c) with red and blue colors, respectively. There is an obvious hardening above $0.1\,GeV$, when the photon index changed to $\Gamma \approx 2.0$, during the most bright periods of the source. The mean γ-ray photon index above $10\,GeV$ is $\Gamma_{mean} = 3.41$ but on MJD 57776.0 $\Gamma = 1.79 \pm 0.55$ with 7.85σ.

The γ-ray photon index versus flux is presented in fig. 5.2 for adaptive (orange) and 2-day binning (blue; $> 0.1\ GeV$). When 2-day intervals are considered, there is a hint of spectral hardening as the source gets brighter. In the γ-ray band such behavior has been already observed from several blazars (e.g., PKS 1502+106 (128), PKS 1510-089 (101), sometimes from 3C 454.3 (129), etc.) and radio galaxies (e.g., NGC 1275 (130)). Such evolution of spectral index and flux is expectable when accelerated HE electrons are cooled down (e.g., (34)). It is hard to see similar relation in the case of adaptive bins as the bright periods last shorter, leading to larger uncertainties. The linear-Pearson correlation test applied to 2-day and adaptively binned intervals yielded $r_p = -0.569$ and $r_p = -0.533$, respectively, the p-value being $<< 10^{-5}$. This suggests negative correlation between the flux and photon index, i.e., as the flux increases, the photon index decreases (hardens).

The distribution of highest energy events ($> 10\ GeV$) detected from CTA 102, calculated

using the *gtsrcprob* tool is presented in fig. 5.1 f). Most of the HE photons are observed during MJD 57700-57800 with the maximum of $97.93\ GeV$ detected on MJD 57773.34.

5.2.2. Swift UVOT/XRT observations

The data from seventy Swift (Neil Gehrels Swift observatory) observations of CTA 102 carried out from 01 January 2016 to 09 January 2018 have been analyzed. The exposures range from 0.3 ks (ObsID:33509083) to 3.14 ks (ObsID:33509095) and most of the observations were made in the photon counting and only two in the window timing mode. The XRT data were analyzed with *XRTDAS* (v.3.3.0) using standard procedure and the most recent calibration databases. Events for the spectral analysis were selected within a 20 pixel ($47''$) circle with the source at the center, while the background region as an annulus with the same center and having inner and outer radii of 51 ($120''$) and 85 pixels ($200''$), respectively. The count rate in some observations was above $0.5\ count\ s^{-1}$ implying pile-up in the inner part of the PSF. This effect was removed by excluding the events within a 3 pixel radius circle centered on the source position. The Cash statistics (131) on ungrouped data was used as for some observations the number of counts was low. However for the observations with a high count rate, the results were also cross-checked by re-binning to have at least 20 counts per bin and then fitted using the χ^2 minimization technique. The individual spectra were fitted with *XSPEC* v12.9.1a adopting an absorbed power-law model with $N_H = 5.35 \times 10^{20}\ cm^{-2}$ column density, ignoring the channels with energy below $0.3\ keV$ and above $10\ keV$. fig. 5.1 d) shows the X-ray flux evolution in time (the corresponding parameters are presented in Table 5.1, where its gradual increase contemporaneous with the γ-ray flux around MJD 57750 can be seen. The highest flux of $F_{0.3-10\ keV} \approx (6.71 \pm 0.21) \times 10^{-11}\ erg\ cm^{-2}s^{-1}$ observed on MJD 57759.69 exceeds the average flux ($\approx 1.2 \times 10^{-11}\ erg\ cm^{-2}s^{-1}$) ~5.6 times. A relation between the unabsorbed X-ray flux and photon index is represented in the insert of fig. 5.2. A trend of a harder spectrum when the source is brighter can be seen. Such harder-when-brighter trend in the X-ray band was already observed from several FSRQs (e.g., PKS 1510-089 (132) (133), 3C

454.3 (134) and etc.) which can be described if assuming the electrons are losing energy mainly through interaction with the external photon fields (e.g. (135)).

The data from the second instrument on board the Swift satellite, UVOT, was used to measure the flux of the source in the UV/optical bands. Photometry was computed using a five-arcsecond source region around CTA 102 and for the background - a source-free annulus centered on the source position with $27''$ inner and $35''$ outer radii. The magnitudes were computed using *UVOTSOURCE* task, then corrected for extinction, using the reddening coefficient $E(B-V)$ from (136) and the ratios of the extinction to reddening A/E(B-V) for each filter from (137) then converting to fluxes, following (138). The flux measured for $V, B, U, W1, M2$ and $W2$ filters is shown in fig. 5.1 e). Even if the available data are not enough for detailed studies, it is clear that up to ~ MJD 57720 the source was in a relatively faint state in the optical/UV band but its flux significantly increased during the bright flaring period around ~ MJD 57750. This is in agreement with the recent results by (139) which show that the source emission in the optical band increased in late 2016 with a 6-7 magnitude jump as compared with the minimal state. The maximum flux in the $R-$ band was observed on 28 December 2016 (MJD 57750) with a peak luminosity of $1.32 \times 10^{48}\ erg\ s^{-1}$. In addition, the radio monitoring (at $37\ GHz$) showed that the peak in this band is much earlier than the one in the $R-$band, inferring these emissions were produced in different locations of the jet.

5.2.3. NuSTAR observation

In the hard X-ray band ($3-79\ keV$), CTA 102 was observed once on 30 December 2016 by NuSTAR with a net exposure of $\sim 26.21\ ks$, when it was bright in the X-ray and γ-ray bands. The raw data (from both Focal Plane Modules [FPMA and FPMB; (140)] were processed with the NuSTAR Data Analysis Software (*NuSTARDAS*) package v.1.4.1 (via the script *nupipeline*), producing calibrated and cleaned event files. The events data were extracted from a region of $75''$ centered on the source position, while the background was extracted from a nearby source free circular region with the same radius. The spectra were binned so to have at least 30 counts per bin and fitted assuming an absorbed power-law

model. The best fit resulted in $\Gamma_x = 1.32 \pm 0.005$ and $\Gamma_{3-79\,keV} \approx (2.94 \pm 0.02) \times 10^{-10}\ erg\ cm^{-2}s^{-1}$ with $\chi^2 = 0.97$ for 1131 degrees of freedom. The corresponding spectra for FPMA and FPMB are shown in fig. 5.3.

Table 5.1. Summary of Swift XRT observations of CTA 102.

Sequence No.	Date (MJD)	Exp(sec)	Log(Flux)[a]	Γ	C-stat./dof
00033509016	2016-01-02(57389.33)	834.1	10.94±0.06	1.23±0.14	91.23(103)
00033509017	2016-01-03(57390.6)	1119.0	10.88±0.04	1.18±0.10	166.99(168)
00033509018	2016-06-21(57560.67)	991.4	10.71±0.03	1.43±0.08	218.22(218)
00033509021	2016-06-30(57569.66)	844.1	10.77±0.04	1.42±0.11	195.86(151)
00033509022	2016-08-24(57624.88)	1633.0	10.68±0.02	1.38±0.06	422.02(320)
00033509023	2016-08-25(57625.35)	1691.0	10.73±0.02	1.46±0.06	393.49(306)
00033509024	2016-08-26(57626.94)	1868.0	10.71±0.02	1.41±0.06	410.73(323)
00033509025	2016-08-27(57627.94)	1466.0	10.65±0.03	1.43±0.07	233.39(291)
00033509026	2016-08-28(57628.01)	2148.0	10.75±0.02	1.45±0.06	271.35(309)
00033509027	2016-08-28(57628.94)	2797.0	10.71±0.02	1.36±0.05	450.67(403)
00033509028	2016-08-30(57630.93)	1576.0	10.81±0.03	1.48±0.07	226.96(270)
00033509030	2016-08-31(57631.93)	2133.0	10.76±0.03	1.35±0.07	289.41(290)
00033509031	2016-09-02(57633.06)	1978.0	10.78±0.02	1.42±0.06	316.53(301)
00033509034	2016-09-03(57634.79)	966.5	10.72±0.03	1.57±0.09	220.83(194)
00033509035	2016-09-04(57635.64)	869.1	10.79±0.03	1.64±0.09	207.90(193)
00033509076	2016-09-02(57633.92)	1965.0	10.75±0.02	1.47±0.06	373.93(324)
00033509077	2016-09-08(57639.9)	991.4	10.78±0.04	1.33±0.10	202.35(178)
00033509078	2016-09-12(57643.43)	914.0	10.85±0.04	1.47±0.10	160.64(171)
00033509079	2016-09-14(57645.36)	1091.0	10.81±0.03	1.4±0.09	192.03(199)
00033509080	2016-09-17(57648.47)	894.0	10.66±0.03	1.34±0.08	262.16(217)
00033509081	2016-09-20(57651.32)	996.4	10.64±0.03	1.33±0.07	311.96(242)
00033509082	2016-09-26(57657.11)	789.1	10.72±0.04	1.43±0.09	198.62(189)
00033509083	2016-10-02(57663.43)	344.6	10.85±0.07	1.37±0.20	47.08(67)
00033509084	2016-10-08(57669.34)	609.3	10.79±0.05	1.45±0.12	130.49(103)
00033509085	2016-10-14(57675.33)	966.5	10.8±0.04	1.38±0.10	221.53(186)
00033509086	2016-10-20(57681.43)	971.4	10.79±0.04	1.32±0.09	248.18(190)
00033509087	2016-10-27(57688.54)	1965.0	10.71±0.02	1.29±0.06	449.38(329)
00033509088	2016-10-28(57689.21)	1711.0	10.79±0.03	1.36±0.07	301.62(271)
00033509090	2016-10-29(57690.59)	1723.0	10.85±0.03	1.46±0.08	182.50(224)
00033509091	2016-10-30(57691.92)	1656.0	10.84±0.03	1.4±0.08	231.46(241)
00033509092	2016-10-31(57692.79)	2108.0	10.82±0.02	1.57±0.06	287.31(299)
00033509093	2016-11-14(57706.68)	2974.0	10.59±0.02	1.22±0.04	597.15(447)
00033509094	2016-11-16(57708.53)	2762.0	10.66±0.02	1.25±0.05	460.61(428)
00033509095	2016-11-18(57710.26)	3137.0	10.73±0.02	1.33±0.05	432.80(415)
00033509096	2016-11-20(57712.58)	2435.0	10.63±0.02	1.32±0.05	556.82(417)
00033509097	2016-11-22(57714.11)	1693.0	10.49±0.02	1.55±0.06	265.95(322)
00033509098	2016-11-23(57715.9)	2934.0	10.43±0.02	1.19±0.04	717.13(517)
00033509099	2016-11-27(57719.78)	1963.0	10.63±0.02	1.36±0.05	505.78(364)
00033509100	2016-11-30(57722.02)	382.1	10.68±0.05	1.42±0.12	108.37(118)
00033509101	2016-12-01(57723.08)	1341.0	10.74±0.02	1.78±0.07	278.11(275)
00033509103	2016-12-06(57728.07)	1958.0	10.47±0.02	1.69±0.05	449.08(354)
00033509105	2016-12-13(57735.06)	2655.0	10.40±0.02	1.32±0.04	457.45(437)

Table 5.1 (continued)

00033509106	2016-12-16(57738.05)	2440.0	10.30±0.02	1.23±0.04	653.22(469)
00033509107	2016-12-18(57740.49)	2402.0	10.32±0.02	1.27±0.05	569.51(541)
00033509108	2016-12-20(57742.95)	818.4	10.39±0.03	1.47±0.08	271.95(359)
00033509109	2016-12-23(57745.07)	1993.0	10.35±0.02	1.58±0.05	399.45(388)
00033509110	2016-12-26(57748.33)	1686.0	10.39±0.02	1.39±0.06	347.1(329)
00033509111	2016-12-29(57751.8)	1823.0	10.27±0.02	1.62±0.04	55.60(397)
00033509112	2016-12-30(57752.54)	1468.0	10.19±0.02	1.29±0.05	82.04(410)
00088026001	2016-12-31(57753.06)	2048.0	10.20±0.02	1.26±0.04	19.50(486)
00033509113	2017-01-02(57755.05)	1566.0	10.30±0.02	1.24±0.05	83.85(386)
00033509114	2017-01-01(57754.37)	1488.0	10.19±0.02	1.18±0.05	05.54(421)
00033509115	2017-01-06(57759.69)	2472.0	10.17±0.01	1.33±0.03	48.83(539)
00033509116	2017-01-08(57761.68)	2480.0	10.29±0.02	1.31±0.04	07.41(465)
00033509117	2017-01-10(57763.14)	2502.0	10.30±0.02	1.17±0.04	07.92(463)
00033509118	2017-01-12(57765.07)	521.9	10.45±0.04	1.19±0.09	00.60(200)
00033509119	2017-01-15(57768.86)	1009.0	10.45±0.03	1.33±0.08	54.30(243)
00033509120	2017-01-18(57771.38)	1768.0	10.50±0.02	1.41±0.05	99.09(391)
00033509121	2017-04-20(57863.68)	1975.0	10.48±0.02	1.56±0.06	42.39(331)
00033509122	2017-04-23(57866.86)	2273.0	10.54±0.02	1.38±0.05	67.86(419)
00033509123	2017-04-26(57869.13)	2018.0	10.34±0.02	1.33±0.05	94.03(383)
00033509124	2017-04-30(57873.83)	991.4	10.36±0.03	1.34±0.07	98.45(263)
00033509125	2017-05-01(57874.31)	891.5	10.31±0.03	1.16±0.08	07.36(245)
00033509126	2017-05-05(57878.23)	681.8	10.59±0.04	1.41±0.09	03.60(192)
00033509127	2017-05-06(57879.75)	529.4	10.56±0.04	1.33±0.09	05.28(182)
00033509128	2017-08-01(57966.04)	1975.0	10.67±0.02	1.45±0.05	27.29(342)
00033509129	2017-08-03(57968.65)	2298.0	10.62±0.02	1.42±0.05	57.95(394)
00033509131	2018-01-05(58123.69)	1970.0	10.4±0.02	1.27±0.06	97.65(354)
00033509130	2017-08-05(57970.96)	876.5	10.62±0.03	1.41±0.08	70.04(241)
00033509061	2017-12-08(58095.17)	2477.0	10.59±0.02	1.25±0.05	444.7(416)

[a] Flux in $0.3-10keV$ in unit of $erg\ cm^{-2}\ s^{-1}$

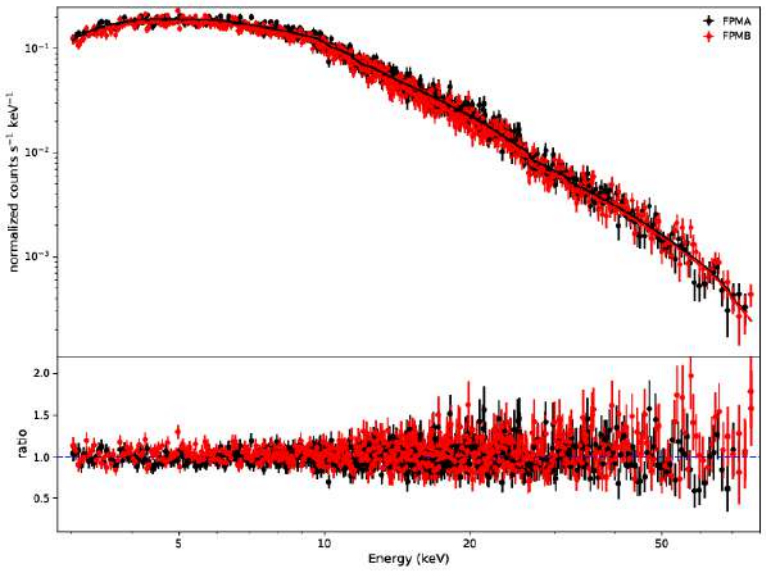

Figure 5.3. Top: NuSTAR FPMA (black) and FPMB (red) spectra and best-fit models. *Bottom:* Residuals with respect to power-law model.

5.2.4. The light curves variability

Table 5.2. Parameter values best explaining the flares

Flare period t_0 MJD	$t_r \pm err$ (day)	$t_d \pm err$ (day)	$F_0/10^{-6}$ $photon\ cm^{-2}s^{-1}$
57736.53±0.11 [a]	0.46 ±0.13	0.17 ±0.08	18.68 ±3.33
57738.50±0.06 [a]	0.60 ±0.09	0.21±0.03	29.04±2.39
57845.78±0.36 [b]	1.49±0.33	0.70±0.23	9.72±1.26
57862.02±0.11 [b]	0.17±0.06	0.73±0.11	25.20±2.63

The γ-ray (2-day (> 0.1 and $> 1.0\ GeV$), 7-day ($> 10.0\ GeV$) and adaptive binned ($> 156.1\ MeV$)), X-ray ($0.3 - 10\ keV$) and UV/optical fluxes variation in time are shown in the a), b), c), d) and e) panels of fig. 5.1. There is an evident major γ-ray flux increase accompanied by moderate brightening in the X-ray and UV/optical bands. The variability in different bands is quantified using their fractional rms variability (F_{var}) amplitude (141), resulting in $F_{var} = 0.511 \pm 0.008$ for X-ray band and correspondingly 0.920 ± 0.006 and 0.984 ± 0.004 for the γ-ray light curves with adaptive and 2-day ($> 0.1\ GeV$) binning, implying much stronger variability in the γ-ray band. This variability is even stronger when the light curves with 2-day ($> 1.0\ GeV$) and 7-day ($10.0\ GeV$) bins are used (excluding correspondingly 20 and 69 periods with upper limits in them), since $F_{var} = 1.61 \pm 0.01$ and 1.18 ± 0.06, respectively.

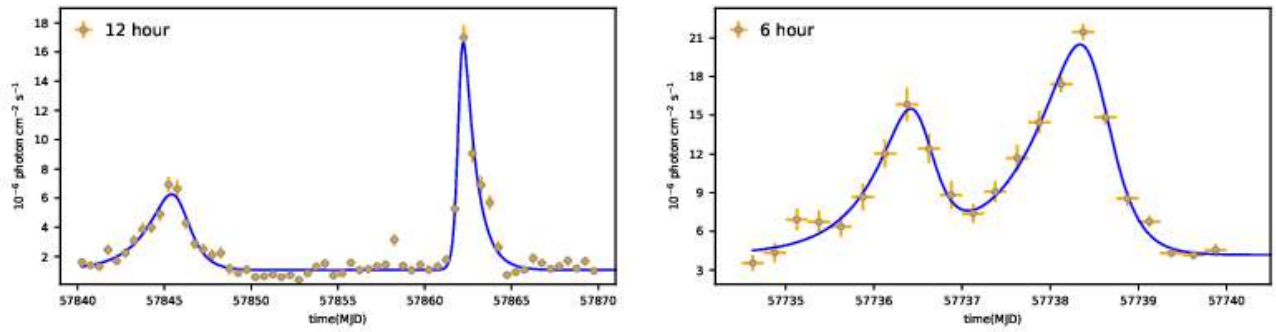

Figure 5.4. Light curves of CTA 102 above 100 MeV with time binning of **6 *h*** (upper panel) and **12 *h*** (lower panel). The lines show the flare fit with Eq. 5.1 (Table 5.2).

The rapid variability in the γ-ray band can be further investigated by fitting the data with the double exponential form function to obtain the time profiles of the flux variations.

However, we note that the double exponential form function is not unique and the flare time profiles can be reproduced also by other functions (e.g., see (142)). As the main purpose of the current fit is only to estimate the rise and decay times, we fit the light curves with the following function (98):

$$F(t) = F_c + F_0 \times \left(e^{\frac{t-t_0}{t_r}} + e^{\frac{t_0-t}{t_d}} \right)^{-1}, \tag{5.1}$$

where t_0 is the time of the flare peak (F_0) and t_r and t_d are the rise and decay times, respectively. Each light curve was fitted with the non-linear optimization python package *lmfit* (143) using a function that contains two inverses of the sum of exponentials (corresponding to the number of flares).

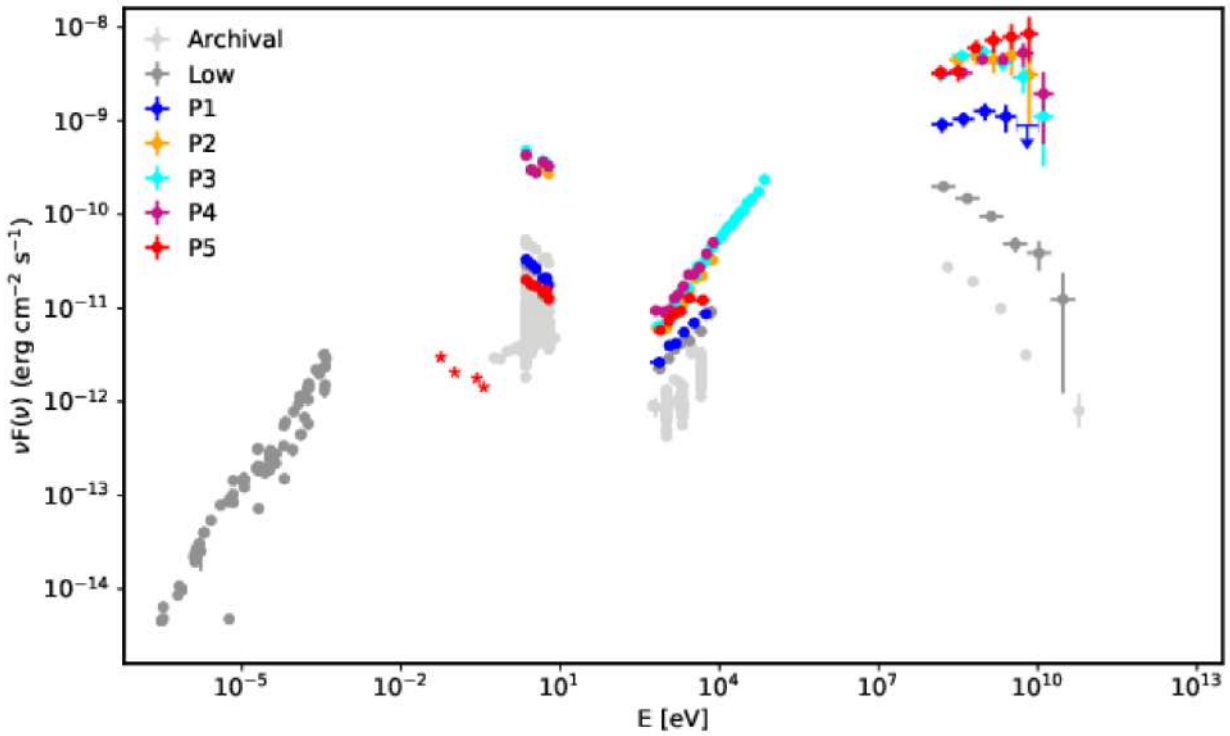

Figure 5.5. The broadband SEDs of CTA 102 in the selected periods. The archival data are shown in light gray.

The active (bright) periods identified in the adaptively binned light curve are analyzed with normal time sampling and only the periods when the rise and decay times can be well constrained are considered. Accordingly, the periods from MJD 57734 to MJD 57740 and from MJD 57840 to MJD 57870 (fig. 5.4) divided into 6- and 12 hour bins respectively are

selected; the detection significance in each bin is $> 5\sigma$ and the plot of $N_{pred}/\sqrt{N_{pred}}$ vs $Flux/\Delta Flux$ shows linear correlation, so the likelihood fit converged for each time bins. The identified four peaks are sequentially numbered from 1 to 4 (F1- F4).

The fit is shown in fig. 5.4 and the corresponding parameters are given in Table 5.2. The average flux level (F_c) is left free during the fitting and the corresponding values are presented in Table 5.2. The flares 1-3 have rise times longer than the fall, and only F4 shows the opposite tendency. The symmetry of the flares can be quantitatively estimated by calculating the parameter of $\varepsilon = (t_d - t_r)/(t_d + t_r)$ as defined in (98) which ranges from -0.64 to -0.46 for F1-3 and 0.62 for F4, implying these are moderately asymmetric flares. The shortest e-folding times for rise and decay are $t_r = 0.17 \pm 0.06$ and $t_d = 0.21 \pm 0.03$ day[1] observed during F2 and F4, respectively. During F4, when the highest flux was observed within 4.08 ± 1.44 hours, the flux increased up to $(2.52 \pm 0.26) \times 10^{-5}$ $photon\ cm^{-2}\ s^{-1}$ and dropped to its average level within 17.52 ± 2.64 $hour$.

5.3. Spectral evolution

A "Light curve/SED movie" is made for a better understanding of the spectral evolution in different bands. For each adaptively binned interval, using the estimated photon index and flux, the γ-ray spectra are calculated by dividing the $(0.16 - 300)$ GeV interval into five logarithmically equal bins. These γ-ray spectra are combined with the UV/optical/X-ray (if available) data to make SEDs. As moving from bin to bin, the spectra in all bands can be compared and their evolution in time seen.

The movie is uploaded here (144), where the time period from MJD 57620 to MJD 57950 coinciding with the most active γ-ray emitting state is presented. Up to $\approx$ MJD 57730, the emission from the source had a soft photon index $\Gamma \geq 2.0$ and a maximum flux around $\approx 10^{-10}$ $erg\ cm^{-2}s^{-1}$, which afterwards exceeded 10^{-9} $erg\ cm^{-2}s^{-1}$ with hard γ-ray photon indices. Starting from MJD 57765, the flux dropped to its original level and the γ-ray photon index softened. Around MJD 57800, when the flux increased again, the photon indices were $\Gamma \approx 2.0$, implying a flat spectrum of the source in $(\nu - \nu F_\nu)$

[1] in Table 5.2 e-folding times are given, the doubling or halving timescales can be computed by $t_{r,d} \times ln2$

representation. These spectral evolutions once more confirm a harder-when-brighter trend.

5.3.1. Spectral analysis

The data from the following periods are considered for the spectral analyses:

low state (when the source was not flaring in the γ-ray band): when X-ray and γ-ray fluxes were in their average levels: from Swift observations, Obsid: 33509078, 33509079, 33509085, 33509086 and 33509091 were analyzed by merging them to increase the exposure and statistics as they have similar X-ray flux and photon indices while a few intervals, when the source flux exceeded $9 \times 10^{-7} photon\ cm^{-2}\ s^{-1}$, were excluded from the contemporaneously obtained γ-ray data.

Table 5.3. Parameters of spectral analysis

Fermi LAT			
Period	Photon index[a]	Flux[b]	σ[c]
low	2.39±0.03	1.13±0.04	61.4
P1	2.01±0.09	6.34±0.72	25.0
P2	1.93±0.08	24.17±2.43	33.4
P3	1.96±0.04	24.74±1.31	56.5
P4	1.93±0.05	21.72±1.40	48.7
P5	1.81±0.08	25.14±2.65	31.0
Swift-XRT			
Period	Photon index[d]	Unabsorbed Flux[e]	χ^2_{red} (d.o.f.)
low	1.44±0.05	1.45±0.07	1.10(39)
P1	1.41±0.05	1.91±0.09	0.77(52)
P2	1.23±0.05	4.79±0.22	0.97(53)
P3	1.25±0.04	5.75±0.13	1.26(84)
P4	1.32±0.04	6.46±0.15	1.20(75)
P5	1.56±0.06	3.31±0.15	0.91(31)
NuSTAR			
P4[f]	1.32±0.005	29.36±0.20	0.97(1131)

[a] γ-ray photon index from likelihood analysis.

[b] γ-ray flux in the $0.1 - 300\ GeV$ energy range in units of $10^{-7} photon\ cm^{-2} s^{-1}$.

[c] Detection significance.

[d] X-ray photon index.

[e] $0.3 - 10\ keV$ X-ray flux corrected for the Galactic absorption in units of $10^{-11} photon\ cm^{-2} s^{-1}$.

[f] X-ray flux and photon are measured in the energy range $3 - 79\ keV$.

This period corresponds to the pre-flaring state, allowing to investigate the source emission spectrum before the major flare.

Period 1 (P1): MJD 57625.06-57625.39 when the source was in the bright γ-ray state coinciding with XRT observations (Obsid: 33509022 and 33509023, merged during the analyses).

Period (P2): MJD 57738.02-57738.08, bright γ-ray period coinciding with the Swift Obsid: 33509106.

Period 3 (P3): $\approx 3.1\ hour$ period centered on MJD 57752.52, corresponding to a bright γ-ray state coinciding with Swift (Obsid: 33509112 and 88026001, merged) and NuSTAR observations.

Period 4 (P4): $\approx 8.06\ hour$ period centered on MJD 57759.62, corresponding to the period when the highest X-ray flux was observed (Obsid: 33509115).

Period 5 (P5): $\approx 14.66\ min$ period centered on MJD 57862.15, corresponding to another peak of γ-ray emission and available quasi-simultaneous Swift observation on the next day (Obsid: 33509121).

During the un-binned likelihood analyses of *Fermi* LAT data, the spectrum of CTA 102 has been modeled using a power-law function with the normalization and index as free parameters. Then, the SEDs are calculated by fixing the power-law index of CTA 102 and running *gtlike* separately for smaller energy bins of equal width in log scale. For the spectral analyses the Swift data were binned to have at least 20 counts per bin and then fitted using χ^2 minimization technique. Then, in order to increase the significance of individual points in the SEDs calculations, a denser re-binning was applied, restricting the energy range to $> 0.5\ keV$. The results of analyses (both X-ray and γ-ray) are given in Table 5.3 and the corresponding spectra shown in fig. 5.5.

The γ-ray emission spectra in the low state extended up to $\sim 10\ GeV$ with a soft photon index of $\Gamma = 2.39 \pm 0.03$ while it hardened during the flares, e.g., $\Gamma = 1.81 \pm 0.08$ during P5. There is an indication of deviation of the model with respect to the data above several GeV during P3 (cyan data in fig. 5.5). An alternative fit with functions in the form of $dN/dE \sim E_\gamma^{-\alpha} \times Exp(-E_\gamma/E_{cut})$ and $dN/dE \sim (E_\gamma/E_{br})^{-(\alpha+\beta\log(E_\gamma/E_{br}))}$ were applied to check

whether the curvature in the spectrum is statistically significant. The first fit resulted in $\alpha = 1.64 \pm 0.09$ and $E_{cut} = 3.84 \pm 1.21\ GeV$ which is preferred over the simple power-law modeling (comparing log likelihood ratio tests) with a significance of 4.81σ. The second fit with $\alpha = 1.58 \pm 0.10$ and $\beta = 0.21 \pm 0.05$ is preferred with a significance of 5.2σ. The breaks in the emission spectra can be expected from pair production in BLR (84) or can be related with the breaks in the emitting electron spectra (145). The possible origin of the curvature in the GeV spectra should be investigated deeper, with more detailed spectral analyses of single as well as several flaring periods, which is beyond the scope of the current paper.

5.4. Broadband SEDs

Fig. 5.5 shows the broadband SEDs of CTA 102 in its low and active periods together with the archival radio to X-ray data (light gray) from ASI science data center. The WISE IR data are highlighted by red asterisk which are most probably due to the torus emission as the recent studies show that the detection rate of almost all γ-ray blazars was high in the WISE all-sky survey (146). The comparison shows that during the considered periods the fluxes in the optical/X-ray and γ-ray bands exceed the averaged archival data: the increase is more significant in the optical/UV band. This increase in all bands is expected as the selected periods correspond to the pre-flaring, flaring and post flaring states, and the source shows different emission properties as compared with the averaged spectrum.

Comparing our selected period *i)* the low-energy component increased while its peak frequency remained relatively constant ($\leq 10^{15}\ Hz$), *ii)* the second component increased and shifted to HEs with a strong Compton peak dominance and *iii)* the UV/optical, X-ray and γ-ray fluxes contemporaneously increased in P2, P3 and P4, while the emission in the UV/optical and X-ray bands was relatively constant in P1 and P5.

The blazar flares can be explained by the changes in the magnetic field, in the emitting region size and its distance from the black hole, bulk Lorentz factor, particle energy distribution, etc. (76). For example, both emission components will be shifted to HEs when the particles are effectively re-accelerated. Only the HE component will increase when the

contribution of the external photon fields starts to dominate, for example, due to the changes in the location of the emitting region (76). However, these are not unique models for explaining the flaring events. Another possibility is the geometrical interpretation of the origin of flares, the case when the jet regions may have different viewing angles. Such a model with a twisted inhomogeneous jet was already applied to explain the emission from CTA 102 jet in the optical, infrared and radio bands (139). The photons of different energy come from the jet regions which have different orientations (hence, different Doppler boosting factors) because of the curvature of the jet.

The SEDs obtained in the low state, P1 and P5 showing different features, and in the bright P2 have been modeled. In order to account for Compton dominance, we assume the bulk Lorentz factor (δ which equals to the bulk Lorentz factor for small viewing angles, $\delta \approx \Gamma$) of the emitting region increased from 10 in the low to 20 in the active states (these are typical values estimated for FSRQs (18)).

When the SEDs in the low state and in P2 are modeled, the emission from a compact region inside and outside the BLR is discussed. Instead, when modeling the periods with lacking correlation in the γ-ray and UV/optical/X-ray bands, we assume the emission from the radio to X-rays is produced in the extended and slow-moving region unrelated to the flaring component, while the HE γ-rays come from a compact and fast-moving region outside BLR (73).

5.4.1. Modeling the SEDs

The SEDs are fitted within a leptonic scenario that includes synchrotron/ SSC (23) (147) (24) and EIC (25) models. A spherical emission region ("blob") with a radius of R and B magnetic field carries relativistic electrons with a $N'_e(E'_e) = N'_0(E'_e/m_e c^2)^{-\alpha} Exp[-E'_e/E'_{cut}]$ distribution for $E'_e \geq E'_{min}$ where E'_{min} is the minimum electron energy. The size of the emitting region can be inferred from the observed e-folding timescale of 4.08 hours from the $R \leq \frac{\delta ct}{1+z} \approx \delta \times 2.16 \times 10^{14}\ cm$ relation. For the extended emission component, a region with a ten times larger radius ($\approx 4 \times 10^{16}\ cm$) will be used.

The low-energy component is modeled by synchrotron emission while for the IC scattering the photons from synchrotron emission, from BLR and dusty torus will be taken into account. The density of BLR (u_{BLR}) and dusty torus (u_{dust}) are calculated as functions of the distance r from the black hole by the formulae, (e.g., (41))

$$u_{BLR}(r) = \frac{L_{BLR}}{4\,\pi\,c\,{r_{BLR}}^2[1 + (r/r_{BLR})^3]}, \quad (5.2)$$

$$u_{dust}(r) = \frac{L_{dust}}{4\,\pi\,c\,{r_{dust}}^2[1 + (r/r_{dust})^4]}, \quad (5.3)$$

The estimated size and luminosity of BLR correspondingly are $r_{BLR} = 6.73 \times 10^{17}\ cm$ and $L_{BLR} = 4.14 \times 10^{45}\ erg\ s^{-1}$ (148). The disk luminosity is $L_{disk} = 10 \times L_{BLR} \approx 4.14 \times 10^{46}\ erg\ s^{-1}$ (assuming its 10% is reprocessed into BLR radiation) then the size and luminosity of torus will be $R_{dust} = 10^{18}(L_{disk}/10^{45})^{0.5} = 6.43 \times 10^{18}\ cm$ (43) and $L_{dust} = \eta L_{disk} = 1.24 \times 10^{46}\ erg\ s^{-1}$ ($\eta = 0.6$, (26)) a little larger than the value from tentative detection of dust emission in CTA 102 (149). Moreover, reproducing the near-IR data presented in fig. 5.5 with a blackbody component requires a luminosity of a few times $10^{46}\ erg\ s^{-1}$ in agreement with the value used. We adopt an effective temperature $T_{BLR} = 10^4\ K$ for the BLR radiation and $T = 10^3\ K$ for dusty torus.

The model free parameters and their uncertainties are estimated using the code described in section 3.3. The spectral model parameters have been derived through MCMC sampling of their likelihood distributions. For the model free parameters the following expected ranges are considered: $1.5 \leq \alpha \leq 10$, $0.511\ MeV \leq E'_{cut,min} \leq 10\ TeV$, and N_0 and B are defined as positive parameters.

5.5. Results and Discussion

The broadband emission from CTA 102 during its bright period in 2016-2018 was investigated. In the γ-ray band, during several periods the flux exceeded $10^{-5}\ photon\ cm^{-2}s^{-1}$ with the maximum being $(3.55 \pm 0.55) \times 10^{-5}\ photon\ cm^{-2}s^{-1}$ (above $100\ MeV$) observed on MJD 57738.47 which corresponds to an apparent isotropic γ-ray luminosity of $L_\gamma = 3.25 \times 10^{50}\ erg\ s^{-1}$ (for a distance of $d_L = 6.91\ Gpc$). This is one of the highest γ-ray luminosities observed from blazars so far (e.g., see (110)). In the proper frame of the jet,

the power emitted in the γ-ray band is $\sim L_\gamma/2\delta^2 = 4.06 \times 10^{47} erg\ s^{-1}$ for $\delta = 20$ which is higher than L_{disk} in agreement with the results by (107). During this bright period, on a 6-h timescale, the apparent luminosity was $\approx 2.0 \times 10^{50}\ erg\ s^{-1}$ with the rate of change $L/\Delta t \approx 1.89 \times 10^{46}\ erg\ s^{-2}$ (using $\Delta t = 6h/(1+z)\ \approx 1.06 \times 10^4\ s$), slightly higher than that observed from 3C 454.3 (150) and well above the Elliot-Shapiro relation (151).

The photon index varies as well: the hardest was 1.61 ± 0.10 observed on MJD 57752.45 which is unusual for FSRQs (having an average photon index of 2.4 (104)), while on MJD 57528.63 it was as soft as 3.08 ± 0.23. The hardest and softest photon indices were observed during the active and low states, confirming the harder-when-brighter trend. The HE photons ($> 10\ GeV$) were mostly emitted during the active period of MJD 57700-57800, the highest energy photon being $97.93\ GeV$. The fractional variability parameter F_{var} shows that the variability is stronger in the γ-ray band ($F_{var} > 0.9$), increasing at higher energies. The observed flares are asymmetric which might be due to different relations between particle acceleration and emission timescales. For example, the flares decrease much faster (F1-F3) when the accelerated particles start to escape from the emitting region or the cooling time gradually increases. Whereas, the flare will appear with a fast rise and a slow decay trend (F4) when the fast injected energetic particles loose energy or escape from the regions for a longer time. The observed shortest e-folding time is $\approx 4.1\ hours$, inferring that the emitting region is compact. However, during the brightest periods of $\sim$ MJD 57738.0 and $\sim$ MJD 57752.0, several minutes of observations were already enough to have $> 14.3\sigma$ detection significance, implying shorter time scale variability cannot be excluded (see (152) for detailed analysis in shorter periods).

Contemporaneous increase in the UV/optical and X-ray bands were also observed during some bright γ-ray periods. In the X-ray band ($0.3 - 10\ keV$), the maximum flux is $(6.71 \pm 0.21) \times 10^{-11}\ erg\ cm^{-2} s^{-1}$ and the photon index hardens in the bright periods. Comparing the Swift UVOT data obtained in different periods (see fig. 5.5 and SED/light curve movie) one can see a clear indication of flux increase in the UV/optical bands as well.

5.5.1. The origin of the emission

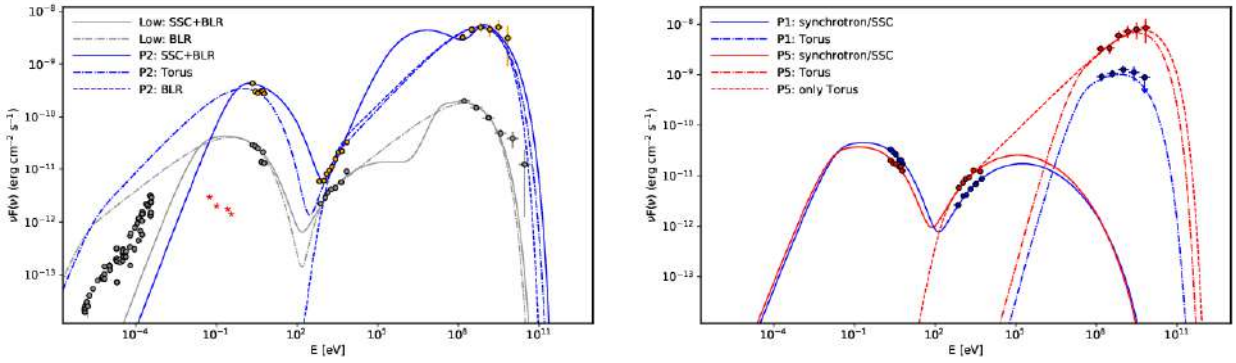

Figure 5.6. Modeling of the broadband SEDs of CTA 102 during the low state and P2 (left panel, gray and orange, respectively) and P1 and P5 (right panel, blue and red, respectively). The model parameters are given in Table 5.4. For the models applied see the text.

Table 5.4. Parameters best describing the multiwavelength emission in different periods

	low		*P1*	*P2*		*P5*	
	SSC+BLR	*BLR*	*compact*	*SSC+BLR*	*Torus*	*compact*	*Torus*
δ	10	10	20	20	20	20	20
α	2.51 ± 0.11	2.19 ± 0.02	2.12 ± 0.54	2.79 ± 0.44	1.91 ± 0.03	1.78 ± 0.52	1.95 ± 0.03
$E_{min}[MeV]$	68.25 ± 5.27	0.54 ± 0.03	155.59 ± 109.18	227.25 ± 26.43	1.38 ± 0.15	121.33 ± 67.33	0.63 ± 0.09
$E_c[GeV]$	0.67 ± 0.1	0.49 ± 0.04	1.42 ± 0.81	1.32 ± 0.43	0.98 ± 0.05	2.36 ± 1.54	3.85 ± 1.57
$E_{max}[TeV]$	0.57 ± 0.31	0.49 ± 0.31	0.48 ± 0.34	0.50 ± 0.30	0.41 ± 0.18	0.58 ± 0.25	0.54 ± 0.31
$B[G]$	5.40 ± 0.13	5.37 ± 0.14	0.23 ± 0.29	6.10 ± 0.50	1.01 ± 0.003	0.004 ± 0.042	0.015 ± 0.049
$L_B[ergs^{-1}]$	1.75×10^{46}	1.73×10^{46}	1.47×10^{42}	1.04×10^{45}	2.86×10^{43}	3.86×10^{38}	6.44×10^{39}
$L_e[ergs^{-1}]$	4.66×10^{44}	2.90×10^{45}	1.73×10^{46}	2.84×10^{45}	2.74×10^{47}	7.33×10^{46}	1.97×10^{47}

Initially, we modeled the SED observed in the low state (fig. 5.6; left panel). The radio data are treated as upper limits during the modeling, as the emission in this band is produced from the low-energy electrons which are perhaps from much extended regions. We note that the IR flux predicted by the models exceeds the archival IR data ~200 times in the flaring (P2) and 28.7 times in the selected low states (see fig. 5.6; left panel), implying that the non-thermal synchrotron emission from the jet dominates over the other emission

components. When the IC scatterings of both synchrotron and BLR photons are considered, the X-ray data allow to measure $E'_{min} = 68.25 \pm 5.27\ MeV$ and $\alpha = 2.51 \pm 0.11$. In order to explain the observed UV/optical data, a $E'_c = 0.67 \pm 0.1\ GeV$ cut-off is required which makes the SSC component to decay in sub-MeV band and the HE data are described only by IC of BLR photons. Alternatively, both X-ray and γ-ray data can be described by IC scattering of BLR photons (dot-dashed gray line in fig. 5.6) but the low-energy tail of IC spectra can reproduce the X-ray data only if $\gamma_{min} = E_e/m_e c^2$ is close to unity (106). In this case, however, the synchrotron emission of these low energy electrons with $E\_min = 0.54 \pm 0.03\ MeV$ will exceed the observed radio flux, making this scenario unlikely.

P2- Fig. 5.6 (left panel) shows the modeling of the SED observed in P2, considering the synchrotron and BLR photons (SSC+BLR, solid line) and then only BLR (dashed line) and only torus (dot-dashed line) photons. When the emitting region is within BLR (SSC+BLR), the hard X-ray spectra 1.23 ± 0.05 can be explained only when $E'_{min} = 227.25 \pm 26.43\ MeV$ and $\alpha = 2.79 \pm 0.44$, while $E'_c = 1.32 \pm 0.43\ GeV$ and $B = 6.10 \pm 0.50\ G$ are estimated from the low-energy component. Also, the external photon fields can dominate for the IC scattering as their density will increase Γ^2 times in the jet frame. For example, the required parameters (especially B) can be somewhat softened when only the IC of torus photons is considered (see Table 5.4). In the case of only BLR photons, the low-energy tail of IC spectra will decline at $\sim\gamma^2 \epsilon_{BLR} \approx 0.52\ keV$ (dashed line in fig. 5.6 left panel), contradicting Swift XRT data (unless lower δ is used). This modeling shows that during the bright γ-ray periods the emission can be also produced outside the BLR. At low energies, the model flux overpredicts noncontemporaneous radio data, but when taking the synchrotron self-absorption into account, which dominates below the frequencies $\sim 10^{13}\ Hz$ (calculated following (35)), the synchrotron flux will be below the radio data. We note that simultaneous observations at low energies, which are missing in this case, are crucial for better constraining of the model free parameters and for deriving some limits/constraints on the source emission properties. As the models presented in fig. 5.6 (left panel) predict different spectra and fluxes at GHz or mid-IR range, the observations at these bands can be also used to distinguish between these two models.

P1 and P5: Fig. 6 (right panel) shows the results of a two-zone SEDs modeling. For the emission from the extended blob we fixed all the parameters, except B and N_0, to the values obtained from the fitting of the SED in the low state, as in the UV/optical and X-ray bands the flux and photon indices did not change significantly (fig. 5.5). In addition, all the parameters of the compact blob are free, but it is required that its synchrotron emission has no contribution at lower energies. As compared with the low state, the magnetic field in the extended blobs is estimated to be low, $5.05 \pm 0.08\ G$ and $3.43 \pm 0.05\ G$ for P1 and P5, respectively, implying the modest X-ray flux changes are related with the increase of electron density. The γ-ray emission is produced in the interaction of fresh electrons (hard power law index ≤ 2.1) with the torus photons in the compact, fast-moving and particle-dominated blob $U_e/U_B \geq 10^{14}$ (fig. 5.6 right panel). The cut-off energies (defined by the last point in the *Fermi* LAT data) should be considered as lower limits, since there is no indication of break in the γ-ray spectra. In fig. 5.6 (right panel) the red dot-dashed line shows an alternative modeling, when both X-ray and γ-ray data are modeled by the IC scattering of torus photons. Within such a scenario, the flare is mainly due to the injection/cooling of $> 10\ GeV$ electrons, which are affecting only the HE spectra having small contribution to the X-ray band (e.g., the density at lower energies increases due to the cooling of HE electrons). Again, the low energy component should be necessarily produced in a different blob, otherwise its relatively constant peak frequency cannot be explained.

Jet energetics- The total power of the jet, $L_{jet} = L_B + L_e$ where $L_B = \pi c R_b^2 \Gamma^2 U_B$ and $L_e = \pi c R_b^2 \Gamma^2 U_e$ (e.g., (106)), is of the order of $L_{jet} \approx 2 \times 10^{46}\ erg\ s^{-1}$ in the low state and can be as large as $\approx 3 \times 10^{47} erg\ s^{-1}$ during the flares.

When the low and HE components are contemporaneously increased the required maximum energy of electrons (E_c) reaches only a few GeV constrained by the low energy data (the energy of synchrotron photons is proportional to $\sim \delta\, B\, E_e^2$). Therefore, during these intense γ-ray flares, the acceleration mechanisms are not effective enough or the electrons cool faster and do not reach HEs. On the other hand, when the γ-ray and

UV/optical/X-ray fluxes are uncorrelated, the γ-rays are perhaps produced in a different part of the jet that contains fresh electrons which can emit up to HE and VHE bands.

5.6. Conclusions

We report the results on the observations of CTA 102 in the UV/optical, X-ray and γ-ray bands from January 2016 to January 2018 when the source was in the bright and active states. Generally, the flares are roughly correlated in all these bands but the variability is more prominent in the γ-ray band with several bright flares when the γ-ray flux is substantially increased and the photon index is hardened, showing a harder-when-brighter trend. The measured hardest photon index $\Gamma = 1.61 \pm 0.10$ significantly differs from the average γ-ray photon index of CTA 102 and is unusual for FSRQs. The highest γ-ray flux measured by *Fermi* LAT is $(3.55 \pm 0.55) \times 10^{-5}\ photon\ cm^{-2}s^{-1}$ (above $100\,MeV$) observed on MJD 57738.47, corresponding to an extremely high isotropic γ-ray luminosity of $L_\gamma = 3.25 \times 10^{50}\ erg\ s^{-1}$.

We discussed the origin of the multiwavelength emission from CTA 102 in the framework of the one-zone and multi-zone synchrotron, SSC and EIC scenarios. We assumed a compact ($R \leq \delta \times 2.16 \times 10^{14}\ cm$ inferred from 4.08 hours γ-ray flux variation) blob inside and outside the BLR. In a single emitting region, the IC up-scattering of both synchrotron and BLR photons can explain the data observed in the low state, whereas the contribution of torus photons is essential in the flaring periods. When in the flaring periods the fluxes in the UV/optical, X-ray and γ-ray bands are unrelated, the two-zone models (with an extended blob inside and a compact fast-moving one outside the BLR) can well explain the observed data under reasonable assumptions on the required parameters. These periods appear to be more favorable for the HE emission from CTA 102 as the emitting electrons have higher cut-off energies and harder power-law indices. Most likely, the emission in these periods is produced in the regions outside BLR that contain fresh electrons which dominantly cool due to the IC scattering making the variability more evident in the γ-ray band.

Conclusion

In the thesis, the particle acceleration and emission processes in the jets of blazars are investigated. Blazars are sub-class of AGNs having extreme bright (high luminosity), rapidly variable and highly polarized emission and apparent superluminal motions detected within a few parsecs scale region of the jet which can be explained by assuming their jets is pointed almost exactly towards the Earth. Due to this the emitted radiation will be Doppler boosted and will appear brighter to the observer. Commonly, the blazars are divided into BL Lac objects and FSRQs, where BL Lacs show no sign of emission lines, whereas the FSRQs are more luminous, and have stronger emission lines. Both types of blazars are known to emit electromagnetic radiation in almost all frequencies that are currently being observed, ranging from radio to HE ($> 100\ MeV$) and VHE ($> 100\ GeV$) γ-ray bands. The modeling of the observed multiwavelength emission of blazar jets allows to estimate or constrain important physical parameters of the jet (composition, power, magnetic field, electron energy distribution, etc.) which are crucial for understanding their physics.

The thesis is structures as follows:

In the introduction, the importance and relevance of the thesis, the goals and objectives, as well as its content are briefly described.

In **Chapter 1** the key features of AGNs and their blazar sub-class observed in different wavelengths are presented. The relativistic transformation of relevant quantities (e.g., flux, luminosity, time, energy etc.) from the proper to observer frame are discussed.

In **Chapter 2** the synchrotron radiation and invers Compton scattering of jet accelerated electrons are described. The synchrotron emission spectra of one electron and electron population as well as their energy loss rates are presented and discussed. The IC scattering spectra and energy loss rates are discussed in both Thomson and Klein Nishina regimes. The IC scattering of various photon fields, such as synchrotron photons (SSC), photons reflected from BLR and IR photons emitted from torus are discussed in details.

In **Chapter 3** the methods for modeling the blazar multiwavelength SEDs are discussed. Various statistical methods for fitting the SEDs (such as Bayesian method) and optimization

of the model free parameters (e.g., χ^2, log-likelihood, etc) are presented. The affine-invariant method of MCMC sampling is described in details. These methods are used to develop a numerical code that allows to model blazar multiwavelength SEDs and find the parameter space with their uncertainties that statistically better describes the observed data. The application of the code is demonstrated by fitting the multiwavelength SEDs of PKS 0537-441 and Mkn 501 blazars. In sub-chapters 4.4-4.7, the prepared code is used to model the SEDs of PKS 1510-089, PKS 1222+216 and 3C 279 FSRQs observed in the VHE γ-ray bands. By modeling their multiwavelength SEDs in the quiescent and flaring states, the parameters of emitting electrons, the magnetic field in the emitting regions and jet luminosity are estimated which are crucial for the understanding the origin of flares. It is shown that the flares can be interpreted by the change of the location of the emitting region. Namely, during the flares the data are best described by assuming the emitting region is outside the BLR and the HE components are formed by IC scattering of dusty torus photons.

In **Chapter 4** the origin of multiwavelength emission from blazar PKS 1441+25 ($z = 0.939$) is discussed by analyzing γ-ray data accumulated by Fermi large Area Telescope during 2015 January - December. A γ-ray flare was observed in January 24, when the flux increased up to $(2.22 \pm 0.38) \times 10^{-6}\, photon\, cm^{-2} s^{-1}$ with the flux-doubling time-scale being as short as $\sim 1.44\, d$. The spectral analysis shows that from 2015 April 13 to April 28, the MeV-to-GeV photon index has hardened and changes in the range of $\Gamma = (1.73 - 17.9)$ for most of the time. The hardest photon index of $\Gamma = 1.54 \pm 0.16$ has been observed on MJD 57 131.46 with 11.8σ which is not common for FSRQs. For the same period the γ-ray spectrum shows a possible deviation from a simple power-law shape, indicating a spectral cutoff at $E_{cut} = 17.7 \pm 8.9\ GeV$. The SEDs during quiescent and flaring states are modelled using one-zone leptonic models that include the synchrotron, SSC and EIC processes; the model parameters are estimated using the MCMC method. The emission in the flaring states can be modelled assuming that either the bulk Lorentz factor or the magnetic field has increased. The modelling shows that there is a hint of hardening of the low-energy index (~ 1.98) of the underlying non-thermal distribution of electrons

responsible for the emission in 2015 April. Such hardening agrees with the γ-ray data, which pointed out a significant γ-ray photon index hardening on 2015 April 13 to 28.

In **Chapter 5** the origin of broadband emission of CTA 102 ($z = 1.037$) during the active states in 2016-2017 is discussed. In the γ-ray band, Fermi-LAT observed several prominent flares that followed a harder-when-brighter behavior. The peak γ-ray flux above 100 MeV, $(3.55 \pm 0.55) \times 10^{-5}\, photon\, cm^{-2} s^{-1}$ was observed on MJD 57,738.47 within $4.31\, minutes$, corresponds to an isotropic γ-ray luminosity of $L_\gamma = 3.25 \times 10^{50}\, erg\, s^{-1}$, comparable to the highest values observed from blazars so far. The analyses of the Swift UVOT/XRT data show an increase in the UV/optical and X-ray bands that is contemporaneous with the bright γ-ray periods. The X-ray spectrum observed by Swift XRT and NuSTAR during the γ-ray flaring period is characterized by a hard photon index of ~ 1.30. The shortest e-folding time was $4.08 \pm 1.44\ hr$, suggesting a very compact emission region $R \leq \delta \times 2.16 \times 10^{14}$ cm. The SEDs of CTA 102 in several periods (having different properties in UV/optical, X-ray, and γ-ray bands) is modeled assuming a compact blob inside and outside the BLR. It is found that the HE data are better described when the infrared thermal radiation of the dusty torus is considered. In the flaring periods when the correlation between the γ-ray and UV/optical/X-ray bands is lacking, the γ-ray emission can be produced from the interaction of fresh electrons in a different blob, which does not make a dominant contribution at lower energies.

As a continuation of the current thesis, a numerical code for modeling of blazar SEDs in the hadronic interaction scenarios will be developed. Blazars being among the most powerful nonthermal emitters were always considered as the main extragalactic sources of VHE neutrinos. Recently, this association was more strengthened when IceCube detected VHE neutrino events from the direction of TXS 0506+056 blazar. Considering the available multiwavelength data, as well as new VHE neutrino data from IceCube observations of blazars, the hadronic interaction code will allow deep investigation of the physics of blazar jets.

Bibliography

1. *Fermi Large Area Telescope Observations of Markarian 421: The Missing Piece of its Spectral Energy Distribution,*. **Abdo A. A., Ackermann M., Ajello M., et al.**, Vol. 736, No. 2, p. 131., The Astrophysical Journal, 2011.

2. *Observation of Gravitational Waves from a Binary Black Hole Merger*. **Abbott B. P., Abbott R., Abbott T. D., et al.**, Vol. 116, No. 6, Physical Review Letters, 2016.

3. *Multimessenger observations of a flaring blazar coincident with high-energy neutrino IceCube-170922A*. **IceCube Collaboration, Aartsen M. G., Ackermann M., et al.**, Vol. 361, Issue 6398, id. eaat1378, Science, 2018.

4. *Gamma-ray bursts*. **Mészáros, P.**, Vol. 69, Issue 8, pp. 2259-2321, Reports on Progress in Physics, 2006.

5. *Gamma-Ray Burst Energetics and the Gamma-Ray Burst Hubble Diagram: Promises and Limitations*. **Bloom J., Frail D. and Kulkarni S.**, Volume 594, Issue 2, pp. 674-683, The Astrophysical Journal, 2003.

6. *GRB090423 at a redshift of z~8.1*. **Salvaterra R., Della, Valle M. et al.**, Vol. 461, Issue 7268, p. 1258-1260, Nature, 2009.

7. **Beckmann, V., Shrader Ch.** *Active Galactic Nuclei*. Wiley-VCH, Verlag GmbH, 2012. ISBN-13: 978-3527410781, pages. 350.

8. *Active Galactic Nucleus Black Hole Masses and Bolometric Luminosities*. **Woo J., Urry C.**, Vol. 579, Issue 2, p. 530-544, The Astrophysical Journal, 2002.

9. *Extraction of Rotational Energy from a Black Hole*. **Penrose R., Floyd R.**, Vol. 229, Issue 6, pp. 177-179, Nature Physical Science, 1971.

10. *Relativistic magnetohydrodynamical effects of plasma accreting into a black hole*. **Ruffini R., Wilson J.**, Vol. 12, p. 2959-2962, Physical Review D - Particles and Fields, 3rd Series, 1975.

11. *Electromagnetic extraction of energy from Kerr black holes.* **Blandford R., Znajek R.**, Vol. 179, p. 433-456, Monthly Notices of the Royal Astronomical Society, 1977.

12. *FERMILARGE AREA TELESCOPE, VIEW OF THE CORE OF THE RADIO GALAXY CENTAURUS A.* **Abdo, A. A., Ackermann, M., Ajello, M., Atwood, W. B., Baldini, L., et al.**, Vol. 719, Issue 2, pp. 1433-1444, The Astrophysical Journal, 2010.

13. *FERMI LARGE AREA TELESCOPE DETECTION OF EXTENDED GAMMA-RAY EMISSION FROM THE RADIO GALAXY FORNAX A.* **Ackermann M., Ajello M., Baldini L., et al.**, Vol. 826. N. 1. p. 1, The Astrophysical Journal, 2016.

14. *Active galactic nuclei: what's in a name?* **Padovani P., Alexander D. M.**, Vol. 25, Issue 1, article id.2, 91 pp., The Astronomy and Astrophysics Review, 2017.

15. *Unified Schemes for Radio-Loud Active Galactic Nuclei.* **Urry C. M., & Padovani P.**, Vol. 107, p. 803, Publications of the Astronomical Society of the Pacific, 1995.

16. **Ghisellini G.,** *Radiative Processes in High Energy Astrophysics.* Berlin : Springer-Verlag, 2013., Vol. 873.

17. *MAGIC Discovery of, Very High Energy Emission from the FSRQ PKS 1222+21.* **Aleksic J., Antonelli L. A., et al.**, Vol. 730, Issue 1, article id. L8, p. 6, The Astrophysical Journal Letters, 2011.

18. *Fermi/LAT detection of extraordinary, Variability in the gamma-ray emission of the blazar PKS 1510-089.* **Foschini L., Bonnoli G., Ghisellini G., et al.**, Vol. 555, id. A138, p.5, Astronomy & Astrophysics, 2013.

19., V*ery Rapid High-amplitude Gamma-Ray, Variability in Luminous Blazar PKS 1510-089 Studied with Fermi-LAT.* **Saito S., Stawarz L., & et al.**, Vol. 766, Issue 1, article id. L11, p. 6, The Astrophysical Journal Letters, 2013.

20. *Polarization and beaming effect for BL Lacertae objects.* **Fan J. H., Cheng K. S., Zhang L., & Liu C. H.**, Vol. 327, p. 947-951, Astronomy and Astrophysics, 1997.

21. *Simultaneous UBVRI photopolarimetry of three blazars: 3C 66A, S5 0716+714 and OJ 287*. **Takalo L. O., Sillanpaeae A., & Nilsson K.**, Vol. 107, p. 497-501, Astronomy and Astrophysics Suppl., 1994.

22. *The Spectral Energy Distribution of Fermi Bright Blazars*. **Abdo A. A., Ackermann M., Ajello M., et.al.**, Vol. 716, Issue 1, p. 30-70, ApJ, 2010.

23. *Inhomogeneous synchrotron-self-Compton models and the problem of relativistic beaming of BL Lac objects*. **Ghisellini G., Maraschi L., Treves A.**, Vol. 146, No. 2, p. 204-212, Astronomy and Astrophysics, 1985.

24. *A jet model for the gamma-ray emitting blazar 3C 279*. **Maraschi L., Ghisellini G., Celotti A.**, Vol. 397, No. 1, p. L5-L9, Astrophysical Journal, 1992.

25. *Comptonization of diffuse ambient radiation by a relativistic jet: The source of gamma rays from blazars?*. **Sikora M., Begelman M. C., Rees M. J.**, Vol. 421, No. 1, p. 153-162, Astrophysical Journal, 1994.

26. *Canonical high-power blazars*. **Ghisellini G., Tavecchio F.**, Vol. 397, Issue 2, p. 985-1002, Monthly Notices of the Royal Astronomical Society, 2009.

27. *Photohadronic origin of γ -ray BL Lac emission: implications for IceCube neutrinos*. **Petropoulou M., S. Dimitrakoudis, P. Padovani, A. Mastichiadis, E. Resconi.**, Vol. 448, Issue 3, p. 2412-2429, Monthly Notices of the Royal Astronomical Society, 2015.

28. *Gamma-ray flaring of 3C 279 - A proton-initiated cascade in the jet?* **Mannheim K., & Biermann P. L.**, Vol. 253, No. 2, p. L21-L24., Astronomy and Astrophysics, 1992.

29. *TeV gamma rays from BL Lac objects due to synchrotron radiation of extremely high energy protons*. **Aharonian F.**, Volume 5, Issue 7, p. 377-395, NewA, 2000.

30. *A proton synchrotron blazar model for flaring in Markarian 501*. **Mucke, A., & Protheroe, R. J.**, Vol. 15, Issue 1, p. 121-136, Astroparticle Physics, 2001.

31. *Leptonic and Hadronic Modeling of Fermi-detected Blazars*. **Böttcher M., Reimer A., Sweeney K., Prakash A.**, Vol. 768, Issue 1, article id. 54, p. 14, The Astrophysical Journal, 2013.

32. *Properties of Blazar Jets Defined by an Economy of Power*. **Petropoulou M., & Dermer C. D.**, Vol. 825, Issue 1, article id. L11, p. 5, The Astrophysical Journal Letters, 2016.

33., V*ariability of Active Galactic Nuclei*. **Ulrich M.H., L. Maraschi, C.M. Urry.**, Vol. 35, p. 445-502, Annual Review of Astronomy and Astrophysics, 1997.

34. *Particle acceleration and synchrotron emission in blazar jets*. **Kirk J. G., Rieger F. M., & Mastichiadis A.**, Vol. 333, p. 452-458, Astronomy and Astrophysics, 1998.

35. **Rybicki, G. B., & Lightman, A. P.,** *Radiative processes in astrophysics* . (New York, Wiley-Interscience): 11, 12, 26, 27, 1979.

36. **Aharonian F., Bergstrom L., Dermer C.,** *Astrophysics at, Very High Energies*. Heidelberg: Swiss Society for Astrophysics and Astronomy, Saas-Fee Advanced Course,, Volume 40. ISBN 978-3-642-36133-3. Springer, 2013.

37. *Bremsstrahlung, Synchrotron Radiation, and Compton Scattering of High-Energy Electrons Traversing Dilute Gases*. **Blumenthal G. R., & Gould R. J.**, Vol. 42, Issue 2, pp. 237-271, Reviews of Modern Physics, 1970.

38. **Dermer C., Menon G.,** *High Energy Radiation from Black Holes: Gamma Rays, Cosmic Rays, and Neutrinos*. Princeton University Press, 2009.

39. *Klein-Nishina effects in the spectra of non-thermal sources immersed in external radiation fields*. **Moderski R., Sikora M., Coppi P., Aharonian F.**, Vol. 363, Issue 3, p. 954-966, Monthly Notices of the Royal Astronomical Society, 2005.

40. *The Beaming Pattern and Spectrum of Radiation from Inverse Compton Scattering in Blazars*. **Georganopoulos M., Kirk J. G., Mastichiadis A.**, Vol. 561, Issue 1, pp. 111-117, The Astrophysical Journal, 2001.

41. *Constraining Emission Models of Luminous Blazar Sources.* **Sikora, M., Stawarz, L., Moderski, R., Nalewajko, K., & Madejski, G. M.**, Vol. 704, Issue 1, p. 38-50, The Astrophysical Journal, 2009.

42. *The Structure and Emission Model of the Relativistic Jet in the Quasar 3C 279 Inferred from Radio to High-energy γ-Ray Observations in 2008-2010.* **Hayashida M., Madejski G. M., Nalewajko K.**, Vol. 754, Issue 2, article id. 114, p. 22 , The Astrophysical Journal, 2012.

43. *AGN Dusty Tori. II. Observational Implications of Clumpiness* . **Nenkova M., Sirocky M. M., Nikutta R., Ivezić Ž., Elitzur M.**, Vol. 685, Issue 1, p. 160-180, The Astrophysical Journal, 2008.

44. *Some comments on radiation mechanisms in Lacertids.* **Blandford R. D., & Rees M. J.,** p. 328;, in Pittsburgh Conference on BL Lac Objects ed. A. M. Wolfe (Pittsburgh, PA: Univ. Pittsburgh Press), 1978.

45. *On the Origin of the Cosmic Radiation.* **Fermi E.**, Vol. 75, Issue 8, pp. 1169-1174, Physical Review, 1949.

46. *Electron Acceleration and Gamma-Ray Emission from Blazars.* **Inoue S., Takahara F.**, Vol. 463, p. 555, Astrophysical Journal, 1996.

47. *Nonstationarity of Spectra of Young Sources of Nonthermal Radio Emission.* **Kardashev, N. S.**, Vol. 6, p. 317, Soviet Astronomy, 1962.

48. *Fokker-Planck Equations of Stochastic Acceleration: Green's Functions and Boundary Conditions.* **Park B., Petrosian V.**, Vol. 446, p. 699, Astrophysical Journal, 1995.

49. **https://events.mpifr-bonn.mpg.de/indico/event/30/material/slides/12.pdf.**

50. *Equation of State Calculations by Fast Computing Machines.* **Metropolis N., Rosenbluth A. W., Rosenbluth M. N., Teller A. H., & Teller E.**, Vol. 21, Issue 6, p. 1087-1092 , The Journal of Chemical Physics, 1953.

51. *WEAK CONVERGENCE AND OPTIMAL SCALING OF RANDOM WALK METROPOLIS ALGORITHMS*. **Roberts G. O., Gelman A. , Gilks W. R.**, Vol. 7, No. 1, p. 110-120, The Annals of Applied Probability, 1997.

52. *Ensemble samplers with affine invariance*. **Goodman J. & Weare J.**, Vol. 5, No. 1, p. 65-80, Communications in Applied Mathematics and Computational Science, 2010.

53. *A general purpose scale-independent MCMC algorithm*. **Christen J.,** CIMAT, Guanajuato, 2007, Vols. technical report I-07-16.

54. *emcee: The MCMC Hammer*. **Foreman-Mackey D., Hogg D. W., Lang D., & Goodman J.**, Vol. 125, Issue 925, pp. 306, Publications of the Astronomical Society of the Pacific, 2013.

55. *Measuring the Hubble constant with Type Ia supernovae as near-infrared standard candles*. **Dhawan S., Jha S. W., & Leibundgut B.**, Vol. 609, id.A72, 13 pp., Astronomy & Astrophysics, 2018.

56. *Measurement of the Radius of Neutron Stars with High Signal-to-noise Quiescent Low-mass X-Ray Binaries in Globular Clusters*. **Guillot S., Servillat M., Webb N. A., & Rutledge R. E.**, Vol. 772, Issue 1, article id. 7, p. 29, The Astrophysical Journal, 2013.

57. *How to constrain your M dwarf: measuring effective temperature, bolometric luminosity, mass, and radius*. **Mann A. W., Feiden G. A., Gaidos E., Boyajian T., & Braun K.**, Vol. 804, Issue 1, article id. 64, p. 38 , The Astrophysical Journal, 2015.

58. ***http://adsabs.harvard.edu/cgi-bin/nph-ref_query?bibcode=2013PASP..125..306F&refs=CITATIONS.***

59. *Naima: a Python package for inference of particle distribution properties from nonthermal spectra.* **Zabalza, V.**, http://pos.sissa.it/cgi-bin/reader/conf.cgi?confid=236, id.922, Proceedings of the 34th International Cosmic Ray Conference (ICRC2015), 2015.

60. *Estimation of cosmological parameters using adaptive importance sampling*. **Wraith D., M. Kilbinger, K. Benabed, O. Capp´e, J.-F. Cardoso, G. Fort, S. Prunet, and C. P. Robert.**, Vol. 80, Issue 2, id. 023507, Physical Review D, 2009.

61. *A Simplex Method for Function Minimization*. **Nelder J. A., & Mead R.**, Vol. 7, p. 308-313, Computer Journal, 1965.

62. *Extragalactic optical-infrared background radiation, its time evolution and the cosmic photon-photon opacity*. **Franceschini A., Rodighiero G.,, Vaccari M.**, Vol. 487, Issue 3, p. 837-852, Astronomy and Astrophysics, 2008.

63. *Extragalactic background light inferred from AEGIS galaxy-SED-type fractions*. **Dominguez A., et al.,** Vol. 410, Issue 4, pp. 2556-2578, Monthly Notices of the Royal Astronomical Society, 2011.

64. *Insights into the High-energy γ-ray Emission of Markarian 501 from Extensive Multifrequency Observations in the Fermi Era*. **Abdo A. A., Ackermann M., Ajello M., et al.**, Vol. 727, article id. 129, 26 pp., ApJ, 2011a.

65. *Long-term monitoring of PKS 0537-441 with Fermi-LAT and multiwavelength observations*. **D'Ammando F., Antolini E., Tosti G., et al.**, Vol. 431, Issue 3, p.2481-2492, Monthly Notices of the Royal Astronomical Society, 2013.

66. ***http://tevcat.uchicago.edu/.***

67. *H.E.S.S. discovery of, VHE & gamma-rays from the quasar PKS 1510-089*. **Abramowski A., Acero F., et al.,** Vol. 554, id. A107, p. 7, Astronomy & Astrophysics, 2013.

68. *MAGIC gamma-ray and multi-frequency observations of flat spectrum radio quasar PKS 1510-089 in early 2012*. **Aleksic J., Ansoldi S., et al.**, Volume 569, id. A46, pp. 21, Astronomy & Astrophysics, 2014.

69. *PKS 1510-089: a rare example of a flat spectrum radio quasar with a, Very high-energy emission*. **Barnachka A., Moderski R., et al.**, Vol. 567, id. A113, p. 8, A&A, 2014.

70. *Multiwavelength observations of a, VHE gamma-ray flare from PKS 1510-089 in 2015.* **Aleksic J., Ansoldi S., et al.**, Vol. 603A, p. 29A, Astronomy and Astrophysics, 2017.

71. ***http://www.asdc.asi.it/.***

72. *Fermi Large Area Telescope Detection of Bright Gamma-Ray Outbursts from the Peculiar Quasar 4C +21.35.* **Tanaka Y., et al.**, Vol. 733, Issue 1, article id. 19, p. 10, The Astrophysical Journal, 2011.

73. *On the origin of the γ-ray emission from the flaring blazar PKS 1222+216.* **Tavecchio F., Becerra-Gonzalez J., Ghisellini G., et al.,** Vol. 534, id. A86, p. 8, Astronomy & Astrophysics, 2011.

74. *Location of gamma-ray flaring region in quasar 4C +21.35.* **Lei M., and Wang J.**, Vol. 67, Issue 4, id. 799, Publications of the Astronomical Society of Japan, 2015.

75. *Multi-Wavelength Observations of 3C 279 During the Extremely Bright Gamma-Ray Flare in 2014 March-April.* **Paliya, V., Sahayanathan S., Stalin S.**, Vol. 803, Issue 1, article id. 15, p. 13, The Astrophysical Journal, 2015.

76. *Flaring Patterns in Blazars.* **Paggi A., Cavaliere A., Vittorini, V., D'Ammando F., & Tavani M.**, Vol. 736, Issue 2, article id. 128, p. 5 , The Astrophysical Journal, 2011.

77. *Angular, spectral, and time distributions of highest energy protons and associated secondary gamma rays and neutrinos propagating through extragalactic magnetic and radiation fields.* **Aharonian F. A., Kelner S. R., Prosekin A. Y.**, Vol. 82, Issue 4, id. 043002 , Physical Review D, 2010.

78. *Compton scattering of relativistic electrons in compact X-ray sources.* **Aharonian F. A., Atoyan A. M.,** Vol. 79, No. 2, p. 321-336, Astrophysics and Space Science, 1981.

79. *An Exceptional, Very High Energy Gamma-Ray Flare of PKS 2155-304.* **Aharonian F. et al.**, Vol. 664, Issue 2, p. L71-L74, The Astrophysical Journal, 2007.

80. *Black hole lightning due to particle acceleration at subhorizon scales.* **Aleksic J., Ansoldi S. et al.**, Vol. 346, p. 1080-1084, Science, 2014a.

81. *Comptonization of Infrared Radiation from Hot Dust by Relativistic Jets in Quasars.* **Blazejowski M., Sikora M., Moderski R., & Madejski G. M.**, Vol. 545, N. 1, 107, The Astrophysical Journal, 2000.

82. *BL Lac objects in the synchrotron proton blazar model.* **Mucke, A., Protheroe, R. J., Engel, R., Rachen, J. P.,Stanev, T.**, Vol. 18, Issue 6, p. 593-613, Astroparticle Physics, 2003.

83. *Absorption of 10-200 GeV Gamma Rays by Radiation from Broad-Line Regions in Blazars.* **Liu H. T., & Bai J. M.**, Vol. 653, Issue 2, p. 1089-1097, The Astrophysical Journal, 2006.

84. *GeV Breaks in Blazars as a Result of Gamma-ray Absorption Within the Broad-line Region.* **Poutanen J., & Stern B.**, Vol. 717, Issue 2, p. L118-L121, The Astrophysical Journal Letters, 2010.

85. *Gamma-Rays from the Quasar PKS 1441+25: Story of an Escape.* **Abeysekara A. U. et al.**, Vol. 815, Issue 2, article id. L22, p. 7, ApJ, 2015.

86., *Very High Energy Gamma-Rays from the Universe's Middle Age: Detection of the z = 0.940 Blazar PKS 1441+25 with MAGIC.* **Ahnen M. L., Ansoldi S., et al.**, 2015., Vol. 815, Issue 2, article id. L23, p. 8, The Astrophysical Journal Letters, 2015.

87. *Detection of, Very high energy gamma-ray emission from the gravitationally lensed blazar QSO B0218+357 with the MAGIC telescopes.* **Ahnen M., et al.**, Vol. 595, id. A98, p. 11, Astronomy & Astrophysics, 2016.

88. *Simultaneous X-Ray and Gamma-Ray Observations of TEV Blazars: Testing Synchro-Compton Emission Models and Probing the Infrared Extragalactic Background.* **Coppi P. S., Aharonian F. A.**, Vol. 521, No. 1, p. L33, ApJ, 1999.

89. *Constraints on the Extragalactic Background Light from Gamma-Ray Observations of High-Redshift Quasars*. **Madau P., Phinney E. S.**, Vol. 456, p. 124, Astrophysical Journal, 1996.

90. *Spectroscopy of Broad-line Blazars from 1LAC*. **Shaw M. S. et al.**, Vol. 748, Issue 1, article id. 49, p. 12, The Astrophysical Journal, 2012.

91. *Discovery of, Very High Energy Gamma-Ray Emission from the distant FSRQ PKS 1441+25 with the MAGIC telescopes*. **Mirzoyan** R. 7416, The Astronomer's Telegram, 2015.

92., V*ery-high-energy gamma-ray emission from PKS 1441+25 detected with, VERITAS*. **Mukherjee R.** 7433, The Astronomer's Telegram, 2015.

93. *The Large Area Telescope on the Fermi Gamma-Ray Space Telescope Mission*. **Atwood W. B. et al.**, Volume 697, Issue 2, pp. 1071-1102, The Astrophysical Journal, 2009.

94. ***http://fermi.gsfc.nasa.gov/ssc/data/analysis/software/.***

95. *Fermi Large Area Telescope Third Source Catalog*. **Acero F., Ackermann M., Ajello M., et al.**, Vol. 218, Issue 2, article id. 23, p. 41, The Astrophysical Journal Supplement Series, 2015.

96. *An adaptive-binning method for generating constant-uncertainty/constant-significance light curves with Fermi-LAT data*. **Lott B., Escande L., Larsson S., & Ballet J.**, Vol. 544, id.A6, p. 12, Astronomy & Astrophysics, 2012.

97. *High energy gamma-rays from PKS 1441+25*. **Sahakyan N., Gasparyan S.**, Vol. 1792, Issue 1, id.050005, AIP Conference Proceedings, 2017.

98. *Gamma-ray Light Curves and, Variability of Bright Fermi-detected Blazars*. **Abdo A. A., Ackermann M., Ajello M. & et al.**, Vol. 722, Issue 1, pp. 520-542, ApJ, 2010a.

99. ***http://tools.asdc.asi.it/SED/index.jsp.***

100. *Radio-gamma-ray connection and spectral evolution in 4C +49.22 (S4 1150+49): the Fermi, Swift and Planck, View*. **Cutini S. et al.**, Vol. 445, Issue 4, p. 4316-4334, Monthly Notices of the Royal Astronomical Society, 2014.

101. *Fermi Large Area Telescope and Multi-wavelength Observations of the Flaring Activity of PKS 1510-089 between 2008 September and 2009 June*. **Abdo A. A., Ackermann M., Agudo I. & et al.**, Vol. 721, Issue 2, p. 1425-1447, ApJ, 2010b.

102. *Fermi/LAT broad emission line blazars*. **Ghisellini G., & Tavecchio F.**, Vol. 448, Issue 2, p. 1060-1077, Monthly Notices of the Royal Astronomical Society, 2015.

103. *Intrinsic Gamma-ray luminosity, black hole mass, jet and accretion in Fermi blazars*. **Xiong D. R., Zhang X.**, Vol. 441, Issue 4, p. 3375-3395, Monthly Notices of the Royal Astronomical Society, 2014.

104. *The Third Catalog of Active Galactic Nuclei Detected by the Fermi Large Area Telescope*. **Ackermann M., Ajello M., et.al.**, Vol. 810, Issue 1, article id. 14, p. 34, The Astrophysical Journal, 2015.

105. *Exploring the Blazar Zone in High-energy Flares of FSRQs*. **Pacciani L., Tavecchio F., Donnarumma I., Stamerra A., Carrasco L., Recillas E., Porras A., Uemura M.**, Vol. 790, Issue 1, article id. 45, p. 17, The Astrophysical Journal, 2014.

106. *The power of blazar jets*. **Celotti A., Ghisellini G.,** Vol. 385, Issue 1, p. 283-300, Monthly Notices of the Royal Astronomical Society, 2008.

107. *The power of relativistic jets is larger than the luminosity of their accretion disks*. **Ghisellini G., Tavecchio F., Maraschi L., Celotti A., Sbarrato T.**, Vol. 515, Issue 7527, p. 376-378, Nauture, 2014.

108. *Minute-timescale >100 MeV Gamma-Ray, Variability during the Giant Outburst of Quasar 3C 279 Observed by Fermi-LAT in 2015 June*. **Ackermann, M., Anantua, R., et al.**, Vol. 824, Issue 2, article id. L20, p. 8, The Astrophysical Journal Letters, 2016.

109. *Search for the shortest, Variability at gamma rays in flat-spectrum radio quasars.* **Foschini L., Ghisellini G., Tavecchio F., Bonnoli G., Stamerra A.**, Vol. 530, id. A77, p. 5, Astronomy & Astrophysics, 2011.

110. *The brightest gamma-ray flares of blazars.* **Nalewajko, K.**, Vol. 430, Issue 2, p. 1324-1333, Monthly Notices of the Royal Astronomical Society, 2013.

111. *Locating the Gamma-ray emission region of the flat spectrum radio quasar PKS 1510-089.* **Brown A.**, Vol. 431, Issue 1, p. 824-835, Monthly Notices of the Royal Astronomical Society, 2013.

112. *Constraining the location of rapid gamma-ray flares in the flat spectrum radio quasar 3C 273.* **Rani B., Lott B., Krichbaum T. P., Fuhrmann L., & Zensus J. A.**, Vol. 557, id. A71, p. 11, Astronomy & Astrophysics, 2013.

113. *Rapid, Variability of Blazar 3C 279 during Flaring States in 2013-2014 with Joint Fermi-LAT, NuSTAR, Swift, and Ground-Based Multiwavelength Observations.* **Hayashida M., Nalewajko K., & et al.**, Vol. 807, Issue 1, article id. 79, p. 18, The Astrophysical Journal, 2015.

114. *Large Redshifts of Five Quasi-Stellar Sources.* **Schmidt M.**, Vol. 141, p. 1295 , Astrophysical Journal, 1965.

115. *The class of highly polarized quasars - Observations and description.* **Moore, R. L., & Stockman, H. S.**, Vol. 243, p. 60-75, Astrophysical Journal, 1981.

116. *Long-term optical behavior of 144 compact extragalactic objects - 1969-1988.* **Pica A. J., Smith A. G., Webb J. R., et al.**, Vol. 96, p. 1215-1226, Astronomical Journal, 1988.

117. *A Multi-wavelength Polarimetric Study of the Blazar CTA 102 during a Gamma-Ray Flare in 2012.* **Casadio C., Gomez J. L., & et al.**, Vol. 813, Issue 1, article id. 51, p. 14 , The Astrophysical Journal, 2015.

118. *Blazar CTA 102 Reaches Historic Optical Maximum During Current Extended Period of Activity.* **Balonek T. J., Zhang S., & et al**. No. 9732, The Astronomer's Telegram, 2016.

119. *A Spectacular, Unprecedented Optical Flare in the Blazar CTA 102.* **Chapman K. J., Sabyr A., Stahlin R. W., Zhang S., Balonek T. J.**, No. 9756, The Astronomer's Telegram, 2016.

120. *Intra-night optical activity of the blazar CTA 102 during its maximum state.* **Popov, V., & Bachev R.**, 9776, The Astronomer's Telegram, 2016.

121. *Fermi LAT observation of renewed and strong GeV gamma-ray activity from blazar CTA 102.* **Ciprini S.,** 9869, The Astronomer's Telegram, 2016.

122. *AGILE detects renewed gamma-ray emission from the FSRQ CTA 102.* **Bulgarelli A., Verrecchia F., & et al.**, No. 9788, The Astronomer's Telegram, 2016.

123. *Yet another strong GeV gamma-ray outburst of blazar CTA 102 observed by the Fermi LAT.* **Ciprini S.**, 10292; The Astronomer's Telegram, 2017.

124. *Fermi-LAT detection of strong flaring activity from the FSRQ CTA 102.* **Becerra J., Carpenter B., & Cutini S.**, No. 8722, The Astronomer's Telegram, 2016.

125. *AGILE detection of enhanced gamma-ray emission from the FSRQ CTA 102.* **Minervini, G., Piano, G., & et al.**, 9743, The Astronomer's Telegram, 2016.

126. *A NIR Flare of the QSO PKS0306+102.* **Carrasco L., Miramon J., Recillas E., et al.**, No. 8574; The Astronomer's Telegram, 2016.

127. *Log-parabolic spectra and particle acceleration in the BL Lac object Mkn 421: Spectral analysis of the complete BeppoSAX wide band X-ray data set.* **Massaro, E., Perri, M., Giommi, P., & Nesci, R.**, Vol. 413, p. 489-503, Astronomy and Astrophysics, 2004.

128. *PKS 1502+106: A New and Distant Gamma-ray Blazar in Outburst Discovered by the Fermi Large Area Telescope.* **Abdo A. A., Ackermann M., Ajello M. & et al.**, Vol. 710,N. 1, p. 810-827, ApJ, 2010d.

129. *Fermi Gamma-ray Space Telescope Observations of Gamma-ray Outbursts from 3C 454.3 in 2009 December and 2010 April.* **Ackermann M., Ajello M., Baldini L., et al.**, Vol. 721, Issue 2, p. 1383-1396, The Astrophysical Journal, 2010.

130. *Rapid Gamma-Ray, Variability of NGC 1275.* **Baghmanyan, V., Gasparyan S., & Sahakyan N.**, Vol. 848, Issue 2, article id. 111, p. 8 , The Astrophysical Journal, 2017.

131. *Parameter estimation in astronomy through application of the likelihood ratio.* **Cash W.**, Astrophysical Journal,, Vol. 228, p. 939-947, Astrophysical Journal, 1979.

132. *Multiwavelength Observations of the Powerful Gamma-Ray Quasar PKS 1510-089: Clues on the Jet Composition.* **Kataoka J., Madejski G., Sikora M., et al.,** Vol. 672, Issue 2, p. 787-799, The Astrophysical Journal, 2008.

133. *AGILE detection of extreme Gamma-ray activity from the blazar PKS 1510-089 during March 2009. Multifrequency analysis.* **D'Ammando F., Raiteri C. M.,, Villata M., et al.**, Vol. 529, id. A145, p. 12, Astronomy & Astrophysics, 2011.

134. *Multiwavelength Observations of 3C 454.3. III. Eighteen Months of Agile Monitoring of the "Crazy Diamond".,* ***V*****ercellone S., D'Ammando F., Vittorini, V., et al.**, Vol. 712, Issue 1, p. 405-420, The Astrophysical Journal, 2010.

135. *The Brightest Gamma-Ray Flaring Blazar in the Sky: AGILE and Multi-wavelength Observations of 3C 454.3 During 2010 November.,* ***V*****ercellone S., Striani E., Vittorini, V., et al.**, Vol. 736, Issue 2, article id. L38, p. 8, The Astrophysical Journal Letters, 2011.

136. *Measuring Reddening with Sloan Digital Sky Survey Stellar Spectra and Recalibrating SFD.* **Schlafly E. F., & Finkbeiner D. P.**, Vol. 737, Issue 2, article id. 103, p. 13, The Astrophysical Journal, 2011.

137. *Correcting for the Effects of Interstellar Extinction.* **Fitzpatrick E. L.,** Vol. 111, Issue 755, p. 63-75, The Publications of the Astronomical Society of the Pacific, 1999.

138. *An Updated Ultraviolet Calibration for the Swift/UVOT*. **Breeveld A. A., Landsman W., Holland S. T., et al.**, Vol. 1358, 373-376, in American Institute of Physics Conference Series, 2011.

139. *Blazar spectral, Variability as explained by a twisted inhomogeneous jet*. **Raiteri C. M., Villata M., Acosta-Pulido J. A., et al.**, Vol. 552, Issue 7685, p. 374-377, Nature, 2017.

140. *The Nuclear Spectroscopic Telescope Array (NuSTAR) High-energy X-Ray Mission*. **Harrison F. A., Craig W. W., Christensen F. E., & et al.,** Vol. 770, Issue 2, article id. 103, p. 19, The Astrophysical Journal, 2013.

141. *On characterizing the, Variability properties of X-ray light curves from active galaxies.*, ***V*aughan S., Edelson R., Warwick R. S., & Uttley P.**, Vol. 345, Issue 4, p. 1271-1284, Monthly Notices of the Royal Astronomical Society, 2003.

142. *Fermi-Large Area Telescope Observations of the Exceptional Gamma-ray Outbursts of 3C 273 in 2009 September*. **Abdo A. A., Ackermann M., Ajello M. & et al.**, Volume 714, Issue 1, pp. L73-L78, ApJL, 2010c.

143. ***https://lmfit.github.io/lmfit-py/.***

144. ***https://youtu.be/K9WWWSy6W8U***.

145. *Spectral Properties of Bright Fermi-Detected Blazars in the Gamma-Ray Band*. **Abdo A. A., Ackermann M., Ajello M. & et al**., Vol. 710, Issue 2, p. 1271-1285, ApJ, 2010e.

146. *The Infrared-Gamma-Ray Connection: A WISE, View of the Extragalactic Gamma-Ray Sky*. **Massaro, F., & D'Abrusco, R.,** Vol. 827, Issue 1, article id. 67, p. 6, The Astrophysical Journal, 2016.

147. *An Analysis of the Synchrotron Self-Compton Model for the Multi--Wave Band Spectra of Blazars*. **Bloom S. D., & Marscher A. P.,** Vol. 461, p. 657, Astrophysical Journal, 1996.

148. *Hubble Space Telescope ultraviolet spectroscopy of blazars: emission-line properties and black hole masses*. **Pian E., Falomo R., & Treves A.,** Vol. 361, Issue 3, p. 919-926, Monthly Notices of the Royal Astronomical Society, 2005.

149. *Emission from Hot Dust in the Infrared Spectra of Gamma-ray Bright Blazars*. **Malmrose, M. P., Marscher, A. P., Jorstad, S. G., Nikutta,R., Elitzur, M.,** Vol. 732, Issue 2, article id. 116, p. 8, The Astrophysical Journal, 2011.

150. *Fermi Gamma-ray Space Telescope Observations of the Gamma-ray Outburst from 3C454.3 in November 2010*. **Abdo A. A., Ackermann M., Ajello M. & et al.**, Vol. 733, Issue 2, p. L26, ApJL, 2011.

151. *On the, Variability of the Compact Nonthermal Sources*. **Elliot J. L., & Shapiro S. L.**, Vol. 192, p.L3, Astrophysical Journal, 1974.

152. *Short-timescale γ-Ray, Variability in CTA 102*. **Shukla A., Mannheim K., Patel S. R., et al.,** Vol. 854, Issue 2, article id. L26, p. 6, The Astrophysical Journal Letters, 2018.